UNIVERSITY OF CALIFORNIA
RIVERSIDE

Optimizing Thermoelectric Properties of Metal Chalcogenides by Engineering Composition and Crystallinity

A Dissertation submitted in partial satisfaction
of the requirements for the degree of

Doctor of Philosophy

in

Chemical and Environmental Engineering

by

Ji Won Kim

March 2015

Dissertation Committee:
Dr. Nosang V. Myung, Chairperson
Dr. Robert C. Haddon
Dr. Phillip Neil Christopher

The Dissertation of Ji Won Kim is approved:

_____

_____

_____

Committee Chairperson

University of California, Riverside

Acknowledgements

I would like to express my gratitude to all those who gave me the possibility to complete this thesis.

ABSTRACT OF THE DISSERTATION

Optimizing Thermoelectric of Metal Chalcogenides by Engineering Composition and Crystallinity

by

Ji Won Kim

Doctor of Philosophy, Graduate Program in Chemical and Environmental Engineering
University of California, Riverside, March 2015
Dr. Nosang V. Myung, Chairperson

Metal Chalcogenide nanostructures have been extensively implemented for high-performance thermoelectric applications, which can directly convert waste-heat-energy into electricity, with the support of theoretical and empirical results. In fact, finding a novel and cost effective synthesis approach that facilitates the formation of stable and reproducible nanostructured thermoelectric materials determines the commercial applicability.

The overall objective of this work is to synthesize metal chalcogenide nanostructures with outstanding thermoelectric performance by an electrodeposition technique, which is one of the most versatile methods for low dimensional nanostructures in a cost effective and scalable manner. Precise control over dimension, chemical composition, crystallinity, crystal structure, grain size, preferred orientation, and the attainment of nanoinclusions and/or intermediate phases based on thermodynamically favored solid-state phase transition yields optimal electrical transport and thermoelectric properties of the metal chalcogenide nanostructures. In this dissertation, antimony

telluride (Sb_xTe_y), silver doped antimony telluride, antimony telluride ($Ag_xSb_{(2-x)}Te_{(3-x)}$), bismuth antimony telluride ($Bi_xSb_{2-x}Te_y$) thin films were electrodeposited, followed by post annealing to create various nanocrystalline thin films. Additionally, antimony telluride nanowires were synthesized by a template-directed electrodeposition. The material, electrical, and thermoelectric properties of those metal chalcogenide nanostructures are systematically investigated to depend the effect of dimension, composition, crystallinity, crystallographic properties, and temperature for thermoelectric applications.

TABLE OF CONTENTS

LIST OF FIGURES

CHAPTER 1 Introduction: Nanostructured Thermoelectrics

1.1 Nanostructured Thermoelectrics

1.1.1 An Overview of Thermoelectrics

With the ever-rising demand throughout the world for energy consumption and CO_2 reduction, thermoelectric energy conversion has been receiving intensified attention as a potential candidate for waste-heat harvesting as well as for power generation from renewable sources. Thermoelectrics, which converts directly between heat and electricity with no moving parts, leading to simple, silent, reliable operation, is an exciting alternative for conventional energy generators. The mechanism of the thermoelectric power generation, which creates the voltage from the temperature gradient called as the Seebeck effect, is explained by charge carrier's movement in the thermoelectric materials. The production of voltage in the thermoelectric materials is based on the charge build-up from the hot-end to cold-end under the temperature gradient. Once the one side of the material exposures to the heat, the mobile charge carriers diffuse to the cold-end, resulting in a net charge. This charge build-up produces the voltage. Depending on the major carrier type, the type of the net charge is decided either negative for n-type materials or positive for p-type materials. Reversely, the thermoelectric cooler is based on the Peltier effect, which can convert the applied voltage into the temperature gradient.

The thermoelectric module consists of an array of p- and n-type semiconductor elements that are heavily doped with charge carriers. The schematic of one pair of p- and n-type element, which referred to as a thermoelectric couple for the thermoelectric power

generator and as the cooler, is indicated in Figure 1.1.[1] As shown in the Figure 1.1, the free electrons in the n-type semiconductor and free holes in the p-type semiconductor flow from hot junction to cold junction. The performance of thermoelectric effects is maximized by arranging the thermoelectric couples into the array that is electrically connected in series but thermally connected in parallel as shown in Figure 1.2.[2] Using this configuration, the higher current output and larger temperature gradient are expected due to the electrical current (power output) is driven by the heat flow.

Since the thermoelectric generators and coolers are solid-state devices without moving parts, they are silent and reliable. Moreover, an excellent scalability and long operation time allows the thermoelectric devices for various applications in vast fields (Figure 1.3). Traditionally, the solid-state thermoelectric devices have been applied to generate an amount of power for waste heat recovery, remote sensor power, and emergency power source ranging from thermocouple sensors to power generators in space missions. In addition, the thermoelectric modules can be either heater or cooler; a common application utilized is thermal cycling system such as DNA amplification, which requires high-throughput and durability under a heavy duty temperature cycle. As for well-known consumer applications, the thermoelectric modules are provided to cooling and temperature control in small size and weight electronic devices such as integrated circuit coolers and potable refrigerators.

1.1.2 Efficiency of Thermoelectrics

Efficient thermoelectric energy conversion critically depends on the performance of thermoelectric materials and devices. The efficiency of thermoelectric materials for both the power generator and the cooler is evaluated by figure-of-merit (zT), which is a dimensionless value;

$$zT = \frac{S^2\sigma}{k}T = (S^2 n)\left(\frac{\mu}{k}\right)eT, \quad where\ \sigma = ne\mu \qquad \text{Equation 1.1}$$

where S is the Seebeck coefficient, σ is the electrical conductivity, k is the thermal conductivity, n is the carrier concentration, and μ is the mobility. The thermal conductivity k is the summation of the lattice contribution k_l and electron contribution k_e. As the equation indicates, the high zT can be achieved as the material has a high Seebeck coefficient, a high electrical conductivity and a low thermal conductivity.

1.1.3 Interdependence of Thermoelectric Parameters

Enhancement of zT and/or Power factor (P.F.=$S^2\sigma$) is needed to carefully design because increasing σ generally suppresses S – meaning they typically oppose one another resulting in a net decrease in these two performance parameters. Limited success at increasing zT has been achieved by focusing on reducing k. This is thought of in terms of increasing phonon scattering within the thermoelectric materials by incorporating complex lattice structures, such as superlattices, heterostructures, and nanocomposites. For some materials, k can be taken to a minimum by placing the material in an amorphous state, but this is typically associated with a substantial drop in the charge carrier mobility, thereby in electrical conductivity, σ. This strong interdependence in the

key parameters of *zT* has taken its toll by stalling the release of new high *zT* thermoelectric devices to industry. Therefore, another approach, described in the following chapter 6, places focus on understanding and controlling mechanisms and processes that tend to de-couple key parameters and maximize the *zT* numerator, specifically, that optimize the power factor.

1.1.4 Thermoelectric Materials

The thermoelectric materials require for holding a high Seebeck coefficient (*S*), a high electrical conductivity (σ), and a low thermal conductivity (*k*) for a high thermoelectric efficiency (*zT*). The maximum of the *zT* of the thermoelectric materials is expected using the relationship of those three interdependent parameters as a function of the carrier concentration of the materials as shown in Figure 1.4.a. Good thermoelectric materials are typically heavily doped semiconductors with a carrier concentration between 10^{19} and 10^{21} cm^{-3}. According to the modeling based on experimental data from Bi_2Te_3,[3] the thermoelectric power factor $S^2\sigma$ maximizes at higher carrier concentration than *zT*. In addition, reducing the lattice thermal conductivity leads to a two-fold increase in the thermoelectric *zT*. As shown in Figure 1.4.b, an optimized *zT* of 0.8 is shown at point (1) for a model system (Bi_2Te_3) with a k_l of 0.8 $Wm^{-1}K^{-1}$ and k_e that is a function of the carrier concentration (purple). Reducing k_l to 0.2 $Wm^{-1}K^{-1}$ directly increases the *zT* to point (2). Additionally, lowering the thermal conductivity allows the carrier concentration to be re-optimized (reduced), leading to the re-optimized zT value as shown at point (3).

According to various theoretical and experimental studies, metal chalcogenides with a narrow energy band gap (E_g < 0.2 eV),[4] specifically, antimony telluride (Sb_2Te_3) and bismuth telluride (Bi_2Te_3) have been known for the best thermoelectric materials at room temperature operation (Figure 1.5). By allowing the fine tuning of the carrier concentrations through the alloy, the derivative materials including bismuth antimony telluride $(Bi_{0.5}Sb_{1.5})_2Te_3$ and bismuth telluride selenide $Bi_2(Te_{0.8}Sb_{0.2})_3$ became the most common p-type and n-type thermoelectric materials for a-near-room temperature operational thermoelectric devices. Moreover, unique anisotropic electronic properties originated from a weak van der Waals bonding between the Te atoms along the hexagonal *c*-axis of BiSbTe allowed the additional reduction of thermal conductivity and directionality on thermoelectric performance.[2,5] Specially, the bismuth antimony telluride ($Bi_xSb_{2-x}Te_y$) is anticipated as the best room temperature thermoelectric material due to the reduced thermal conductivity introduced by the substitution of Bi/Sb in the structure orders. By virtue of recently advanced nanotechnology and fabrication techniques, the enhanced zT values of 2.4 in Bi_2Te_3/Sb_2Te_3 superlattice, and zT of 1.5 in nanocrystalline BiSbTe bulk alloy were recorded at room temperature.[2,6]

1.1.5 Recent Advance in Thermoelectric Figure-of-Merit of Nanostructured Materials

Interdependent properties (e.g., Seebeck coefficient (S), electrical (σ), and thermal conductivity (k)) of the thermoelectrics still hinder the assertive utilization of thermoelectric devices in extensive industry. In order to overcome this intrinsic demerit,

numerous researches endeavored to independently control those interdependent parameters. Historical approaches to enhance the *zT* have been focused to independently engineer the phonon scattering mechanism, called phonon-glass electron-crystal (PGEC), by introducing complex lattice structures such as skutterudites, superlattices, heterostructure, and nanocomposites. The enhancement of thermoelectric *zT* in these systems was mainly achieved by the reducing the thermal conductivity due to the increased phonon scattering at the interfaces. For example, a peak *zT* of 1.4 at 100 ^{o}C was observed using a p-type nanocrystalline BiSbTe bulk alloy, which prepared by hot pressing nanopowders that were ball-milled from crystalline ingots (Figure 1.6).[7] According to Poudel *et al.*, this successful achievement was originated from the increased phonon scattering at the interfaces created by the nano-grains, therefore, the drastic reduction of the thermal conductivity was compared to its single crystal ingot. Not only in the bulk alloy, the engineered lattice structures of Bi_2Te_3/Sb_2Te_3 and GaAs/AlGaAs forming the supperlattices configuration also demonstrated the empirical results in the reduced thermal conductivity, thus, the enhanced *zT* of 2.4 at 300 K and, respectively (Figure 1.7).[4,8]

Nevertheless the decreased thermal conductivity allowed the *zT* improved, there is theoretical limit for reducing the thermal conductivity as amorphous level and also compensation for the mobility decrease. Therefore, it is inevitable for efforts to enhance the Seebeck coefficient without damaging the electrical conduction, thereby, expecting the enhanced power factor (P.F.=$S^2\sigma$). Recent advancements in this strategy have been achieved by incorporating metallic and/or semiconducting nanoparticles in thermoelectric

materials. The distortions of the density of states (DOS) near Fermi level as results of carrier localization, resonant state, and carrier filtering effect fulfilled the sharp increase of the Seebeck coefficient without suppressing electrical conductivity.[9-11] As shown in Figure 1.8, the large Seebeck coefficient can be dependent on the behavior of the scattering rates ($1/\tau$) as a function of energy in the materials.[12] The $1/\tau$, which is inverse function of the energy dependence of the relaxation times ($\tau = \tau_0 E^r$), where the exponent r is called the scattering parameter. This scattering parameter, which is determined by different scatterings for example, in the case of acoustic phonon scattering, the r is -1/2, and weak impurity scattering, the r is 3/2. Therefore, an increase of the scattering parameter leads to an increase in the slope of the differential conductivity, thus also in the Seebeck coefficient.

Recently, it is known that interfacial energy barrier scattering of charge carriers is an effective method to enhance the Seebeck coefficient. It is often called the energy filtering effect where the creation of band bending induced by charge transfer at the interfaces can cause the energy-dependent scattering of charge carriers. In the concrete, the created interfaces on charge carrier pathways can generate a barrier height (potential, E_b) at which the low energy charge carriers are scattered but the high energy charge carriers pass through. This strong energy-dependent charge scattering leads to increase in the Seebeck coefficient because of its dependence on the energy derivative of the relaxation time at the Fermi energy;

$$S = \frac{\pi^2 {k_B}^2 T}{3e}\left(\frac{\partial lnN(E)}{\partial E} + \frac{\partial ln\tau(E)v(E)^2}{\partial E}\right)_{E_F} \qquad \text{Equation 1.2}$$

$$\tau^{-1}(E) = \frac{{V_b}^2 x}{R} E^{-3/2} = \frac{e\mu}{m^*} \qquad \text{Equation 1.3}$$

where $N(E)$ is the density of the states, $\upsilon(E)$ is the average charge velocity, $\tau(E)$ is the carrier scattering relaxation time, and m^* is the effective mass of the carrier. In addition, as indicated in Eq. 1.3 the carrier relaxation time is inversely proportional to the barrier potential (V_b), therefore, adjusting the effective height in a potential barrier can be another variable to maximize the Seebeck coefficient.

Various theoretical and experimental results have probed the significant enhancement of the *zT* by utilizing the energy filtering effect in thermoelectric materials. As proposed by Faleev *et al.* where the concept of band bending at metal/semiconductor interfaces demonstrated the enhancement of the Seebeck coefficient as a result of strong energy dependent electron scattering (Figure 1.9), the incorporation of metal nanoparticles was selected as experimental approaches.[13] For example, Ko *et al.* and Zhang *et al.* introduced the metal Pt and Ag nanoparticles in the Sb_2Te_3 films, respectively, and represented the enhancement of Seebeck coefficient without losing the conductivity of the Sb_2Te_3 (Figure 1.10).[14,15] According to Sumithra *et al.*, the incorporation of semimetal Bi nanoparticles in nanostructured Bi_2Te_3 also revealed the enhanced Seebeck coefficient at given carrier concentrations and the reduced lattice thermal conductivity, thus, the increase in the bulk Bi_2Te_3 *zT* by a factor of 2 from 0.2 to 0.4 (Figure 1.11).[16] Moreover, it was claimed that this strong energy-dependent charge scattering mechanism is not only valid at the interfaces created between metal or semimetal and semiconductors.[17] Martin *et al.* demonstrated the enhanced Seebeck coefficient in nanocrystalline PbTe bulk system using the effective grain-boundary potential-barrier scattering.[18] According to them, the low energy charge carriers are

impeded at the grain boundaries of nanocrystals where the energy barriers are formed to trap the charge carriers. Similar behavior was also observed in the thermoelectric performance study using the Sb_2Te_3 nanoparticles by Chen *et al.* (Figure 1.12).[19] As the size of nanoparticle decreased the Seebeck coefficient of the films increased at given carrier concentration which was also understood as a result of the energy filtering effect due to the charge carrier trapped in the grain boundaries.

1.2 Research Objectives

The goal of this work is to fabricate metal chalcogenide nanostructures with outstanding performances for thermoelectric applications. To accomplish this aim, diverse nanocrystalline metal chalcogenides (i.e., Sb_2Te_3, Bi_2Te_3, Ag-doped Sb_2Te_3, $AgSbTe_2$, $Bi_{0.5}Sb_{1.5}Te_3$) known for the high-thermoelectric performance near room temperature, are selected as candidates to study. As for synthesis approach, the electrodeposition, which is one of the most versatile and easiest solution-based synthesis techniques for low dimensional nanostructures in a cost effective and scalable manner, is utilized to achieve one- and two-dimensional (1- and 2-D) nanocrystalline metal chalcogenides. Enhancement of electrical transport and thermoelectric properties are proposed by controls over the dimension, crystallinity, crystal structure, foreign metal (i.e., Ag) doping, and nanocomposite with secondary phases.

The specific aims of this work are the following:

1) Synthesize chalcogenide binary Sb_xTe_y, silver-doped Sb_xTe_y, Bi_xTe_y, ternary $Ag_xSb_{2-x}Te_{3-x}$, and $Bi_xSb_{2-x}Te_y$ thin films and nanowires by using potentiostatic electrodeposition and template-directed electrodeposition, respectively. Investigate the effect of electrodeposition parameters (i.e., applied potential and electrolyte concentration) on the morphology, composition, crystallinity, and crystallographic properties of the 1-D and 2-D nanostructures.

2) Characterize electrical conductivity, magnetoresistance, carrier concentration, mobility, and Seebeck coefficient by using FET-measurement and Hall-measurement for the 1-D and 2-D nanostructures, respectively.
3) Optimize material, electrical, and thermoelectric properties by manipulating the grain size and embedded secondary phases of nanocrystalline chalcogenide nanostructures using a post-annealing treatment.
4) Observe the effect of metal doping on the transport and thermoelectric properties.

1.3 Thesis Organization

This thesis is organized as follow:

Chapter 2 demonstrates the enhancement of thermoelectric properties of nanocrystalline Sb_2Te_3 electrodeposits by creating γ-SbTe/Sb_2Te_3 nanocomposite, where γ-SbTe nanoinclusions are embedded in a nanocrystalline Sb_2Te_3 matrix. The enhancement of Seebeck coefficient without reducing its conductivity is explained by a carrier energy filtering effect due to the band bending at the two-phase interfaces, which is also manifested by measuring their difference in the valence band. As an extension, Chapter 3 describes the approach to augment the thermoelectric performance of nanocrystalline Sb_2Te_3 thin films by controlling energy filtering effects (i.e., barrier heights) occurring at both grain boundaries and at an induced embedded second-phases (i.e., Te element and γ-SbTe) within a grain. Such adjustment in the interfacial energy-barrier scatterings allows optimizing the thermoelectric performance in the nanocrystalline Sb_2Te_3 system using the energy filtering effect. For the studies in the chapter 2 and 3, a facile but high precision composition-controlled electrodeposition technique is selected to synthesize various compositions of amorphous Sb-Te solid solutions which are readily crystallized by post annealing treatments selectively forming thermodynamically favored phases, including single-phase nanocrystalline Sb_2Te_3 and crystalline nanocomposites Te/Sb_2Te_3 or γ-SbTe/Sb_2Te_3. Solution composition and post-annealing profiles are used to control the single-phase grain size, thereby the grain-boundary potential-barrier, at a given carrier concentration as well as the nature of the embedded second-phase. Chapter 4 shows the effect of Ag-doping in the nanocrystalline

Sb_2Te_3 thin films on the electrical and thermoelectric properties. Not only the Ag-doping level, the modulated crystallographic properties such as crystallinity, preferred orientation, and composition provides the understanding of their correlations to improve the electrical and thermoelectric properties of the nanocrystalline Sb_2Te_3 thin films. Chapter 5 demonstrates the effect of the composition and microstructure changes on the electrical and thermoelectric properties of antimony telluride (Sb_xTe_y) nanowires to determine the optimum conditions that give the highest thermopower. For a systematical study, a facile template-directed electrodeposition technique was utilized to prepare amorphous Sb_xTe_y nanowires with well-controlled dimension and composition. Composition-dependent phase transition behavior of the nanowires, corresponding to the amorphous-to-crystalline solid state transition, was investigated by measuring their electrical resistivity changes in addition to their FET-mobility, activation energy, and Seebeck coefficient changes as well. Chapter 6 and 7 describe the synthesis and characterization of ternary nanocrystalline silver antimony telluride ($Ag_xSb_{2-x}Te_{3-x}$) and bismuth antimony telluride ($Bi_xSb_{2-x}Te_y$) thin films by potentiostatic electrodeposition followed by a post annealing treatment for thermoelectric applications. The measurement of electrical transport and thermoelectric properties as a function of the composition and crystallographic properties are indicated to evaluate the roles of chemical composition and structural defects in those ternary systems, which are known as the best-room temperature thermoelectric materials.

1.4 References

[1] P. Pichanusakorn, and P. Bandaru, *Nanostructured thermoelectrics*, Materials Science and Engineering R, 2010, **67**: p.19.

[2] G. J. Snyder, and E. S. Toberer, *Complex thermoelectric materials.* Nature materials, 2008. **7**: p. 105.

[3] D. M. Rowe, and G. Min, *Alpha-plot in sigma-plot as a thermoelectric-material performance indicator.* Journal of Materials Science Letters, 1995. **14**: p. 617-619.

[4] R. Venkatasubramanian, E. Siivola, T. Colpitts, and B. O'Quinn, *Thin-film thermoelectric devices with high room-temperature figures of merit.* Nature, 2001. **413**(6856): p. 597-602.

[5] J. P. Wiff, Y. Kinemuchi, H. Kaga, C. Ito, and K. Watari, *Correlations between thermoelectric properties and effective mass caused by lattice distortion in Al-doped ZnO ceramics.* Journal of the European Ceramic Society, 2009. **29**(8): p. 1413-1418.

[6] H. Böttner, G. Chen, and R. Venkatasubramanian, *Aspects of thin film superlattice thermoelectric materials, devices, and applications.* MRS Bulletin, 2006. **31**.

[7] B. Poudel, Q. Hao, Y. Ma, Y. Lan, A. Minnich, B. Yu, X. Yan, D. Wang, A. Muto, D. Vashaee, X. Chen, J. Liu, M. S. Dresselhaus, G. Chen, and Z. Ren, *High-Thermoelectric Performance of Nanostructured Bismuth Antimony Telluride Bulk Alloys.* Science, 2008. **320**(5876): p. 634-638.

[8] V. Narayanamurti, H. L. Störmer, M. A. Chin, A. C. Gossard, and W. Wiegmann, *Selective Transmission of High-Frequency Phonons by a Superlattice: The "Dielectric" Phonon Filter*. Physical Review Letters, 1979. **43**(27): p. 2012-2016.

[9] K. F. Hsu, S. Loo, F. Guo, W. Chen, J. S. Dyck, C. Uher, T. Hogan, E. K. Polychroniadis, and M. G. Kanatzidis, *Cubic AgPbmSbTe2+m: Bulk Thermoelectric Materials with High Figure of Merit.* Science, 2004. **303**(5659): p. 818-821.

[10] G. Zeng, J. M. O. Zide, W. Kim, J. E. Bowers, A. C. Gossard, Z. Bian, Y. Zhang, A. Shakouri, S. L. Singer, and A. Majumdar, *Cross-plane Seebeck coefficient of ErAs:InGaAs/InGaAlAs superlattices.* Journal of Applied Physics, 2007. **101**(3): p. 034502.

[11] J. M. O. Zide, D. Vashaee, Z. X. Bian, G. Zeng, J. E. Bowers, A. Shakouri, and A. C. Gossard, *Demonstration of electron filtering to increase the Seebeck coefficient in In0.53Ga0.47As/ In0.53Ga0.28Al0.19As superlattices.* Physical Review B, 2006. **74**: p. 205335.

[12] M. Zebarjadi, K. Esfarjani, M. S. Dresselhaus, Z. F. Ren, and G. Chen, *Perspectives on thermoelectrics: from fundamentals to device applications.* Energy & Environmental Science, 2012. **5**(1): p. 5147-5162.

[13] S. V. Faleev, and F. Léonard, *Theory of enhancement of thermoelectric properties of materials with nanoinclusions.* Physical Review B, 2008. **77**(21): p. 214304.

[14] D. K. Ko, Y. Kang, and C. B. Murray, *Enhanced Thermopower via Carrier Energy Filtering in Solution-Processable Pt–Sb2Te3 Nanocomposites.* Nano Letters, 2011. **11**(7): p. 2841-2844.

[15] Y. Zhang, M. L. Snedaker, C. S. Birkel, S. Mubeen, X. Ji, Y. Shi, D. Liu, x. Liu, M. Moskovits, and G. D. Stucky, *Silver-Based Intermetallic Heterostructures in Sb2Te3 Thick Films with Enhanced Thermoelectric Power Factors.* Nano Letters, 2012. **12**(2): p. 1075-1080.

[16] S. Sumithra, N. J. Takas, D. K. Misra, W. M. Nolting, P. F. P. Poudeu, and K. L. Stokes, *Enhancement in Thermoelectric Figure of Merit in Nanostructured Bi2Te3 with Semimetal Nanoinclusions.* Advanced Energy Materials, 2011. **1**(6): p. 1141-1147.

[17] D. Narducci, E. Selezneva, G. Cerofolini, S. Frabboni, and G. Ottaviani, *Impact of energy filtering and carrier localization on the thermoelectric properties of granular semiconductors.* Journal of Solid State Chemistry, 2012. **193**(0): p. 19-25.

[18] J. Martin, Li. Wang, L. Chen, and G. S. Nolas, *Enhanced Seebeck coefficient through energy-barrier scattering in PbTe nanocomposites.* Physical Review B, 2009. **79**(11): p. 115311.

[19] J. Chen, T. Sun, D. Sim, H. Peng, H. Wang, S. Fan, H. H. Hng, J. Ma, F. Y. C. Boey, S. Li, M. K. Samani, G. C. K. Chen, X. Chen, T. Wu, and Q. Yan, *Sb2Te3 Nanoparticles with Enhanced Seebeck Coefficient and Low Thermal Conductivity.* Chemistry of Materials, 2010. **22**(10): p. 3086-3092.

[20] R. Venkatasubramanian, T. Colpitts, B. O'Quinn, S. Liu, N. El-Masry and M. Lamvik, *Low-temperature organometallic epitaxy and its application to superlattice structures in thermoelectrics*. Applied Physics Letters, 1999. **75**: p. 1104-1106.

.

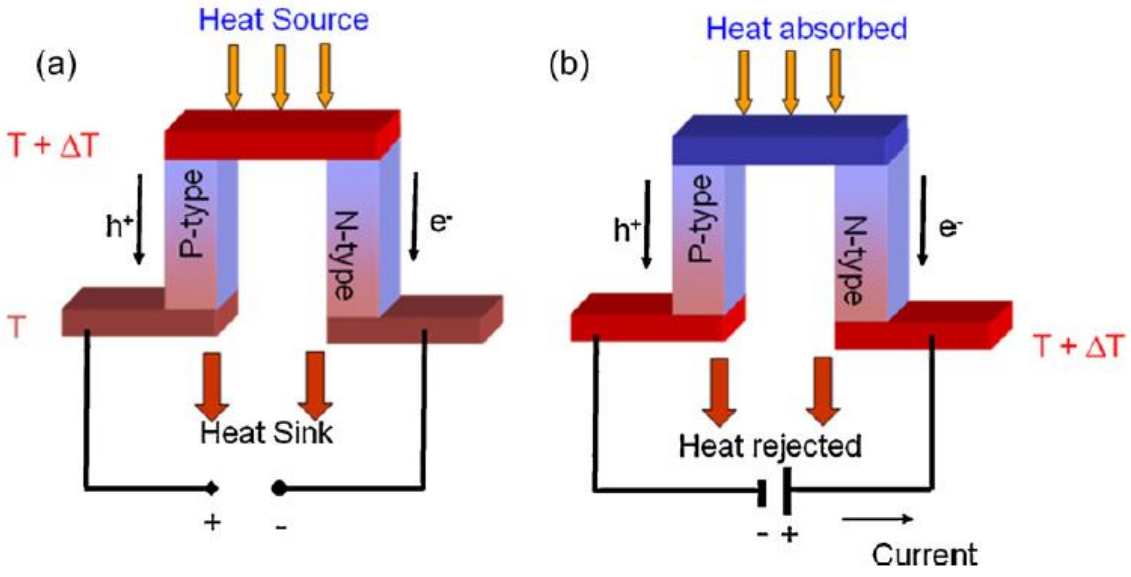

Figure 1.1 Basic thermoelectric devices for (a) heat-to-electrical energy conversion, and (b) heat pumping. The couple is comprised of p- and n-type semiconductors. In practice, many such elements are chained in series to yield desired power levels.[1]

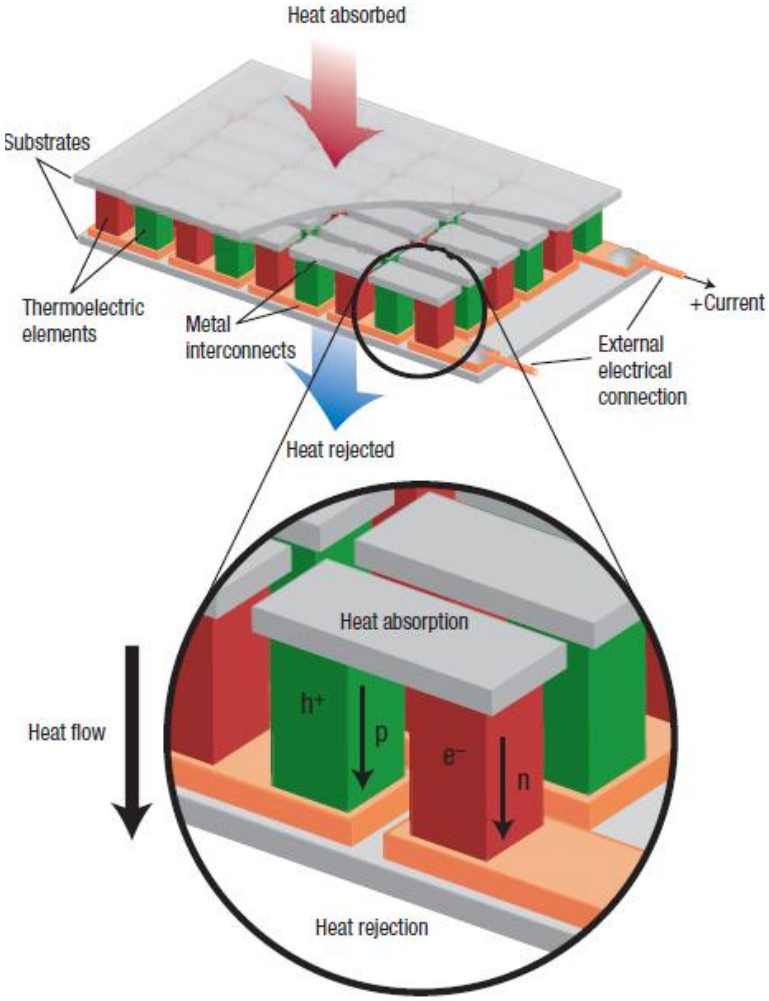

Figure 1.2 Thermoelectric module showing the direction of charge flow on both cooling and power generation.[2]

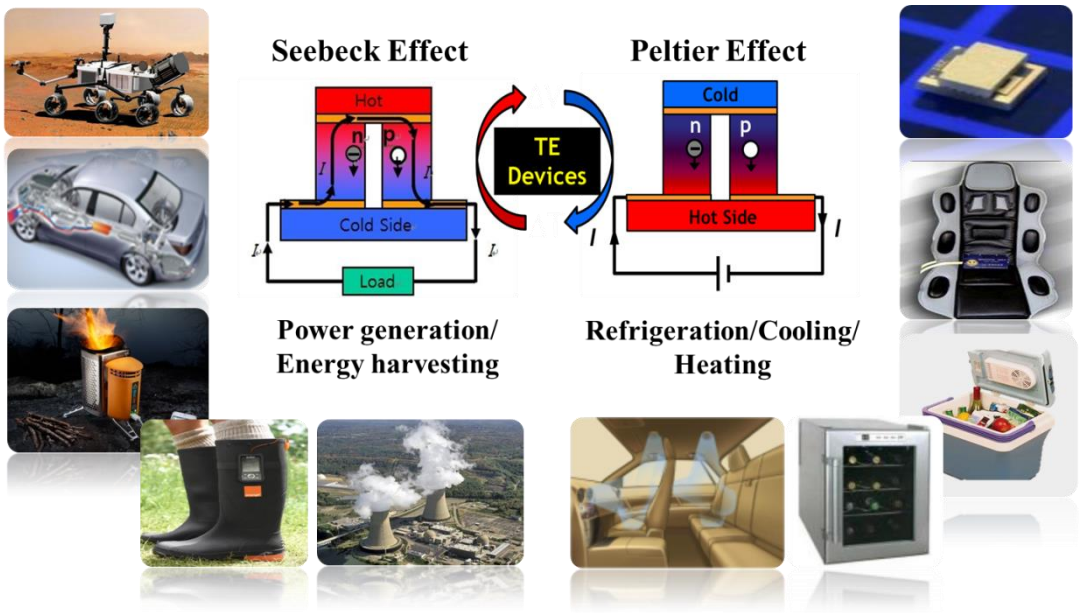

Figure 1.3 Applications of thermoelectric devices in various commercial fields.

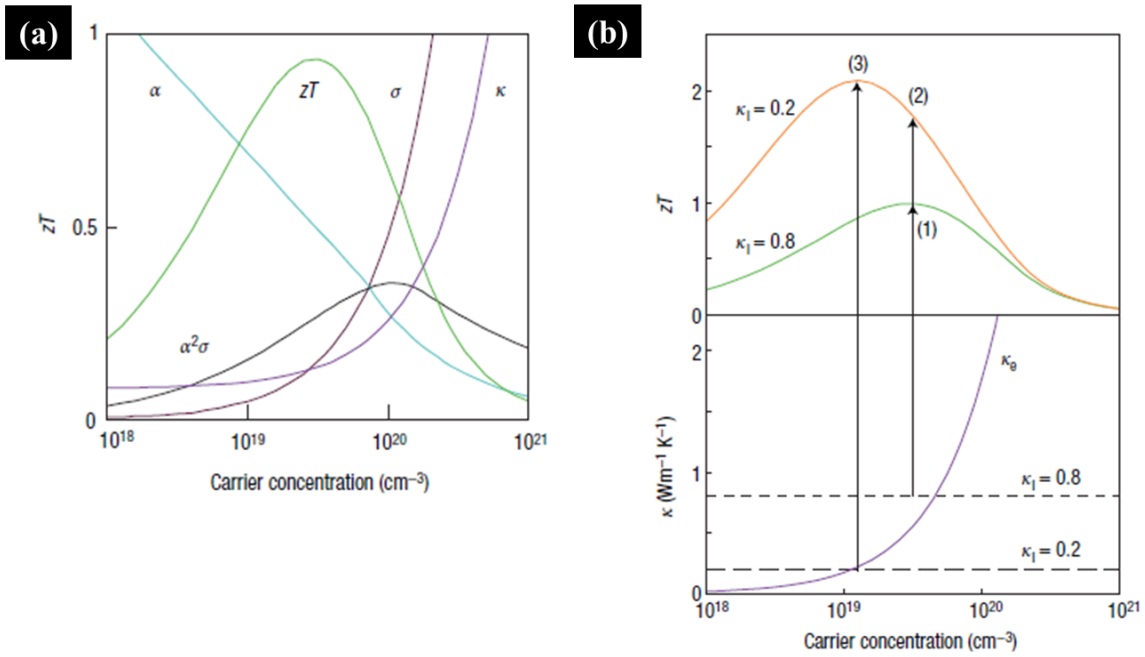

Figure 1.4 Optimizing zT through carrier concentration tuning.[2]

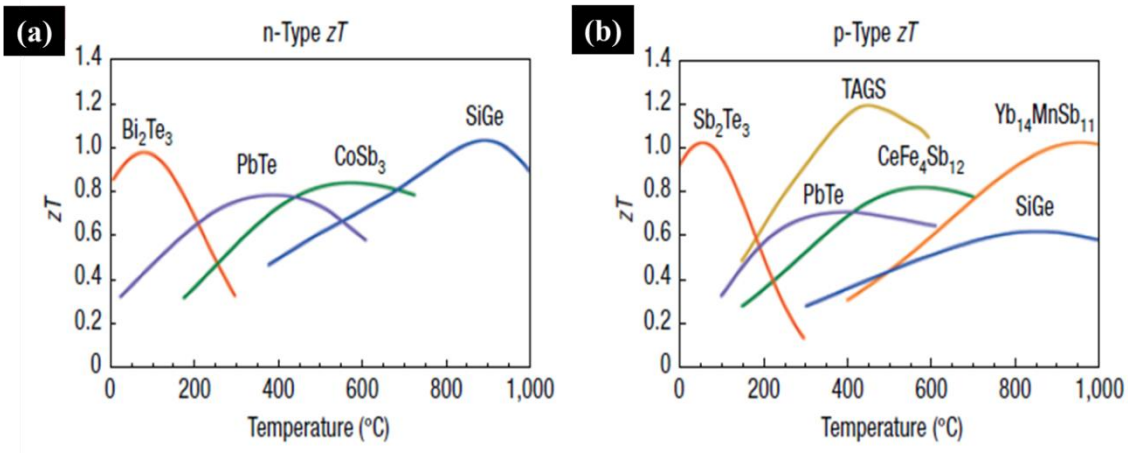

Figure 1.5 zT of state-of-the-art commercial materials and those used or being developed by NASA for thermoelectric power generation. n-type (a) and p-type (b).[2]

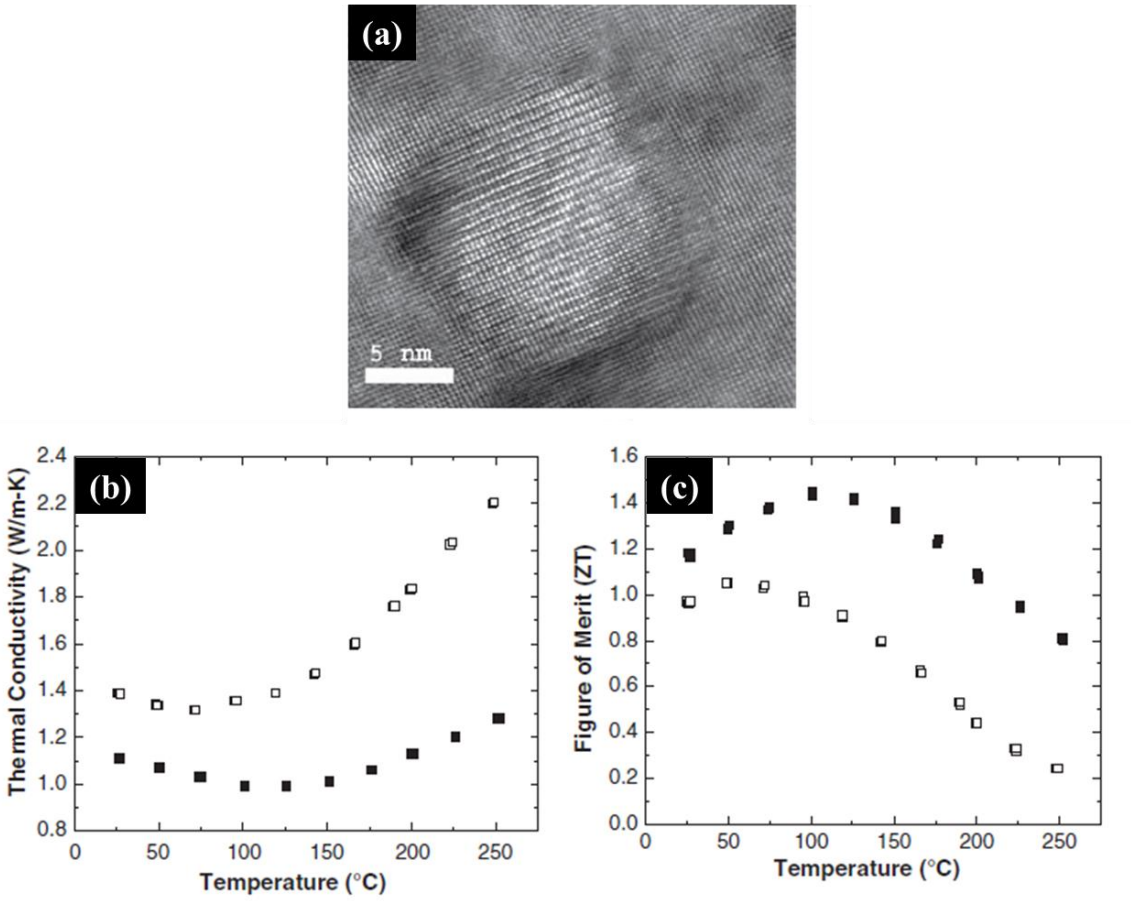

Figure 1.6 Enhancement of zT of nanocrystalline BiSbTe bulk alloy: High-magnification TEM image showing the nanodots in the matrix of BiSbTe alloy (a), thermal conductivity (b) and zT (c) of SOD ingot (open symbol) and nanocrystalline (solid symbol) as a function of temperature. [7]

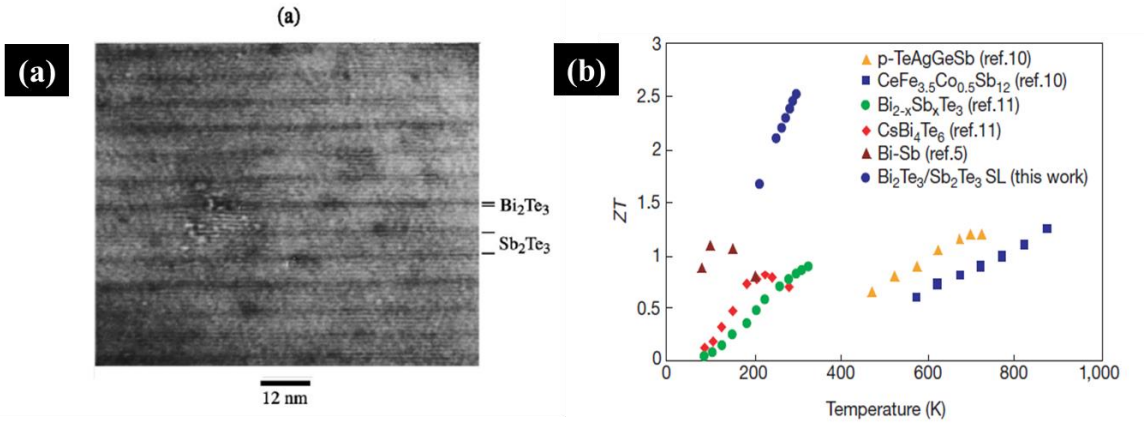

Figure 1.7 Epitaxy of hexagonal-phased Bi_2Te_3/Sb_2Te_3 superlattices by metal organic chemical vapor deposition (MOCVD) (a).[20] Temperature dependent *zT* of 10Å /50Å p-type Bi_2Te_3/Sb_2Te_3 superlattice compared to several recently reported materials (b).[4]

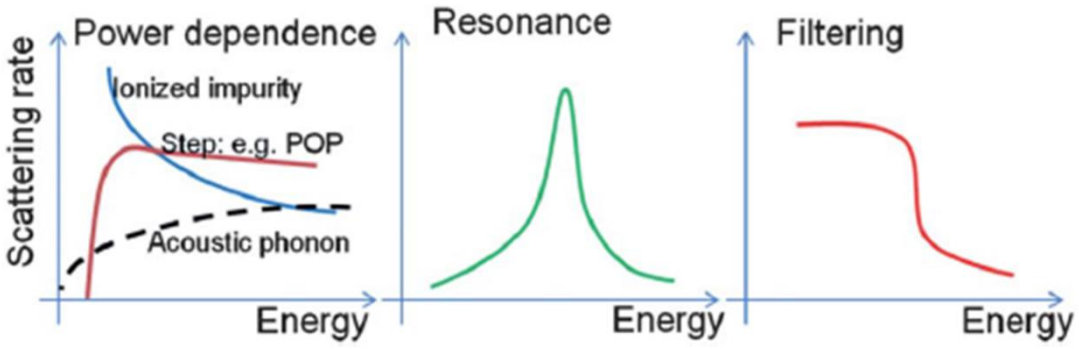

Figure 1.8 Several possible behaviors of total relation rate ($1/\tau(E)$) in a few k_BT window.[12]

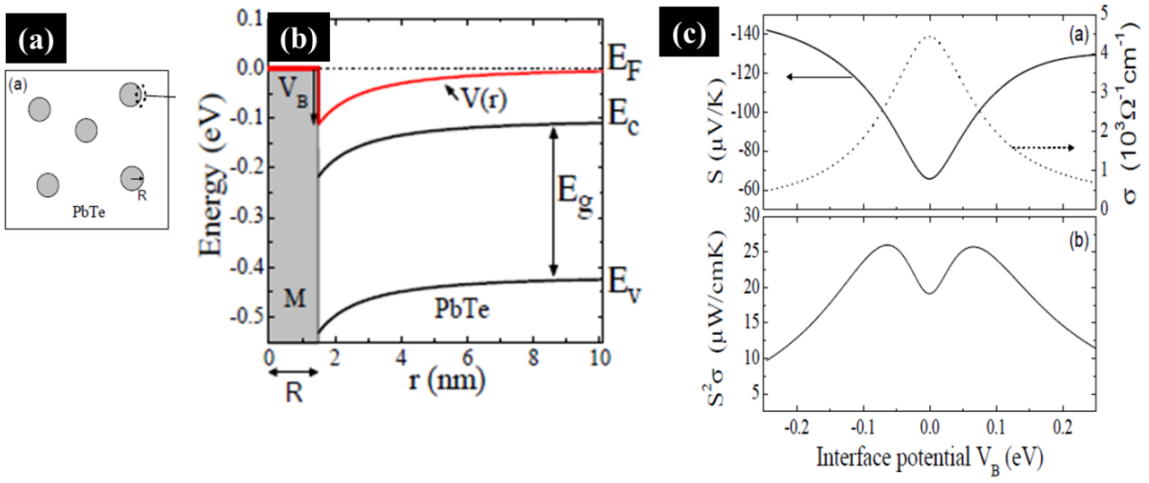

Figure 1.9 Schematic of the semiconductor host with metallic nanoinclusions (a). Calculated potential V(r) and the energy diagram for PbTe at T=300K, n=2.5x10^{19} cm^{-3}, V_B=-0.11eV, and R=1.5 nm (b). The calculated Seebeck coefficient and conductivity for PbTe as a function of the interface potential VB with the resulting power factor (c). The parameters are R=1.5 nm, T=300K, x=5%, and n=2.5x10^{19} cm^{-3}.[13]

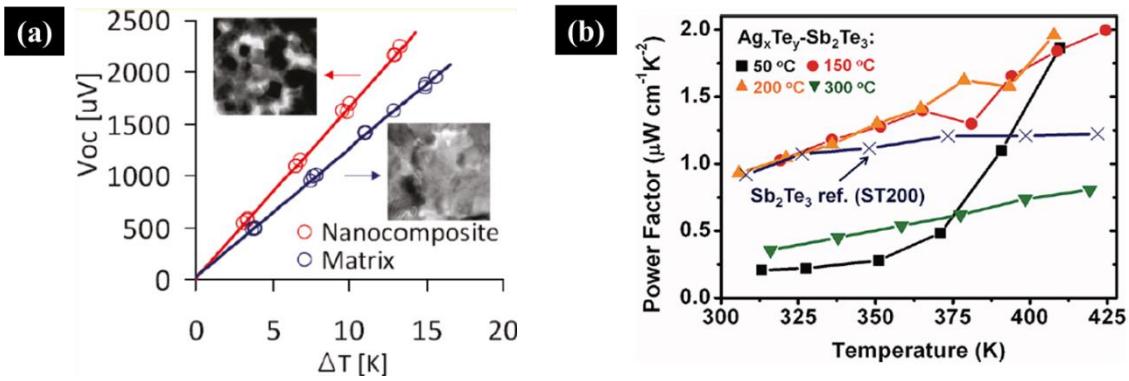

Figure 1.10 Open-circuit voltage vs. temperature difference for Pt-Sb_2Te_3 composite and matrix measured at room temperature (a).[14] Temperature dependence of power factor of Ag_xTe_y-Sb_2Te_3 (b).[15]

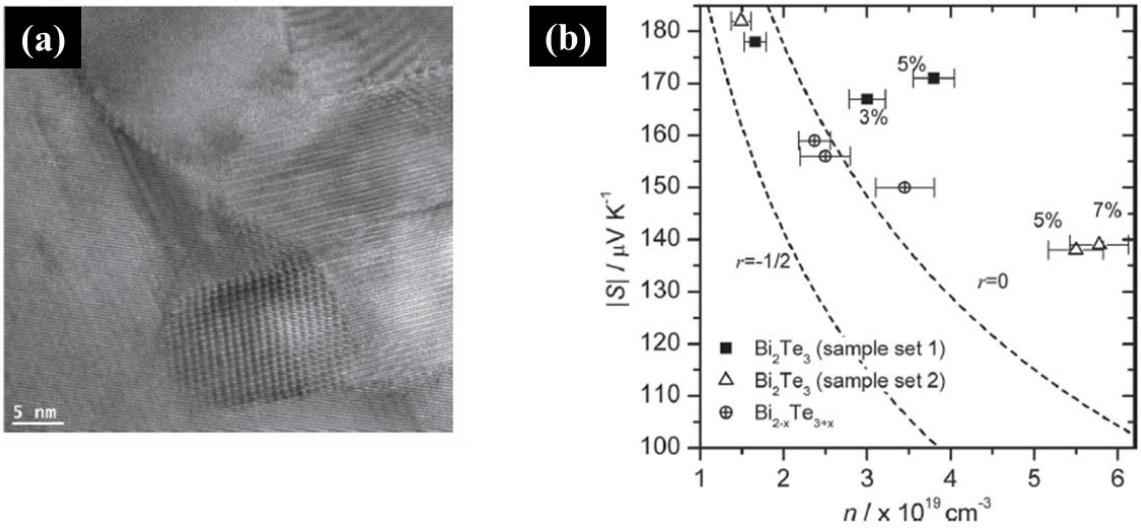

Figure 1.11 High resolution transmission electron micrograph of 5 % Bi incorporated Bi_2Te_3 nanocomposite (a). Seebeck coefficient as a function of carrier concentration for Bi_2Te_3/Bi nanoparticle composites (b).[16]

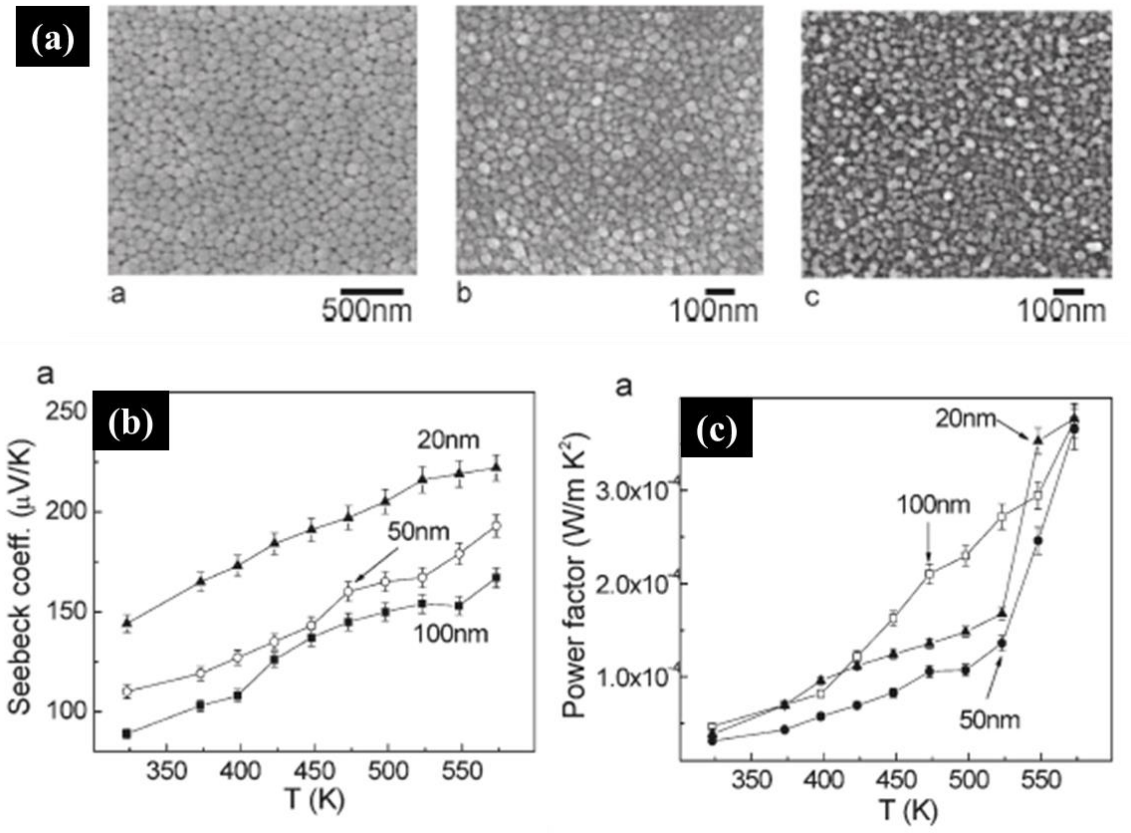

Figure 1.12 SEM images of Sb_2Te_3 nanoparticles (a), temperature dependent Seebeck coefficient (b) and power factor (c) of films with various diameters.[19]

CHAPTER 2 Maximizing Thermoelectric Properties by Nanoinclusion of γ-SbTe in Sb2Te3 Film via Solid-State Phase Transition from Amorphous Sb-Te Electrodeposits

2.1 Abstract

In this work, we demonstrate an enhancement of thermoelectric properties by creating γ-SbTe/Sb_2Te_3 nanocomposite film, where γ-SbTe nanoinclusions are embedded in a nanocrystalline Sb_2Te_3 matrix. The two-phase nanocomposite was formed via solid-state phase transition using an amorphous Sb_2Te_3 electrodeposits as the starting materials. The crystallinity and crystal structure of intermediate states during the amorphous-crystalline solid-state transformation were characterized by sequentially annealing the sample. The formation of the γ-SbTe is attributed to the different enthalpy of mixing for the bonding structures available in the Sb-Te system. Room temperature measurement of electrical and thermoelectrical properties as a function of annealing temperature revealed that the two-phase system provided the carrier energy filtering effect at the interfaces between two phases, leading to enhanced Seebeck coefficient without affecting its electrical transport properties. The band bending at the two-phase interfaces was indirectly manifested by measuring their difference in the valence band, advocating the possibility of a strong energy-dependent charge scattering to the enhanced Seebeck coefficient.

2.2 Introduction

The energy conversion efficiency of thermoelectric (TE) devices depends on the temperature extremes across the device and on a figure-of-merit defined by $zT = S^2\sigma T/\kappa$, where S, σ, T, and κ are the Seebeck coefficient, electrical conductivity, temperature, and thermal conductivity, respectively. The first two terms in the zT define the power factor P.F. = $S^2\sigma$. Thus, enhancing the TE efficiency can be realized by reducing κ while enhancing S and σ. However, careful design is needed to enhance zT and/or P.F. because increasing σ generally suppresses S – meaning they typically oppose one another resulting in a net decrease in these two performance parameters. Therefore, the key strategy is to implement mechanisms that decouple opposing thermoelectric properties; namely, decouple S and σ, κ and σ, and κ and S. Recent advancements in this strategy have been achieved by incorporating metallic and/or semiconducting nanoparticles in TE materials. Nanoinclusions in TE materials have a wide range of effects; including, reducing thermal conductivity by increasing phonon scattering at interfaces, altering the effective mass of charge carriers by changing the energy surface profile (*i.e.*, density of states- DOS engineering) near the Fermi level, and enhancing the Seebeck coefficient by means of an energy filtering effect (EFE). The EFE is due to a strong energy-dependent charge scattering originating from interface potential barriers induced by doping, structural defects, and grain boundaries as well. The EFE has the potential to sharply enhance S without appreciable suppression in σ - making it an effective mechanism that decouples S and σ.[1-9] The formation of the effective height of potential barriers introduced by foreign elements or lattice defects in TE materials has been studied

theoretically and proven experimentally to enhance thermoelectric properties. Examples include the ErAs:InGaAs/InGaAlAs superlattices, the incorporation of metal nanoparticles (*e.g.,* Ag, Pt), and the precipitation of hetero-nanocomposites, such as Te in Sb_2Te_3 and PbSe in PbTe.

Antimony telluride (Sb_2Te_3) and its derivatives (e.g. $Bi_{0.5}Sb_{1.5}Te_3$ and $AgSbTe_2$) have attracted attention due to their high performance levels in diverse applications such as TE devices, phase change memory (PCM), and recently in topological insulators (TI). Specifically, the Sb_2Te_3 is a well-known p-type TE material operable at room temperature. However, due to the similar electronegativity of Sb and Te atoms, the major anti-site defects yield a relatively low Seebeck coefficient (*i.e.,* 38~83 μV/K) at room temperature.[10] The general attention over the last few years to enhance the Seebeck coefficient of Sb_2Te_3 has been placed on a post-annealing process which reduces native defects and increases grain size. These changes are anticipated to enhance both σ and the P.F. by increasing the charge carrier mobility while reducing its concentration.[9,11-13] Recently, motivated by the strategy of using the EFE to decouple *S* and *σ*, the nanoinclusions such as Pt, Ag, and Te in Sb_2Te_3 films have proved the enhanced Seebeck coefficient by representing the increased effective mass values.[2,4,9] The synthesis techniques to incorporate those nanoinclusions were assorted, for example, just mixing the nanoparticles during the synthesis process of Sb_2Te_3 films or precipitating within the Sb_2Te_3 film by post-annealing process. Although these studies showed the improved Seebeck coefficient, however, the addition of extra elements in the Sb_2Te_3 inevitably affected its transport property which also determines the entire thermoelectric

performance. It is known that the metal incorporation in the semiconductor materials is irresistible to increase the carrier concentration. This is counter effect on Seebeck coefficient due to their interdependence. Instead of metals, however, if we can embed the materials such that have similar material properties to host materials, this negative compensation can be impeded. Moreover, the current synthesis techniques to incorporate nanoinclusions require extreme environmental conditions such as high power, long processing time, and the use of toxic chemicals such as hydrazine and capping ligands. These requirements will challenge any practical scale-up in manufacture. Only a few studies have been reported on the EFE effect on the TE properties without the incorporation of foreign elements to introduce the potential barriers; therefore, it is important to explore alternative ways to achieve the effective height of the potential barriers.

Electrodeposition is one of the most versatile and easiest techniques that can overcome the drawbacks of other methods in a cost effective and scalable manner. Stable and/or meta-stable films with precision control over dimension, chemical composition, morphology and degree of crystallinity can be achieved by simply varying electrodeposition parameters such as applied potential, electrolyte concentration, temperature, agitation, and additives. In particular, the electrodeposition of a non-equilibrium reaction has successfully synthesized one- and two-dimensional Sb_2Te_3 nanostructures with excellent control over composition and crystallinity.[2,14-18] Thus, the key strategy to decouple opposing thermoelectric properties so to maximize the P.F. must now be extended to a better understanding of the amorphous-crystalline solid-state

phase transition. Furthermore, it calls for a better understanding of how these structural and compositional changes interrelate with carrier type, mobility, density of states, and the EFE. Currently, there is only a poor understanding regarding the kinetics of Sb-Te crystallization and no correlation to the transport or thermoelectric properties.

In this report, we investigated enhancements in the thermoelectric properties of Sb_2Te_3 nanocomposites. The electrodeposition was utilized to prepare amorphous Sb_2Te_3 thin films with controlled composition followed by a post-annealing process to tailor the crystallinity and crystal structure of the solid-state phase transition from the amorphous to the fully crystalline state. The electrical conductivity, Hall mobility, carrier concentration and Seebeck coefficient were measured and correlated with the structural changes as determined by X-ray under various temperature annealing profiles. Thorough analysis of the data revealed that the enhancements in the Seebeck coefficient and power factor correlated with the formation of an intermediate two-phase nanocomposite that appeared when annealed between 70 to 100 ^{o}C. It is proposed that this two-phase system provided the carrier energy filtering effect at the interfaces between the phases leading to the enhancements. From this observation, the formation of a two-phase mixture is believed to be the key to efficient enhancement of thermopower.

2.3 Experimental Section

2.3.1 Synthesis of Sb_2Te_3 Films

Details of our electrodeposition process where we use applied potential and electrolyte concentration to control the morphology, and chemical composition of deposited films

can be found in our previous papers where we synthesized Sb-Te thin films[2,16] and nanoribbons.[17] In this work, Sb_2Te_3 thin films were potentiostatically electrodeposited where the electrolyte was prepared by separately dissolving a 2.4 mM TeO_2 in a 1 M HNO_3 solution and a 3.6 mM Sb_2O_3 in a 33 mM L-tartaric acid solution at 60 ^oC. The dissolved solutions were then mixed together and deionized water was added to reach final volume of 1 L. The working electrode was e-beam evaporated using Au (80 nm)/Ni (20 nm) films on a Si substrate, and a Pt coated titanium electrode and a saturated calomel electrode (SCE) were used as the counter and reference electrodes, respectively. A potential of -0.1 V (V vs. SCE) was applied for 10 minutes and the electrolyte was kept at 25 ^oC and magnetically stirred at 300 rpm. The deposited film was amorphous, dense, and smooth 2 cm in diameter with a uniform thickness of 1 μm and with a composition Sb_2Te_3.

2.3.2 Sample Preparation

For electrical and thermoelectric characterization, the thin films were transferred from the Au/Ni/Si substrate to a non-conductive Torr Seal epoxy substrate (Varian Vacuum Products, Lexington, Massachusetts). The entire film was successfully transferred without cracking (see ref. 2 for transfer details). The final dimensions of the sample for characterization were 1 cm^2.

2.3.3 Characterization

Morphology and composition of the synthesized Sb_2Te_3 thin films were analyzed by scanning electron microscopy (SEM) (Jeol, JSM-5800) and energy dispersive X-ray spectroscopy (EDS). Crystallinity of the films was investigated by X-ray diffraction (XRD) (Bruker D8 ADVANCE). The valence bend of the films were determined by ultraviolet photoelectron spectroscopy (UPS) measurements on an AXIS-NOVA spectrometer (KRATOS Inc.) with He I emission (21.22eV). The crystallinity and crystal structure of intermediate states during the amorphous-crystalline solid-state transformation were characterized by sequentially annealing the sample under various temperatures ranging between 30 to 200 ^oC for 30 min in a nitrogen atmosphere with 5 % hydrogen present. The electrical conductivity, Hall mobility, and carrier concentration of the film were investigated by a custom-made Hall measurement unit in the van der Pauw configuration with four-point probes. The Seebeck coefficient was determined by a custom-made Seebeck measurement system by plotting the measured Seebeck voltages as a function of temperature difference (<2 ^oC) across the sample ($S = \Delta V/\Delta T$).

2.4 Results and Discussion

Figure 2.1 depicts the anticipated solid-state phase transitions driven by external thermal energy in accordance with the crystallization kinetics of a binary Sb-Te system.[19] Schematic of the experimental design strategy to achieve γ-$SbTe/Sb_2Te_3$ nanocomposites from amorphous Sb-Te films is shown in Figure 2.1a. Controlled annealing condition enables the as-deposited amorphous film to form the intermediate mixed two-phase

nanocomposites. The co-existence of the two phases attracted our attention and motivated us to more thoroughly determine if this two-phase system can provide the carrier energy filtering effect at the interfaces between the phases. It is highlighted that instead of embedding foreign elements, the inclusion of the material that is readily different from its component stacking-layer order or number would not significantly alter the host material's transport properties but only the energy-dependent charge scattering at the interfaces. Moreover, consisted of nano-sized grains, in addition to incorporated γ-SbTe between grain boundaries as defects, might represent the energy filtering effect from the synergetic scattering.[20]

The amorphous Sb-Te thin film with the uniform thickness of 1 μm was electrodeposited as described in our experimental section. The dense and smooth morphology of the film was confirmed by SEM analysis (Figure 2.8). The crystallinity and phase transition of the Sb-Te thin film from amorphous to nano-crystalline were investigated by XRD analysis. As shown in Figure 2.2(a), two different phases (*i.e.,* intermediate γ-SbTe and rhombohedral Sb_2Te_3) appeared in the temperature region of 70 to 100 ^{o}C (Figure 2.2a (C and D)). The calculated grain sizes of each phase based on Scherrer equation was about 20 nm independent of annealing temperature. As the annealing temperature further increased, the intermediate γ-SbTe disappeared and only rhombohedral Sb_2Te_3 remained (Figure 2.2a(E)). The formation of two phases during the crystallization might be attributed to the difference in the mixing enthalpy of various bonding structures during annealing.[19,21] The co-existence of two different phases was also confirmed by investigating the change of the chemical bonding states of the films.

The XPS analysis (Figure 2.2b) was performed on the Sb-Te film before and after an annealing at 70 and 200 ℃. It is known that the binding energies of Sb 3d peak are 529 ~ 530 eV (3d3/2) and 538 ~ 539 eV (3d5/2) ascribed to Sb-Te bonding.[22] The peak position of the Sb homopolar (Sb-Sb) bond is at 537.4 eV for Sb3d3/2 and 527.9 or 528.2 eV for Sb3d5/2. The XPS spectrum (b) in Fig. 2 shows additional binding energy at a Sb 3d peak at 537.9 and 528.6 from the sample annealed at 70 ℃, indicating that the Sb-Sb bond is present, which is observed in γ-SbTe. These peaks disappeared with the higher annealing temperature, which is readily corresponding to the XRD data.

In order to investigate the change of its electrical and thermoelectric properties during the phase transition, the properties were measured at room temperature after different annealing treatment. Figure 2.3 shows the electrical conductivity (black circle), carrier concentration (red triangle) and carrier mobility (blue square) as a function of annealing temperature. The electrical conductivity of the as-deposited amorphous Sb-Te thin film was of order ~ 10^{-2} S/cm. When the film was annealed at the temperature range from 50 to 80 ^{o}C, the electrical conductivity increased significantly by almost 3 orders. The conductivity further increased gradually with annealing temperature reaching 1.65 x 10^{2} S/cm at 200 ^{o}C. This number is about an order of magnitude lower than that of a bulk single crystal (*i.e.,* 5.59 x 10^{3} S/cm). Carrier concentration, which was determined from Hall measurement, followed a similar trend as the electrical conductivity. After annealed at 200 ^{o}C, the film's carrier concentration increased significantly from 1×10^{17} to 8×10^{19} cm^{-3}. Unlike the carrier concentration, the carrier mobility showed a maximum (*i.e.*,

214 $cm^2/V \cdot s$) at 70 ^oC followed by abrupt decreased by 100 ^oC, and gradual increased by 200 ^oC.

Up to 50 ^oC, the Sb_2Te_3 thin film maintained its amorphous phase (Figure 2.2a). According to Anderson-Mott model of electronic bands in disordered semiconductors, the disorder electronic states are made of extended states and localized states within the energy gap.[23-25] Due to the localized states, where the charge transport is induced by thermal activation between adjacent atoms, the carrier transport in the amorphous Sb-Te, which has a high density of localized states at the Fermi level,[11,23,26] can be explained by hopping transport. In this concept, the carrier transport in the localized states has no great coherence of unit cells, therefore, the carrier moves by hopping from one atom to the next where the conductivity and mobility of the carrier are essentially very small. Some of works reported the electrical conductivity of amorphous Sb-Te thin films of 0.2 ~ 0.5 S/cm at room temperature,[11,24] which is approximately one order magnitude higher than electrodeposited amorphous Sb-Te thin film (~ 10^{-2} S/cm). The difference in electrical conductivity might be due to the difference in the degree of disorder caused by the different synthesis methods used. Moreover, the relatively low values of carrier mobility in the Sb-Te thin film also manifested the transport behaviors in the amorphous phase. After the crystallization process, however, the charge transport by a hopping mechanism is no longer valid to interpret the electrical transport owing to the improved crystallinity.

In the Sb_2Te_3 thin film, the phase transition occurred at the transition temperature (T_p) of 60 ^oC, showing the formation of two different phases (*i.e.*, intermediate γ-SbTe

and rhombohedral Sb_2Te_3). This T_p is lower than the reported T_p (67 to 97 ^oC) of the Sb_2Te_3.[11,24] The difference in the transition temperature may be caused by the formation of different crystal structures. Unlike the reported works, where the amorphous phase was completely transformed to the single-phase rhombohedral Sb_2Te_3 for long duration of heat treatment, our Sb-Te thin film formed the γ-SbTe phase at 60 ^oC for 30 min before the complete transformation. The formation of the intermediate γ-SbTe phase is believed to be formed by diffusion limited kinetics for the formation of stable Sb_2Te_3, which is in the smallest mixing enthalpy.[19]

In the early state of crystallization in Sb-Te (*i.e.*, 60 to 70 ^oC), even though the phase transition was observed by the XRD analysis (Figure 2.2(a)), the low carrier concentration (~10^{17} cm^{-3}) was obtained in the measurement (Figure 2.3). The sharp increase in the mobility was observed in this region. Recently, Woellner *et al*. reported the simulation of the mobility behavior in a two-phase system with a low carrier concentration. In this simulation, the increased mobility was observed with reduced energetic disorder in both phases,[25] which is similar to the mobility increase in this work. Once the film was annealed at 80 ^oC, however, the mobility dropped abruptly whereas the carrier concentration increased by almost two orders of magnitude. This sudden increase of carrier concentration proves the formation of the γ-SbTe phase, which has much smaller band gap than Sb_2Te_3.[27] The significant increased carrier concentration made the charge-charge scattering dominant rather than the interface scattering in this system, resulting in the decrease of carrier mobility.[28] Based on the XRD analysis, the Sb-Te thin film was completely transformed to the single-phase

Sb_2Te_3 after annealed at 200 ^oC. The diverse studies on the transport characterization of crystalline Sb_2Te_3 were investigated in a wide range of the conductivity, listed in Table S1. The carrier concentration and mobility of the crystalline Sb_2Te_3 films were generally placed in the range of 10^{19} to 10^{20} cm^{-3} and 10 to 400 $cm^2/V.s$, respectively in which the values from the single-phase nanocrystalline Sb_2Te_3 were located (Figure 2.S2).

The Seebeck coefficient and power factor (P.F. = σS^2) of the Sb-Te thin film as a function of the annealing temperature are shown in Figure 2.4. The Seebeck coefficients were positive at all temperatures, indicating that the film is a p-type semiconductor. In the amorphous phase of the film, its Seebeck coefficient was between 167 to 204 μV/K, followed by an increase to optimum of 480 μV/K after annealed at 70 ^oC. Once the sample was further annealed at 80 to 100 ^oC, the Seebeck coefficient was reduced to 286 μV/K. A significant reduction in the Seebeck coefficient was observed after annealing above 150 ^oC. Like the Seebeck coefficient, the P.F. increased with the annealing temperature reaching a maximum at 80 ^oC but decreased thereafter. However, their maximum values were achieved at different temperatures; the highest Seebeck coefficient was obtained at 70 ^oC and the greatest P.F. was achieved at ten degrees higher. The mismatch in the optimal temperature is simply because of the higher electrical conductivity at 80 ^oC (56.7 S/cm), which compensates for the lower Seebeck coefficient (322 μV/K) compared to that at 70 ^oC (450 μV/K). The amorphous Sb-Te thin film show a greater Seebeck coefficient (167 - 204 μV/K) compared to the single crystalline Sb_2Te_3 bulk (38 - 83 μV/K). This is because of the large activation energy required by the localized states than free carriers at the Fermi level in the disordered materials.[11]

Similar results of larger Seebeck coefficients from the amorphous chalcogenide films than annealed films were investigated with relatively high thermal activation energies.[11,26,29,30] After the T_P (60 ^oC) to 100 ^oC where the two-phase system was observed, the enhancement of the Seebeck coefficient was clearly obtained. Compared to the Seebeck coefficient of single crystalline bulk Sb_2Te_3 (38 to 83 μV/K), these values were drastically enhanced. The Seebeck coefficient can be described as follows in a single band material:

$$S = \frac{\pi^2 {k_B}^2 T}{3e}\left(\frac{\partial lnN(E)}{\partial E} + \frac{\partial ln\tau(E)\upsilon(E)^2}{\partial E}\right)_{E_F} \quad \text{Equation 2.1}$$

$$\tau^{-1}(E) = \frac{{V_b}^2 x}{R}E^{-3/2} = \frac{e\mu}{m^*} \quad \text{Equation 2.2}$$

where N(E) is the density of the states, υ(E) is the average charge velocity, τ(E) is the carrier scattering relaxation time, and m^* is the effective mass of the carrier. As indicated in Equation 2.2 the carrier relaxation time is inversely proportional to the barrier potential (V_b). As described, incorporating an effective height in a potential barrier can enhance the Seebeck coefficient. Emphasizing the observation of the two-phase mixture (70 - 100 ^oC) in our film, it is believed that the carrier energy filtering effect may occur at the interfaces between the two phases, consequently, leading to the enhanced Seebeck coefficient and power factor. The significant reduction in the Seebeck coefficient after annealing at 150 ^oC appears to correspond to the disappearance of the potential barriers due to the complete transformation of intermediate γ-SbTe to Sb_2Te_3 phase in the film.

The summary of the transport and thermoelectric properties of our Sb_2Te_3 thin film and recently published literature data using the Sb_2Te_3 thin films is listed in Table 2.1. As the effort to enhance the P.F., many researchers have focused on increasing the

conductivity of the Sb_2Te_3 thin films without suppressing the Seebeck coefficient. By utilizing various synthesis methods such as electrodeposition (ED),[31] solution phase method (SM),[4,9] radio frequency magnetron sputtering (SP),[13] ion beam sputtering (IBS),[32] atomic layer deposition (ALD),[33] molecular beam epitaxy (MBE),[34] and traveling heater method (THM)[10] the enhanced thermoelectric properties were investigated in a wide range of the conductivity in past years. Moreover, additional processes such as the post-annealing and nano-particle inclusion were suggested to further enhance the thermopower. However, the Seebeck coefficient values remained within the 75 ~ 160 μV/K range. The Seebeck coefficient and the P.F. as a function of the electrical conductivity are plotted in Figure 2.10. As indicated, the P.F. values of literature data clearly represented the linear relationship as a function of the conductivity (10^1 ~ 10^4 S/cm) which is due to the similarity of the Seebeck coefficient values. Distinction of the Seebeck coefficient enhancement in our film was indicated after annealing at 70 to 100 ^oC. Because of the increased Seebeck coefficient, the relatively higher P.F. values were recorded in the conductivity range of 10 ~ 10^2 S/cm compared to the reported data.

In order to compare the effect of the two-phase nanocrystalline on thermopower, Pisarenko plot was applied with literature data as shown in Figure 2.5. Bulk Sb_2Te_3 (star) as well as Sb_2Te_3 thin films with the incorporation of Te (triangle), Pt (diamond), and Ag (square) were also shown in the figure. Clear enhancement of Seebeck coefficient was observed in the two-phase nanocrystalline film (solid circle) compared to not only the single-phase nanocrystalline (empty circle), but also the Sb_2Te_3 thin films with the Te, Pt,

and Ag. As mentioned, the Seebeck coefficient of the Sb_2Te_3 films can be enhanced by creating potential barriers at the interfaces between the Sb_2Te_3 and Pt, Ag, and Te. The Seebeck coefficient enhancement in our two-phase mixture film may be also caused by the EFE due to the formation of potential barriers at the interfaces between two phases. The calculated effective mass based on Mott-relation was also compared to evaluate the energy filtering effect from various types of interfaces. The dotted lines show the Mott-relation with various values of m^*/m_0. Among the reported results, the Ag-incorporated Sb_2Te_3 thin film represented the largest effective mass. In case of our two-phase nanocrystalline Sb_2Te_3 thin films, however, it has the similar effective mass values, but almost more than two times larger Seebeck values. This might be results of the incorporated material characteristics. Again, it is known that the metal incorporation in the semiconductor materials is irresistible to increase the carrier concentration. This is counter effect on Seebeck coefficient due to their interdependence. As observed in our experiment, intentionally separated two different phases in Sb_2Te_3 film successfully demonstrated enhanced Seebeck values without negative compensation.

The valence band (E_{VB}) difference between γ-SbTe and single-phase nanocrystalline Sb_2Te_3 film was measured by ultraviolet photoelectron spectroscopy (UPS). It is kwon that the top of the valence band mainly consists of Te states, whereas the character of the conduction band is mainly Sb states, resulting that the γ-SbTe phase has similar conduction band but different valance band from Sb_2Te_3 phase.[27] As shown in Figure 2.6, clear shift in binding energy depending on its crystal structures represents the valence band change. The difference in the valence band between γ -SbTe and Sb_2Te_3

nanocrystalline is about 90 meV, which is similar to the theoretical approximation of optimized barrier height.[1] Therefore, the band bending at the two-phase interfaces might be induced by the difference in the valence band, leading to the strong energy-dependent charge scattering to enhance the Seebeck coefficient and, therefore, P.F..

The change of m^*/m_0 of Sb_2Te_3 thin film as a function of the annealing temperature is plotted in Figure 2.7. The values of m^*/m_0 were obtained by fitting the results using the Mott-relation.[2] As noticed, the maximum effective mass was achieved in the two-phase nanocomposite film, showing a number that it is almost three times larger than the values from in the single-phase thin film. Moreover, these values correspond to the values of the bulk single crystal Sb_2Te_3 whereas lowered carrier concentrations led to higher Seebeck coefficients. Therefore, this work highlights that the mixture of two phases in the system can play an important role for superior thermoelectric properties. Moreover, the two-phase nanocrystalline Sb_2Te_3 thin film may also effectively scatter mid- to long-wavelength phonons that transport a large fraction of the heat, consequently bring an additional positive effect on the improvement of the thermopower efficiency.

2.5 Conclusion

In this paper, the nanoinclusion γ-SbTe in Sb_2Te_3 film was achieved by preparing the amorphous Sb-Te film using the simple and cost-effective electrodeposition technique followed by a post-annealing process. The formation of γ-SbTe in nanocrystalline Sb_2Te_3 matrix was confirmed by XRD and XPS analysis, representing its crystal structure and chemical bonding states. Enhancement of Seebeck coefficient and P.F. was observed in

this two-phase γ-SbTe/Sb_2Te_3 compared to not only the single-phase Sb_2Te_3 nanocrystalline film but also the reported values of Sb_2Te_3 films with the incorporation of Te, Pt, and Ag. The difference in the valence band of ~90 meV between γ-SbTe and Sb_2Te_3 nanocrystalline, confirmed by UPS analysis, supports the strong energy-dependent charge scattering as a result of the highly maintained Seebeck coefficient of 320 μV/K observed in two-phase γ-SbTe/Sb_2Te_3 nanocomposites.

2.6 References

[1] S.V. Faleev and L. François, *Theory of enhancement of thermoelectric properties of materials with nanoinclusions*, Physical Review B, 2008, **77**: p.214304.

[2] I.J. Yoo, Y. Song, L.D. Chan, N. V. Myung, K. H. Lee , M. Oh, D. Lee, Y. Kim, S. Kim, Y.H. Choa, J.Y. Lee, K.H. Lee, and J.H. Lim, *Thermoelectric characteristics of Sb2Te3 thin films formed via surfactant-assisted electrodeposition*, Journal of Materials Chemistry A, 2013, **1**: p.5430-5435.

[3] L.D. Hicks and M.S. Dresselhaus, *Effect of quantum-well structures on the thermoelectric figure of merit*, Physical Review B, 1993, **47**: p.12727-12731.

[4] D.K. Ko, Y. Kang, and C.B. Murray, *Enhanced Thermopower via Carrier Energy Filtering in Solution-Processable Pt–Sb2Te3 Nanocomposites*, Nano Letters, 2011, **11**: p.2841-2844.

[5] J.P. Heremans, V. Jovovic, E.S. Toberer, A. Saramat, K. Kurosaki, A. Charoenphakdee,S. Yamanaka, and G.J. Snyder, *Enhancement of Thermoelectric Efficiency in PbTe by Distortion of the Electronic Density of States*, Science, 2008, **321**: p.554-557.

[6] D. Narducci, E. Selezneva, G. Cerofolini, S. Frabboni, and G. Ottaviani, *Impact of energy filtering and carrier localization on the thermoelectric properties of granular semiconductors*, Journal of Solid State Chemistry, 2012, **193**: p.19-25.

[7] C.M. Jaworski, V. Kulbachinskii, and J.P. Heremans, *Resonant level formed by tin in Bi2Te3 and the enhancement of room-temperature thermoelectric power*, Physical Review B, 2009, **80**: p.233201.

[8] J.P. Heremans, B. Wiendlocha, and A.M. Chamoire, *Resonant levels in bulk thermoelectric semiconductors*, Energy & Environmental Science, 2012, **5**: p.5510-5530.

[9] Y. Zhang, M.L. Snedaker, C.S. Birkel, S. Mubeen, X. Ji, Y. Shi, D. Liu, X. Liu, M. Moskovits, and G.D. Stucky, *Silver-Based Intermetallic Heterostructures in*

Sb2Te3 Thick Films with Enhanced Thermoelectric Power Factors, Nano Letters, 2012, **12**: p.1075-1080.

[10] D.M. Rowe, CRC Handbook CRC Press (1995).

[11] D.V. Damodara, N. Soundararajan, and M. Pattabi, *Electrical conductivity and thermoelectric power of amorphous Sb2Te3 thin films and amorphous-crystalline transition*, Journal of Materials Science, 1987, **22**: p.3522-3528.

[12] N.G. Patel, and P.G. Patel, *Electrical properties of polycrystalline Sb2Te3 films*, Journal of Materials Science, 1991, **26**: p.2543-2546.

[13] B. Fang, Z. Zeng, X. Yan, and Z. Hu, *Effects of annealing on thermoelectric properties of Sb2Te3 thin films prepared by radio frequency magnetron sputtering*, Journal of Materials Science: Materials in Electronics, 2013, **24**: p.1105-1111.

[14] G. Leimkühler, I. Kerkamm, and R. Reineke-Koch, *Electrodeposition of Antimony Telluride*, Journal of The Electrochemical Society, 2002, **149**: p.474-478.

[15] Q. Huang, A.J. Kellock, and S. Raoux, *Electrodeposition of SbTe Phase-Change Alloys*, Journal of The Electrochemical Society, 2008, **155**: p.104-109.

[16] H. Jung and N.V. Myung, *Electrodeposition of antimony telluride thin films from acidic nitrate-tartrate baths*, Electrochimica Acta, 2011, **56**: p.5611-5615.

[17] H. Jung, J.H. Lim, H. Park, J. Kim, Y.H. Choa, and N.V. Myung, *Lithographically Patterned p-Type SbxTey Nanoribbons with Controlled Morphologies and Dimensions*, The Journal of Physical Chemistry C, 2013, **56**: p.17303-17308.

[18] D. Pinisetty, M. Gupta, A.B. Karki, D.P. Young, and R.V. Devireddy, *Fabrication and characterization of electrodeposited antimony telluride crystalline nanowires and nanotubes*, Journal of Materials Chemistry, 2011, **21**: p. 4098-4107.

[19] C. Guo, C. Li, and Z. Du, *Thermodynamic Re-modeling of the Sb-Te System Using Associate and Ionic Models*, Journal of Electronic Materials, 2014, **43**: p. 4082-4089.

[20] X.H. Yang, X.Y. Qin, J. Zhang, D. Li, H.X. Xin, and M. Liu, *Enhanced thermopower and energy filtering effect from synergetic scattering at heterojunction potentials in the thermoelectric composites with semiconducting nanoinclusions*, Journal of Electronic Materials, 2013, **558**: p. 203-211.

[21] G. Ghosh, *The Sb-Te (antimony-tellurium) system*, Journal of Phase Equilibria, 1994, **15**: p. 349-360.

[22] M.J. Shin, D.J. Choi, M.J. Kang, and S.Y. Choi, *Chemical Bonding Characteristics of Ge2Sb2Te5 for Thin Films*, Journal of the Korean Physical Society, 2004, **44**: p. 10-13.

[23] D.K. Ferry, S.M. Goodnick, J. Bird, Transport in nanostructures. Cambridge, (2009).

[24] J. Yu, B. Liu, T. Zhang, Z. Song, S. Feng, and B. Chen, *Effects of Ge doping on the properties of Sb2Te3 phase-change thin films*, Applied Surface Science, 2007, **14**: p. 6125-6129.

[25] C.F. Woellner, Z. Li, J.A. Freire, G. Lu, and T.Q. Nguyen, *Charge carrier mobility in a two-phase disordered organic system in the low-carrier concentration regime*, Physical Review B, 2013, **88**: p. 125311.

[26] S.A. Baily, and D. Emin, *Transport properties of amorphous antimony telluride*, Physical Review B, 2006, **73**: p. 165211.

[27] K. Govaerts, M. H. F. Sluiter, B. Partoens, and D. Lamoen, *Stability of Sb-Te layered structures: First-principles study*, Physical Review B, 2012, **85**: p. 144114.

[28] P. Zhu, Y. Imai, Y. Isoda, Y. Shinohara, X. Jia, G. Ren, and Guangtian Zou, *Electrical Transport and Thermoelectric Properties of PbTe Prepared by HPHT*, Materials Transactions, 2004, **85**: p. 3102-3105.

[29] H.K. Rockstad, R. Flasck, and S. Iwasa, *Seebeck coefficient in amorphous chalcogenide films*, Journal of Non-Crystalline Solids, 1972, **10**: p. 326-330.

[30] S. Raoux, D. Ielmini, M. Wuttig, and I. Karpov, *Phase change materials*, MRS Bulletin, 2012, **37**: p. 118-123.

[31] C. Schumacher, K.G. Reinsberg, L. Akinsinde, S. Zastrow, S. Heiderich, W. Toellner, G. Rampelberg, C. Detavernier, J.A.C. Broekaert, K. Nielsch, and J. Bachmann, *Optimization of Electrodeposited p-Doped Sb2Te3 Thermoelectric Films by Millisecond Potentiostatic Pulses*, Advanced Energy Materials, 2012, **2**: p. 345-352.

[32] Z.H. Zheng, P. Fan, J.T. Luo, G.X. Liang, and D.P. Zhang, *Enhanced Thermoelectric Properties of Antimony Telluride Thin Films with Preferred Orientation Prepared by Sputtering a Fan-Shaped Binary Composite Target*, Journal of Electronic Materials, 2013, **42**: p. 3421-3425.

[33] S. Zastrow, J. Gooth, T. Boehnert, S. Heiderich, W. Toellner, S. Heimann, S. Schulz, and K Nielsch, *Thermoelectric transport and Hall measurements of low defect Sb2Te3 thin films grown by atomic layer deposition*, Semiconductor Science and Technology, 2013, **28**: p. 035010.

[34] N. Peranio, M. Winkler, Z. Aabdin, J. König, H. Böttner, and O. Eibl, *Room temperature MBE deposition of Bi2Te3 and Sb2Te3 thin films with low charge carrier densities*, physica status solidi (a), 2012, **209**: p. 289-293.

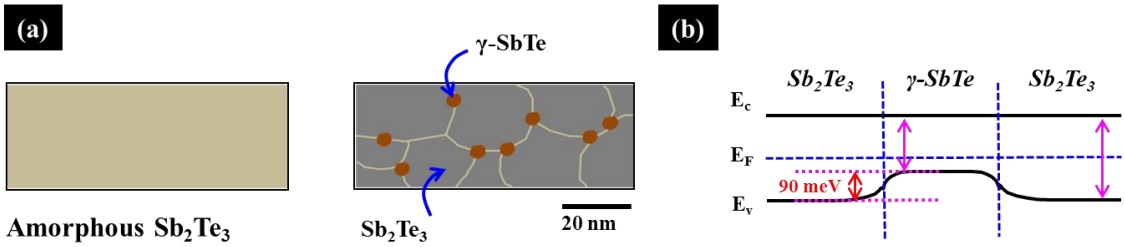

Figure 2.1 Schematic of the anticipated solid-state phase transition from amorphous Sb-Te driven by external thermal energy in accordance with the composition-dependent crystallization kinetics of a binary Sb-Te system (a). An intermediate γ-SbTe nanoinclusion in nanocrystalline Sb_2Te_3 matrix can possibly create a potential barrier (V_b) for band bending shown in hetero-junction band diagram (b).

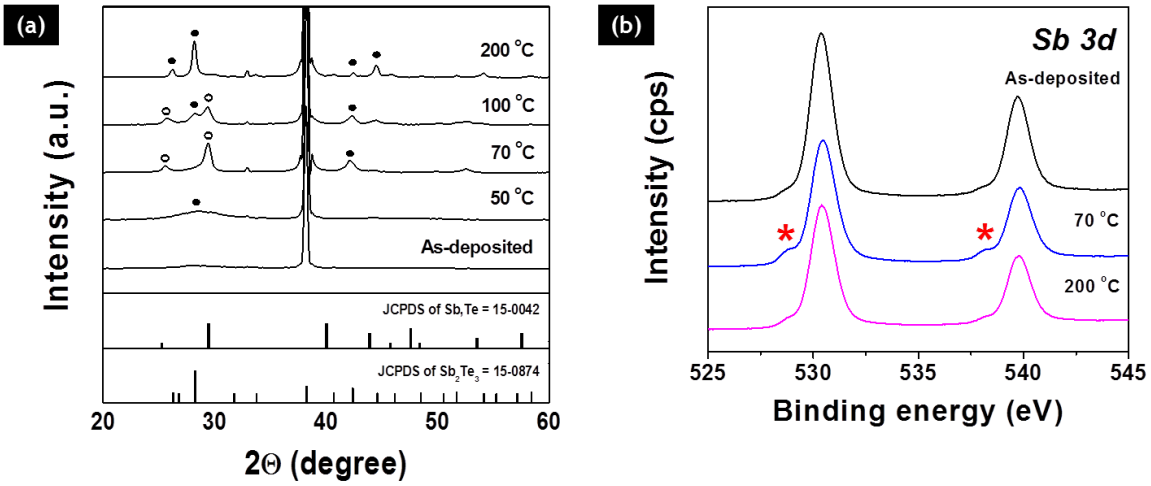

Figure 2.2 XRD analysis (a) of as-deposited and annealed at 50, 70, 100, and 200 ^{o}C for 30 min $Sb_{37}Te_{63}$ thin film. Symbol of solid circle refers to Sb_2Te_3 JCPDS 15-0874, symbol of empty circle refers to γ-SbTe JCPDS 15-0042. XPS analysis (b) of as-deposited and annealed at 70 and 200 ^{o}C.

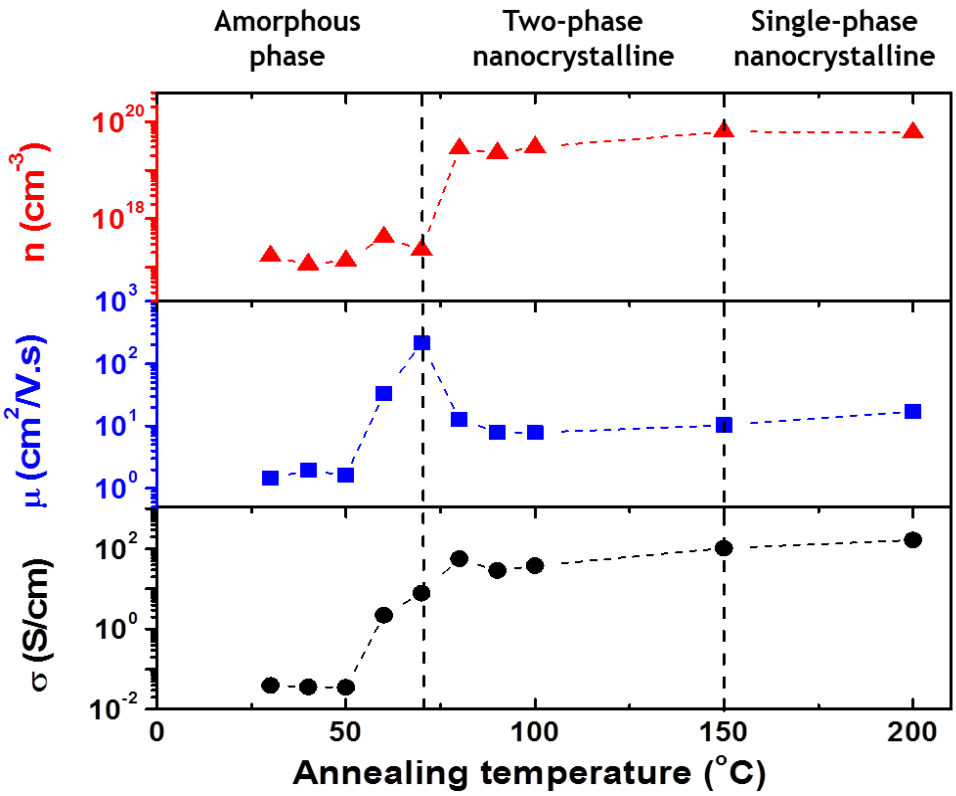

Figure 2.3 Change of electrical conductivity (black circle), Hall mobility (blue triangle), and carrier concentration (red square) of Sb_2Te_3 thin film as a function of annealing temperature.

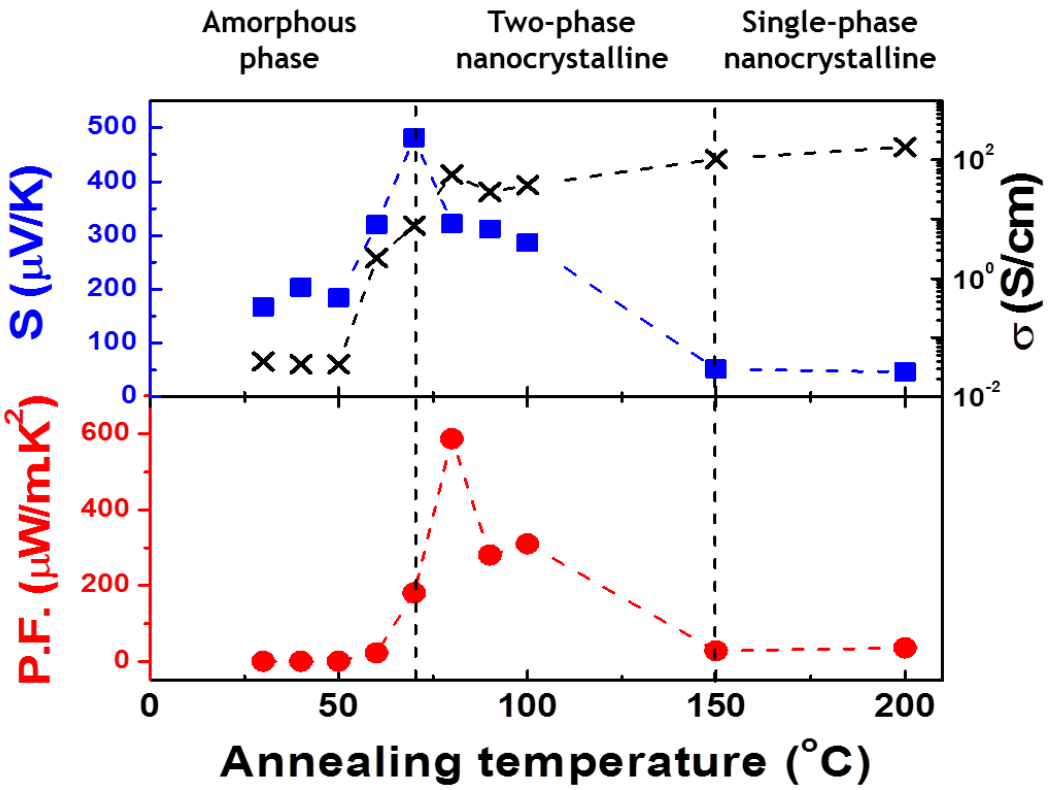

Figure 2.4 Change of thermoelectric properties of Sb_2Te_3 thin film as a function of annealing temperature.

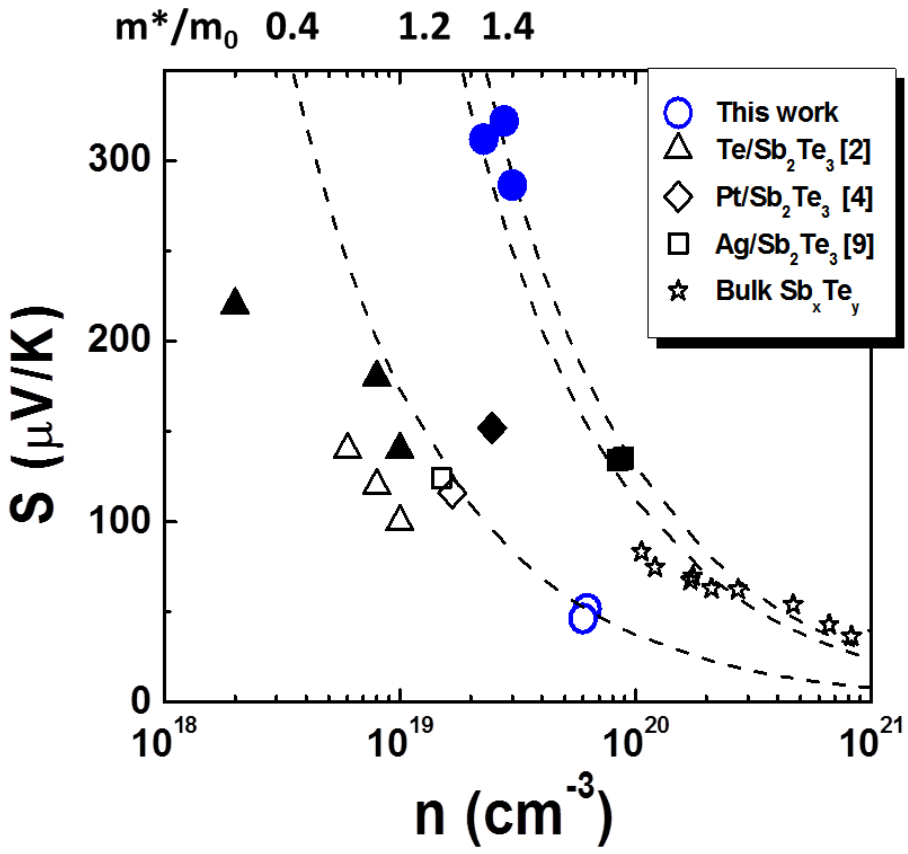

Figure 2.5 Seebeck coefficient as a function of carrier concentration (Pisarenko plot) at room temperature. The compared results are from studies of Sb_2Te_3 thin films (empty) with the incorporation (solid) of Te (triangle), Pt (diamond), and Ag (square). Dashed lines are the theoretical fittings by Mott-relation.

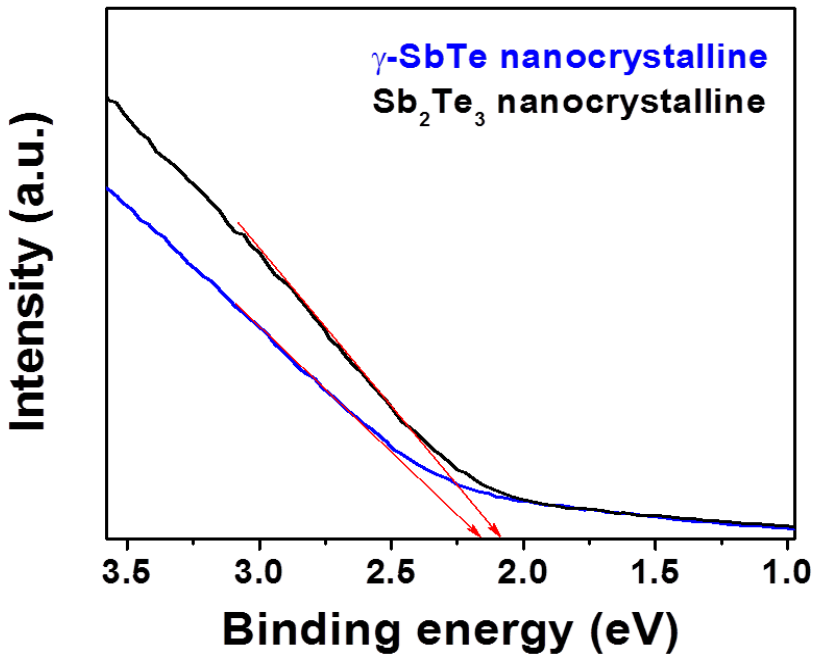

Figure 2.6 Measurements of valence band (E_{VB}) of γ-SbTe (blue) and Sb_2Te_3 nanocrystalline (black) by UPS analysis. An inset represents the derivative of the UPS spectra. Difference of E_{VB} between γ-SbTe and Sb_2Te_3 nanocrystalline is about 90 meV.

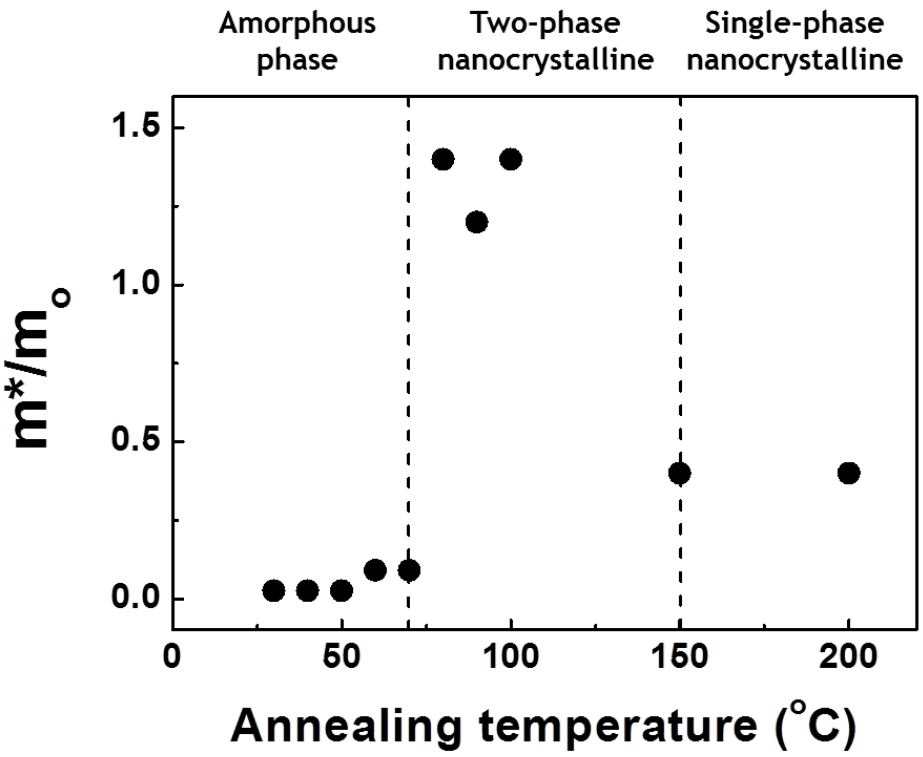

Figure 2.7 Change of m^*/m_0 of $Sb_{37}Te_{63}$ thin film as a function of the annealing temperature.

Table 2.S.1. Summary of electrical and thermoelectrical properties of Sb_2Te_3 thin films

Synthetic method	Morphology	Composition	Annealing	σ	S	P.F.	n	μ	Year/Ref.
			(^oC)	(S/cm)	(μV/K)	(μW/m.K^2)	(cm^{-3})	(cm^2/V.sec)	
ED	Thin film	Sb_2Te_3	-	0.0395	167	0.1103	1.69E+17	1.46	this work
			40	0.0359	204	0.1493	1.15E+17	1.94	
			50	0.0356	184	0.1201	1.36E+17	1.64	
			60	2.2	320	23	4.16E+17	33	
			70	7.8	482	181	2.27E+17	214	
			80	57	322	587	2.77E+19	13	
			90	29	312	280	2.27E+19	7.93	
			100	38	286	310	3.01E+19	7.84	
			150	104	52	28	6.24E+19	10	
			200	165	46	36	5.98E+19	17	
IBS		Sb_2Te_3	-	750	145	1700	-	-	2013 [31]
				2800	100	2700			
				3500	110	4400			
				2200	160	6100			
				4000	130	3000			
SP		$Sb_{34}Te_{66}$	-	100	150	225	1.30E+20	10	2013 [13]
			100	300	120	432	1.20E+20	18	
			150	800	115	1058	1.05E+20	45	
			200	1000	120	1440	9.00E+19	70	
			250	1200	125	1875	8.00E+19	95	
ALD		Sb_2Te_3	-	104	146	222	2.40E+18	271	2013 [32]
MBE		$Sb_{39}Te_{61}$	-	1696	130	2866	2.60E+19	402	2012 [33]
ED		Sb_2Te_3	-	71	75	40	-	-	2012 [30]
			327	171	119	242			
SM		$Ag_{20}Sb_{27}Te_{53}$	50	11	134	20	8.40E+19	0.6	2012 [9]
		$Ag_{31}Sb_{19}Te_{50}$	150	56	135	102	8.90E+19	4.1	
		Sb2Te3	150	39	124	60	1.50E+19	14	
SM		Sb2Te3	-	73	116	96	1.67E+19	28	2011 [4]
		Pt-Sb2Te3		27	152	102	2.46E+19	11	
THM	Bulk	Sb36.5Te63.5	-	5587	75	3126	1.21E+20	288	1995 [10]

1) ED : Electrodeposition, 2) SM : Solution phase method, 3) SP : Radio frequency magnetron sputtering , 4) IBS : Ion beam sputtering, 5) ALD : Atomic layer deposition, 6) MBE : Molecular beam epitaxy, 7) THM : Traveling heater method

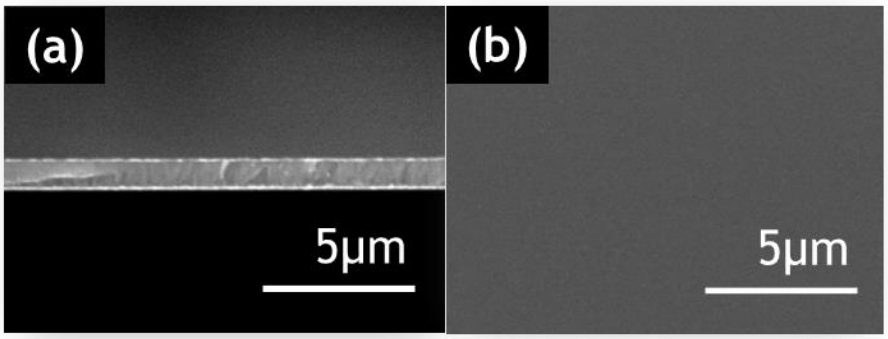

Figure 2.8 Morphology of $Sb_{37}Te_{63}$ thin film confirmed by cross-sectional (a) and top view (b) SEM images

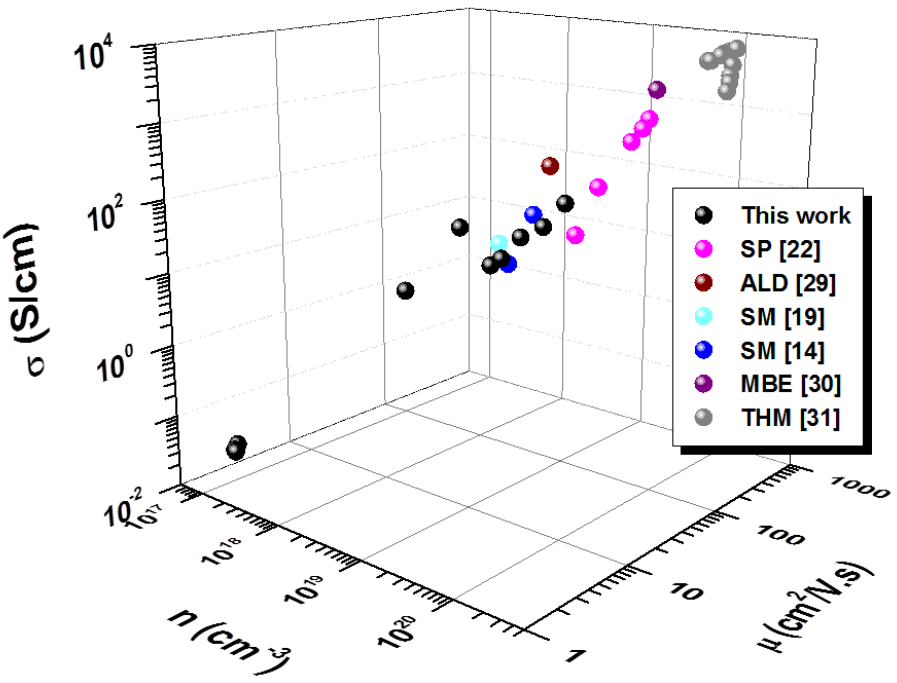

Figure 2.9 3D plot of electrical conductivity of Sb_2Te_3 thin film as a function of mobility and carrier concentration. Recently reported data from Sb_2Te_3 thin films and bulks are included for direct comparison.

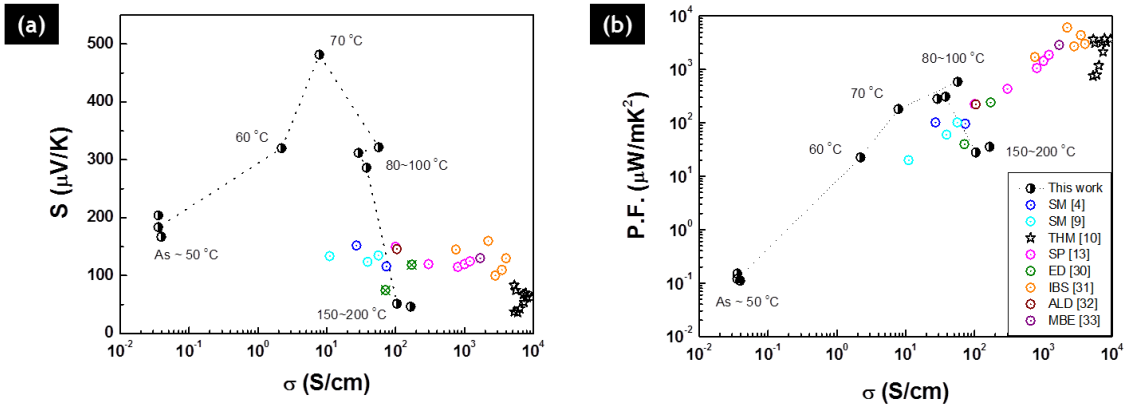

Figure 2.10 Seebeck coefficient (a) and power factor (b) of Sb_2Te_3 thin film as a function of electrical conductivity. Recently reported data from Sb_2Te_3 thin films and bulk are included for direct comparison.

CHAPTER 3 Facile Control over Interfacial Energy-Barrier Scatterings in Nanocrystalline Sb2Te3 Electrodeposits

3.1 Abstract

The goal of this work is to augment the thermoelectric performance of nanocrystalline Sb_2Te_3 thin films by controlling energy filtering effects (i.e., barrier heights) occurring at both grain boundaries and at an induced embedded second-phase within a grain. It‘s postulated that energy-dependent filtering lowers the current charge carrier concentration by removing the low energy carriers from the current after scattering, thus favoring a high Seebeck coefficient. A facile but high precision composition-controlled electrodeposition technique is selected to synthesize various compositions of amorphous Sb-Te solid solutions which are readily crystallized by post annealing treatments selectively forming thermodynamically favored phases, including single-phase nanocrystalline Sb_2Te_3 and crystalline nanocomposites Te/Sb_2Te_3 or γ-$SbTe/Sb_2Te_3$. Solution composition and post-annealing profiles are used to control the single-phase grain size, thereby the grain-boundary potential-barrier, at a given carrier concentration as well as the nature of the embedded second-phase. Electrical and thermoelectrical properties are measured and correlated with the properties of each film, where an enhanced Seebeck coefficient at a given carrier concentration is interpreted to imply that an energy-dependent carrier filtering effect is at play. On a promising note, the highest power factor investigated in the embedded γ-SbTe nanocomposite is observed at a lower

carrier concentration of ~$3x10^{19}$ versus ~$8x10^{19}$ for a single crystal - making it a candidate as a high zT thermoelectric based on an easily tailored energy filtering effect.

3.2 Introduction

The thermoelectric energy conversion efficiency of thermoelectric (TE) materials has been steadily improving over the last decades. The efficiency is expressed in terms of a dimensionless number $zT = S^2\sigma T/k$ simply referred to as the figure-of-merit, where S is the Seebeck coefficient, σ is the electrical conductivity, k is the thermal conductivity, and T is absolute temperature. Typical zT numbers range between1 to 2. Limited success at increasing zT has been achieved by focusing on reducing k. This is thought of in terms of increasing phonon scattering within the TE film by incorporating complex lattice structures, such as superlattices, heterostructures, and nanocomposites.[1-4] For some materials, k can be taken to a minimum by placing the material in an amorphous state, but this is typically associated with a substantial drop in the charge carrier mobility, thereby in electrical conductivity. This strong interdependence in the key parameters of zT has taken its toll by stalling the release of new high zT thermoelectric devices to industry. Therefore, another approach, adopted in this study, places focus on understanding and controlling mechanisms and processes that tend to de-couple key parameters and maximize the zT numerator, specifically, that optimize the power factor (P.F. = $S^2\sigma$).

Recently, it is known that interfacial energy barrier scattering of charge carriers is an effective method to enhance the power factor (P.F. = $S^2\sigma$). It is often called the energy filtering effect where the creation of band bending induced by charge transfer at the

interfaces can cause the energy-dependent scattering of charge carriers. In the concrete, the created interfaces on charge carrier pathways can generate a barrier height (potential, V_b) at which the low energy charge carriers are scattered but the high energy charge carriers pass through. This strong energy-dependent charge scattering leads to increase in the Seebeck coefficient because of its dependence on the energy derivative of the relaxation time at the Fermi energy;

$$S = \frac{\pi^2 {k_B}^2 T}{3e}\left(\frac{\partial lnN(E)}{\partial E} + \frac{\partial ln\tau(E)\upsilon(E)^2}{\partial E}\right)_{E_F} \quad \text{Equation 3.1}$$

$$\tau^{-1}(E) = \frac{{V_b}^2 x}{R} E^{-3/2} = \frac{e\mu}{m^*} \quad \text{Equation 3.2}$$

where N(E) is the density of the states, υ(E) is the average charge velocity, τ(E) is the carrier scattering relaxation time, and m* is the effective mass of the carrier. In addition, as indicated in Equation 3.2 the carrier relaxation time is inversely proportional to the barrier potential (V_b), therefore, adjusting the effective height in a potential barrier can be another variable to maximize the Seebeck coefficient.

Various theoretical and experimental results have probed the significant enhancement of the zT by utilizing the energy filtering effect in thermoelectric materials. As proposed by Faleev *et al.* where the concept of band bending at metal/semiconductor interfaces demonstrated the enhancement of the Seebeck coefficient as a result of strong energy dependent electron scattering, the incorporation of metal nanoparticles was selected as experimental approaches.[5] For example, Ko *et al.* and Zhang *et al.* introduced the metal Pt and Ag nanoparticles in the Sb_2Te_3 films, respectively, and represented the enhancement of Seebeck coefficient without losing the conductivity of

the Sb_2Te_3.[6,7] According to Sumithra *et al.*, the incorporation of semimetal Bi nanoparticles in nanostructured Bi_2Te_3 also revealed the enhanced Seebeck coefficient at given carrier concentrations and the reduced lattice thermal conductivity, thus, the increase in the bulk Bi_2Te_3 zT by a factor of 2(from 0.2 to 0.4).[8] Moreover, it was claimed that this strong energy-dependent charge scattering mechanism is not only valid at the interfaces created between metal or semimetal and semiconductors.[9] Martin *et al.* demonstrated the enhanced Seebeck coefficient in nanocrystalline PbTe bulk system using the effective grain-boundary potential-barrier scattering.[10] According to them, the low energy charge carriers are impeded at the grain boundaries of nanocrystals where the energy barriers are formed to trap the charge carriers. Similar behavior was also observed in the thermoelectric performance study using the Sb_2Te_3 nanoparticles by Chen *et al.*.[11] As the size of nanoparticle decreased the Seebeck coefficient of the films increased at given carrier concentration which was also understood as a result of the energy filtering effect due to the charge carrier trapped in the grain boundaries.

As indicated in the current researches, the development of nanostructure fabrication technology allowed demonstrating the intriguing thermoelectric performances in accordance with the interfacial energy barrier scatterings. Due to the strong interface dependent carrier transport of the nanostructured thermoelectric materials, however, it is essential to have a comparative analysis on the correlation of the improved thermoelectric performances with the physical properties of nanostructures to acknowledge the optimized conditions. Specially, the Sb_2Te_3 is a well-known p-type thermoelectric material operable at room temperature. Due to the high anti-site defects originated from

the similar electronegativity of Sb and Te atoms, however, the relatively low Seebeck coefficient (*i.e.,* 38~83 μV/K) at room temperature impeded its direct use for commercial thermoelectric applications. Although there are some limited works conducted on the nanostructured Sb_2Te_3 with the concept of the energy filtering effect, very limited of works directly evaluates the optimized thermoelectric performance in consequence of the change in the interfaces at given carrier concentration. Depending on the physical properties of the Sb_2Te_3, the position of its Fermi level is changed and so the effective barrier height will be also differed. This is the reason of a variation of the energy filtering effect on enhanced power factor values in the Sb_2Te_3. Therefore, it is important to develop the synthesis technique which can readily provide the nanocrystalline Sb_2Te_3 with incorporation of various second phases available.

The goal of this work was to optimize the thermoelectric performance of nanocrystalline Sb_2Te_3 thin films by tailoring the barrier heights of energy filtering mechanisms at play at both grain boundaries and at an induced embedded second-phase interface within a Sb_2Te_3 grain. A facile and rapid electrodeposition technique was selected to synthesize the various amorphous Sb-Te solid solutions by simply controlling the applied potential and electrolyte concentration. The amorphous films were crystallized by post annealing treatments selectively forming thermodynamically favored phases, including single-phase crystalline Sb_2Te_3 and crystalline nanocomposites Te/Sb_2Te_3 or γ-$SbTe/Sb_2Te_3$. We first manuplate the size of the single phase nanograin to monitor the grain boundary effect as a scattering source, followed by the incorporation of the two different second-phases. Electrical and thermoelectrical properties were measured

at room temperature for each film and correlated with their annealing temperature and physical properties. A significant enhancement in the power factor was observed in both the Te and γ-$SbTe/Sb_2Te_3$ nanocomposites compared to the single-phase nanocrystalline Sb_2Te_3 thin films. An accurate comparison to evaluate the energy filtering effect in each case was obtained by plotting the Seebeck coefficient vs. carrier concentration, where an enhanced Seebeck coefficient at a given carrier concentration would imply that an energy-dependent carrier filtering effect is at play. Furthermore, the larger effective mass values obtained by the Mott-relation in this plot are consistent with the electron filtering effect in the system. The highest power factor investigated in the γ-$SbTe/Sb_2Te_3$ nanocomposite was observed at a carrier concentration lower than that of the single phase host – making it a promising candidate for high *zT* thermoelectric applications.

3.3 Experimental Section

3.3.1 Synthesis and Material Characterization

Sb_xTe_{1-x} thin films were potentiostatically electrodeposited with a control of the concentration of electrolytes and applied potentials. According to our previous works on the electrodeposition of binary Sb_xTe_y thin films,[13] the morphology, crystallinity, and chemical composition of the thin films were highly dependent on the electrolyte concentration and applied potentials. Based on these previous knowledge, a $HTeO^{3+}$: Sb^{3+} molar ratio was varied to 3:1 and 2:3 in 1 M nitric acid solution. The issue of low solubility of Sb_2O_3 in acidic aqueous media,[27] was solved by using L-tartaric acid chosen as a complexing agent to form $[Sb(C_4H_2O_6)_2]^{-2}$ in the solution. The electrolyte

bath used for electrodeposition of Te-rich Sb_xTe_{1-x} thin films with smooth morphology was prepared by separately dissolving a 3.6 mM TeO_2 in a 1 M HNO_3 solution and a 1.2 mM Sb_2O_3 in a 33 mM L-tartaric acid solution at 60 ^oC. The dissolved solutions were then mixed together with deionized water to reach final volume of 1 L. The close stoichiometric and Sb-rich Sb_xTe_{1-x} thin films deposition was performed from an electrolyte containing 2.4 mM TeO_2, 3.6 mM Sb_2O_3, 33 mM L-tartaric acid, and 1 M HNO_3.

Electrodeposition of the films was performed using a Bio-Logic VSP potentiostat with DC method at a potential range of -0.1 to 0.14 V (vs. SCE). For a deposition substrate, Au coated Si substrate was utilized as a working electrode. The Au layers were deposited by e-beam evaporation technique and Ni with a thickness of 20 nm was used as an adhesion layer prior to Au deposition. A Pt coated titanium electrode and a saturated calomel electrode (SCE) were used as the counter and reference electrodes, respectively. A thickness of the films was controlled by a total charge of the deposition, which was fixed to 1.4 mAh per working electrode area of 3.14 cm^2. The deposition area was of circular with radius of 1 cm. All deposition were performed at 25 ^oC and magnetically stirred at 300 rpm. After the deposition, the films were rinsed using deionized water and dried in air using a blower.

Morphology and composition of the electrodeposited Sb_xTe_{1-x} thin films were analyzed by scanning electron microscopy (SEM) (Jeol, JSM-5800) and energy dispersive X-ray spectroscopy (EDS). Crystallinity and crystal structure of the films were investigated by X-ray diffraction (XRD) (Bruker D8 ADVANCE). Values of the full

width at half-maximum (FWHM) of each peaks informed by the XRD analysis were applied to provide a detail crystallographic property of the films using the Scherrer equation.[26] An annealing process with sequentially varied annealing temperatures ranging from 30 to 200 ^{o}C for 30 min in an argon atmosphere with 5 % hydrogen was added to introduce different types of nanoinclusion on the basis of the Sb-Te phase diagram. Furthermore, the effect of improvement of crystallinity on electrical and thermoelectric properties change was also able to be correlated for the aim of this work; optimization of thermoelectric performance using binary Sb-Te system. All films were annealed by using a tube furnace in a nitrogen atmosphere with 5 % hydrogen present.

For electrical and thermoelectric characterization, the films are required to be on non-conductive substrate. Therefore, the films were transferred from the Au/Ni/Si substrate to a non-conductive Torr Seal epoxy attached on acrylic substrate (Varian Vacuum Products, Lexington, Massachusetts) as shown in Figure 3.S2. The entire film was successfully transferred without cracking. The final dimension of the sample for characterization was 1 cm in width and ~0.3 cm in height of epoxy attached acrylic substrate and ~1 μm of binary Sb_xTe_{1-x} thin films.

3.3.2 Electrical and Thermoelectric Characterization

The electrical conductivity, Hall mobility, and carrier concentration of the film were investigated by a custom-made Hall measurement unit in the van der Pauw configuration with four-point probes. The Seebeck coefficient was determined by a custom-made

Seebeck measurement system by plotting the measured Seebeck voltages as a function of temperature difference (<2 ^{o}C) across the sample ($S = \Delta V/\Delta T$).

3.4 Results

3.4.1 Amorphous Sb-Te Electrodeposits

In order to synthesize composition-varied Sb_xTe_{1-x} thin films with smooth and dense morphology, the electrolyte concentration and applied potentials were controlled. The ability to deposit uniform morphology of the films is an important matter to successfully utilize them for thermoelectric applications. The morphology of the electrodeposits is determined by a material's growth type either a fast nucleation or growth dominant reaction.[12] The fast nucleation-dominant growth reaction can avoid needle-like or nodular/granular structure formation and achieve more smooth and dense morphology of the films. On the other hand, not only of the morphology but the applied potential is also a variable of the chemical composition of the films. Additionally, due to the relatively low Gibbs formation energy of Sb_2Te_3 (-58.35 kJ mol^{-1}), the composition of Sb_xTe_{1-x} electrodeposits shows the strong applied potential dependency during the electrodeposition. In the light of these considerations, the potentials ranging of -0.1 to -0.14 (V vs. SCE) were found for compatible morphology of the film deposition. Meanwhile, variation of the electrolyte concentration was chosen to tailor the composition within the small potential changes (ΔV_{max} = 40 mV).

Using the electrodeposition conditions described in the experimental section, the Sb_xTe_{1-x} films with 1~2 μm thickness were potentiostatically deposited. The Sb content

was tailored ranging from 30 to 42 at. % confirmed by EDS analysis. The cross sectional images of the films showed the dense and smooth morphology independently on the composition (Figure 3.5). Slight difference on texture of $Sb_{30}Te_{70}$ thin film was observed in the surface SEM image where the visible and anisotropic grown grains were appeared which was unlike the $Sb_{33}Te_{67}$, $Sb_{37}Te_{63}$, and $Sb_{42}Te_{58}$ thin film.

Crystallinity and crystal structure of the electrodeposited Sb_xTe_{1-x} films were confirmed by the XRD analysis as shown in Figure 3.1. The XRD results obtained from the as-deposited the $Sb_{33}Te_{67}$, $Sb_{37}Te_{63}$, and $Sb_{42}Te_{58}$ thin film indicated that electrodeposited binary Sb-Te alloy tends to initially form an amorphous phase, which is consistent with our previous electroanalytical studies on deposition of near-stoichiometric Sb_xTe_{1-x}[13] and others.[14,15] However, as the Te content of the film increased up to 70 at. %, the Te atoms preferred to form the single-phase crystalline Te instead of having the homogeneous amorphous Sb-Te compound. In addition, the XRD result of the $Sb_{30}Te_{70}$ also indicated a reflection peak of R-3m Sb_2Te_3 phase (JCPDS card 15-0874) corresponding to (1 0 10) direction.

3.4.2 Solid-State Phase Transition

Synthesis of the amorphous Sb-Te electrodeposits with varied chemical composition provides a valuable chance to systematically control the crystallographic properties. In fact, the Sb_2Te_3 and its ternary or quaternary alloys containing Ge, Ag, and In are also well-known candidates for non-volatile phase change memory (PCM) applications because of their large difference on resistivity between amorphous-crystalline phases and

the high reliability and reproducibility of each phase depending on the atom-positional switching.[16-21] Therefore, by tuning the crystallinity, not only the resistivity, but also the concentration and mobility of the charge carriers can be effectively modulated. Moreover, the crystal structure is also an important factor for the charge and entropy transport in the Sb_xTe_{1-x} system as a result of energy filtering effect. According to the Sb-Te phase diagram studied by Ghosh, there are two intermediate phases, δ and γ, and stable compound of Sb_2Te_3 available in the Sb-Te system.[22] The δ and γ phase with large homogeneity were indicated in the ranges of 63.2 ~ 83.6 and 51.0 ~ 58.9 at. % Sb, respectively. These two intermediate phases were also investigated by others[23-25] which is strictly determined by the chemical composition and temperature of the system. Moreover, the Te precipitation in the Sb_2Te_3 is also investigated as the Te content increased up to 62 ~ 100 at. %. Therefore, the preparation of Sb_2Te_3 thin film with an embedded additional phase can be favorable by controlling the initial composition of Sb-Te solid solution followed by a solid-state phase transformation under proper annealing conditions. So the effective interfacial energy barrier scatterings can be anticipated at the junction barriers between Sb_2Te_3 and available second phases. Additionally, control of the grain size is also a determining parameter for the improvements in thermoelectric performances by means of grain boundary scatterings to reduce the thermal conductivity and adjusting the carrier concentration to optimize charge transport. The amorphous Sb-Te solid solutions provide the absolute system for a systematical study on the effect of the grain size in the Sb_2Te_3 films. Therefore, it is important to study the effect of the post-

annealing on composition-dependent crystallinity and crystal structure of the Sb_xTe_{1-x} thin films.

The change of crystallinity and crystal structure of the Sb_xTe_{1-x} thin films as a function of annealing temperature (as ~ 200 ^oC) were investigated by XRD analysis (Figure 1). The FWHM of each peak were applied for average grain size calculation using Scherrer equation[26] shown in Table S1. The detail annealing conditions are indicated in the experimental section. The phase transition behavior of the Sb_xTe_{1-x} thin films from amorphous to nanocrystalline with various phases was observed and confirmed by matching with the reference patterns for Sb_2Te_3 (JCPDS 15-0874), γ-SbTe (JCPDS 15-0042), and Te (JCPDS 36-1452) and (JCPDS 44-0925). As expected from the phase diagram, the formation of crystal structures was strictly dependent on the chemical composition and annealing temperature. Recently, we reported the formation of intermediate γ-SbTe phase during the crystallization of the amorphous $Sb_{37}Te_{63}$ to the rhombohedral (*R-3m*) nanocrystalline Sb_2Te_3 film (Figure 3.1c). Instead of direct transition to the R-3m Sb_2Te_3, the γ-SbTe phase was formed in the temperature region of 70 to 100 ^oC along with the *R-3m* Sb_2Te_3 phase. As the annealing temperature further increased to 200 ^oC, the intermediate γ-SbTe disappeared and only nanocrystalline *R-3m* Sb_2Te_3 remained. The formation of the γ-SbTe phase was also observed during the crystallization of the $Sb_{42}Te_{58}$ film (Figure 3.1d). However, the annealing temperature at which the γ-SbTe phase formed increased to 100 ^oC, and the portion of the γ-SbTe phase remained was relatively higher than that of the $Sb_{37}Te_{63}$ film at the same temperature. This explains that the increase of Sb content in the film can hold the γ-SbTe phase more

stable in higher temperature. At 200 ^{o}C, however, the intermediate phase was also disappeared and completely transformed to the R-3m Sb_2Te_3 phase. Interestingly, the γ-SbTe phase was not observed during the crystallization of the Te-rich $Sb_{33}Te_{67}$ film (Figure 3.1b). Instead of showing the γ-SbTe phase at 70 ^{o}C, small tip of the peak corresponding to reflection peak of the *R-3m* (0 1 5) was observed followed by completely transformed to *R-3m* Sb_2Te_3 phase at 100 ^{o}C. Compared to the $Sb_{37}Te_{63}$ and $Sb_{42}Te_{58}$, the formation of a single phase R-3m Sb_2Te_3 was obtained at the lower temperature. However, as the annealing temperature further increased to 200 ^{o}C, the elemental Te was precipitated as a second phase, indicated as (1 0 0) and (1 1 0) reflections peaks in the XRD patterns. This result is consistent with the phase diagram of Sb-Te system where the mixture of Sb_2Te_3 and Te phase is indicated in the range of 62 ~ 100 at. % Te.[22] The calculated grain size of the Te phase is of ~ 24 nm. The phase transition from amorphous to nanocrystalline was also observed in the $Sb_{30}Te_{70}$ thin film. Although this film already had a crystalline Te and Sb_2Te_3 phase in the as-deposited state, the (0 1 5), (0 0 9), (1 1 0), and (2 0 5) Sb_2Te_3 peaks were appeared at 100 ^{o}C and increased their grain size by further annealing at 200 ^{o}C.

3.4.3 Electrical and Thermoelectric Characterization

The electrical conductivity (σ), Hall mobility (μ), and carrier concentration (n) of all the synthesized Sb_xTe_{1-x} films are shown in Figure 3.2 as a function of annealing temperature. All measurement was conducted at room temperature using four-point probe measurement and an annealing period for each step was 30 min in 5 % H_2 / 95 % Ar,

which is readily identical with the conditions used for the annealing temperature dependent XRD analysis (Figure 3.1). Therefore, direct correlation between the crystallinity, crystal structures, and crystallographic changes of the Sb_xTe_{1-x} and electrical transport properties is anticipated. As noticed, the conductivities of the $Sb_{33}Te_{67}$, $Sb_{37}Te_{63}$, and $Sb_{42}Te_{58}$ measured in the early annealing steps were of 0.1 ~ 7, 3.5 ~ 4, and 0.9 ~ 1.5 (10^{-2} S/cm), respectively. The relatively low conductivity values are consistent with their amorphous phases remained within the annealing periods. In addition, the Sb/Te ratio in the amorphous Sb_xTe_{1-x} films also results in variation of transport properties. As the Sb content increased in the Sb_xTe_{1-x} films, the electrical conductivity decreased. This behavior can be understood as a response of the increased carrier concentration as the Sb content increased whereas the mobility values reversely reduced. This trend is expected because the significant antisite defects from non-stoichiometry raises the carrier concentration of the films. Therefore, we conclude that the transport properties of the amorphous Sb_xTe_{1-x} thin film are strictly determined by their chemical composition. Once the films were further annealed the improved crystallinity represented the orders of magnitude increased conductivities. The transition temperature (T_p), at which the film's conductivity dramatically changes, was differed as a function of composition. The T_p of the $Sb_{37}Te_{63}$ film was indicated as 60 ^oC which was 10 ^oC lower than that of $Sb_{33}Te_{67}$ and $Sb_{42}Te_{58}$ film. After the T_p, the conductivity of all films drastically increased by 100 ^oC, and slowed down to change but continuously enhanced by 200 ^oC. The significant increase in the conductivities of the films was most likely due to the increase in carrier concentration as the crystallization was progressed. Unlike the

mobility values fluctuated in the disordered crystal structure states, they remained more stable after crystallization and independent on the annealing temperature. In contrast with the transport properties of the three films started with the amorphous phase, the $Sb_{30}Te_{70}$ film showed a distinguished trend in the transport properties as a function of annealing temperature. As confirmed in the annealing temperature-dependent XRD analysis, this film formed the crystalline Te phase in as-deposited state, followed by formation of the R-3m Sb_2Te_3 phase at 100 ^oC. From the conductivity measurement from the as-deposit to 100 ^oC, the change of the conductivity was a four-fold, which was significantly less than that of others. After 100 ^oC, the conductivity continuously increased showing a similar trend with other films.

The Seebeck coefficient (S) and Power factor (P.F. = $\sigma^2 S$) of the Sb_xTe_{1-x} thin films as a function of annealing temperature are plotted in Figure 3.3. The Seebeck coefficients of the Sb_xTe_{1-x} thin films were positive at all temperatures, indicating a p-type semiconductor. However, transition of the values as the annealing temperature increased considerably differed from the composition of the films. In comparison with our previous report in enhancement of Seebeck coefficient in the two-phase γ-$SbTe/Sb_2Te_3$ nanocomposite (blue triangle) due to the formation of potential barriers at the interfaces between two phases, the initial Seebeck coefficient values of the amorphous $Sb_{33}Te_{67}$ and $Sb_{42}Te_{58}$ films were indicated as five- or six-times higher and suddenly dropped after 50 ^oC. Between 50 and 100 ^oC, the values from both films were remained ~ 200 $\mu V/K$ without significant changes. Once the films were further annealed at 150 ~ 200 ^oC, the distinct Seebeck coefficients (~150 $\mu V/K$) of the $Sb_{33}Te_{67}$ film were observed compared

to those (~50 μV/K) of the $Sb_{37}Te_{63}$ and $Sb_{42}Te_{58}$ films. Although the measured Seebeck coefficient from the $Sb_{37}Te_{63}$ and $Sb_{42}Te_{58}$ film were comparable to bulk single crystal (38 ~ 70 μV/K), the $Sb_{33}Te_{67}$ film kept almost three times higher values without reducing the transport properties. In case of the $Sb_{30}Te_{70}$ film, there was no significant change in Seebeck coefficient as a function of annealing temperature. However, as the sample annealing temeprature increased the Seebeck coefficient slightly but continuosly by 150 ^{o}C and droped just same as other films at 200 ^{o}C. The plot of P.F. of the Sb_xTe_{1-x} thin films, defined as $\sigma^2 S$, is shown as a function of annealing temperature in Figure 3.3(b). The highest P.F. value of each film was obtained at different annealing temperatures in respect of either maximum Seebeck coefficient or conductivity as indicated in the relationship of $\sigma^2 S$. The highest P.F. of the $Sb_{30}Te_{70}$ and $Sb_{42}Te_{58}$ films were observed of ~166 μW/mK and ~188 μW/mK at 150 and 200 ^{o}C, respectively, where two films had the relatively high conductivity instead of the Seebeck coefficient during the annealing process. Similar to these two films, the $Sb_{33}Te_{67}$ film also represented the high P.F. values of ~690 μW/mK at the same temperature region but the absolute values were four-times higher. This significant enhancement in P.F. of the $Sb_{33}Te_{67}$ is explained due to its three times higher Seebeck coefficient with highly maintained conductivities. The comparable P.F. value (i.g., ~590 μW/mK) was also obtained from the $Sb_{37}Te_{63}$ films at 80 ^{o}C as a result of increase in the Seebeck coefficient. In contrast to the $Sb_{33}Te_{67}$, the highest P.F. of $Sb_{37}Te_{63}$ was clearly contributed by abnormally increased Seebeck coefficient at that annealing temperature.

3.5 Discussion

The electrical transport and thermoelectric properties are dependent values as a function of physical properties of the materials. Various attempts to effectively optimize those physical properties such as a control of composition, crystallinity, prefer orientation, grain sizes and so on have been applied for chalcogenide materials with various dimension. In addition, animated by the development of nanotechnology, the interface engineering has been emerged as another important factor to additionally play with.

The γ-SbTe or elemental Te phase embedded nanocrystalline Sb_2Te_3 films were synthesized by solid-state phase transition from the composition-controlled Sb-Te solid solution. In addition, the control of annealing temperature demonstrated the variation of the grain size of single-phase nanocrystalline Sb_2Te_3 films, leading to the grain size effect on the electrical transport and thermoelectric properties as well. The aim of this work is to incorporate the energy filtering effect to optimize the thermoelectric performance of the nanocrystalline Sb_2Te_3 thin film in aspect at a tailor of the energy barrier height.

In the presence of nano-sized grains, the carriers with low kinetic energies are scattered at grain boundaries while high-energy carriers can pass through them, therefore, this strong energy-dependent scattering mechanism determines the electrical transport and thermoelectric performance of the nanocrystalline materials. In fact, the size of barrier height at which the carriers are trapped with the creation of accumulation or depletion regions is dominated by the level of carrier concentration and grain size. In the nanostructured matrix, the charge distribution can be expected by comparison to Debye length ($L_D = (\varepsilon k_B T/e^2 n)^{-1/2}$); a length of charge transport, where ε is the dielectric constant,

k_B is the Boltzmann constant, T is the absolute temperature, e is the electron charge, and n is the carrier concentration with the size of nanograins. Considering the ε for Sb_2Te_3 is of 51 at 300 K in the degenerate charge carrier level, the L_D is expected in the range of 1~3 nm, which is significantly small distance compared to size of the Sb_2Te_3 nanograin in this study (Table S1). For the nanocrystalline Sb_2Te_3, therefore, the governing transport mechanism is no longer valid to the ionized impurities scattering, but dominated by the grain-boundary scatterings. The conductivity, Seebeck coefficient and P.F. of the nanocrystalline Sb_2Te_3 films with different grain size (symbol of empty, triangle and square) are plotted as a function of the carrier concentration in Figure 3.4. Although they had a similar carrier concentration range, the film with smaller grain size (symbol of empty, square) showed lower conductivity due to the reduced mobility at grain boundaries. In contrast, a larger Seebeck coefficient was observed in this film, which is consistent with the reported data of the grain size dependent conductivity and Seebeck coefficient of Sb_2Te_3 thin films.[11] According to this work, the enhanced Seebeck coefficient in smaller particles was explained as the energy filtering effect from the charge carrier trapped in the grain boundaries regions. Therefore, the enhanced P.F. was investigated in the nanocrystalline Sb_2Te_3 films with smaller grain sizes as a result of the more efficient low energy carriers scattering at the grain boundaries.

Instead of the grain boundaries, the incorporation of second phases (i.e., metal or semimetal) into the Sb_2Te_3 film also allows the charge scatterings by creating heterostructure junctions. Various theoretical studies revealed that the energy filtering effect induced on the band bending at the interfaces is highly dependent on the carrier

concentration affecting the Fermi level of the materials and a size of the potential barrier height.[5-11] Unlike the grain boundary as a scattering center, the barrier height at the interfaces of nanocomposite is determined by the work function of the metal or semimetal phase and the electron affinity of semiconductor. Therefore, the energy filtering effect can be optimized by varying the type of incorporation materials at given carrier concentration of the Sb_2Te_3 films.

As indicated in the Figure 3.4b, the γ-SbTe and Te phase embedded nanocrystalline Sb_2Te_3 films showed the distinguished conductivity and carrier concentration changes. As the γ-SbTe phase was formed in the nanocrystalline Sb_2Te_3 film, the conductivity decreased with reduced carrier concentration. On the other hand, the formation of elemental Te in the Sb_2Te_3 film provided the increased conductivity and carrier concentration. Opposite to the conductivity changes as a function of carrier concentration, the Seebeck coefficient of the γ-SbTe/Sb_2Te_3 nanocomposite increased whereas the Seebeck coefficient of Te/Sb_2Te_3 nanocomposite decreased, which is consistent with Mott-relation. Interestingly, depending on the inclusion materials the carrier concentration, at which the highest P.F. values were observed, is shifted. As shown in the Figure 3.4c, compared to the single-phase nanocrystalline Sb_2Te_3 films, the inclusion of the γ-SbTe phase allowed the Sb_2Te_3 films to achieve the highest P.F. in reduced carrier concentrations. However, the Te embedded Sb_2Te_3 had the highest P.F. in higher carrier concentrations. Considering that the achieved highest P.F. values from both films are similar, the almost an order of difference in the carrier concentration of the

films implies the possibility to lower thermal conductivity without reducing P.F., consequently, the promising *zT*.

3.6 Conclusion

In conclusion, we investigated the incorporation of the energy filtering effect to optimize the thermoelectric performance of the nanocrystalline Sb_2Te_3 thin film in aspect of a tailor of the energy barrier height. The interfacial energy barrier scatterings in the nanocrystalline Sb_2Te_3 electrodeposits were simply controlled by adjusing the grain size at given carrier concentration in addition to the incorpolation of the γ-SbTe and Te phases. The effect of low energy carrier filtering at the interfaces with the different types of the barrier height was indicated by showing the enhanced Seebeck coefficient compared to the single-phase nanocrystalline Sb_2Te_3 without significant changes on the given carrier concentration.

3.7 References

[1] K. F. Hsu, S. Loo, F. Guo, W. Chen, J. S. Dyck, C. Uher, T. Hogan, E. K. Polychroniadis, M. G. Kanatzidis, *Cubic AgPbmSbTe2+m: Bulk Thermoelectric Materials with High Figure of Merit*, Science, 2004, **303** : p.818-821.

[2] J. M. O. Zide, D. Vashaee, Z. X. Bian, G. Zeng, J. E. Bowers, A. Shakouri, A. C. Gossard, *Demonstration of electron filtering to increase the Seebeck coefficient in ErAs:InGaAs/InGaAlAs superlattices*, Physical Review B, 2006, **74** : p.205335.

[3] R. Venkatasubramanian, E. Siivola, T. Colpitts, B. O'Quinn, *Thin-film thermoelectric devices with high room-temperature figures of merit*, Nature, 2001, **413** : p.597-602.

[4] J. P. Wiff, Y. Kinemuchi, H. Kaga, C. Ito, K. Watari, *Correlations between thermoelectric properties and effective mass caused by lattice distortion in Al-doped ZnO ceramics.* Journal of the European Ceramic Society, 2009. **29**(8): p. 1413-1418.

[5] S.V. Faleev, and F. Léonard, *Theory of enhancement of thermoelectric properties of materials with nanoinclusions.* Physical Review B, 2008. **77**(21): p. 214304.

[6] D.-K. Ko, Y. Kang, and C.B. Murray, *Enhanced Thermopower via Carrier Energy Filtering in Solution-Processable Pt–Sb2Te3 Nanocomposites.* Nano Letters, 2011. **11**(7): p. 2841-2844.

[7] Y. Zhang, M. L. Snedaker, C. S. Birkel, S. Mubeen, X. Ji, Y. Shi, D. Liu, X. Liu, M. Moskovits, G. D. Stucky, *Silver-Based Intermetallic Heterostructures in Sb2Te3 Thick Films with Enhanced Thermoelectric Power Factors.* Nano Letters, 2012. **12**(2): p. 1075-1080.

[8] S. Sumithra, N. J. Takas, D. K. Misra, W. M. Nolting, P. F. P. Poudeu, K. L. Stokes, *Enhancement in Thermoelectric Figure of Merit in Nanostructured Bi2Te3 with Semimetal Nanoinclusions.* Advanced Energy Materials, 2011. **1**(6): p. 1141-1147.

[9] D. Narducci, E. Selezneva, G. Cerofolini, S. Frabboni, G. Ottaviani, *Impact of energy filtering and carrier localization on the thermoelectric properties of granular semiconductors.* Journal of Solid State Chemistry, 2012. **193**(0): p. 19-25.

[10] J. Martin, L. Wang, L. Chen, G. S. Nolas, *Enhanced Seebeck coefficient through energy-barrier scattering in PbTe nanocomposites.* Physical Review B, 2009. **79**(11): p. 115311.

[11] J. Chen, T. Sun, D. Sim, H. Peng, H. Wang, S. Fan, H. Hng, J. Ma, F. Y. C. Boey, S. Li, M. K. Samani, G. C. K. Chen, X. Chen, T. Wu, Q. Yan, *Sb2Te3 Nanoparticles with Enhanced Seebeck Coefficient and Low Thermal Conductivity.* Chemistry of Materials, 2010. **22**(10): p. 3086-3092.

[12] J.-H. Bahk, Z. Bian, and A. Shakouri, *Electron transport modeling and energy filtering for efficient thermoelectric Mg2Si1-xSnx solid solutions.* Physical Review B, 2014. **89**(7): p. 075204.

[13] H. Jung, and N.V. Myung, *Electrodeposition of antimony telluride thin films from acidic nitrate-tartrate baths.* Electrochimica Acta, 2011. **56**(16): p. 5611-5615.

[14] Q. Huang, A.J. Kellock, and S. Raoux, *Electrodeposition of SbTe Phase-Change Alloys.* Journal of The Electrochemical Society, 2008. **155**(2): p. D104-D109.

[15] M.-Y. Kim, and T.-S. Oh, *Crystallization behavior and thermoelectric characteristics of the electrodeposited Sb2Te3 thin films.* Thin Solid Films, 2010. **518**(22): p. 6550-6553.

[16] M. Wuttig, and N. Yamada, *Phase-change materials for rewriteable data storage.* Nat Mater, 2007. **6**(11): p. 824-832.

[17] S.-H. Lee, Y. Jung, and R. Agarwal, *Size-Dependent Surface-Induced Heterogeneous Nucleation Driven Phase-Change in Ge2Sb2Te5 Nanowires.* Nano Letters, 2008. **8**(10): p. 3303-3309.

[18] B.J. Kooi, W.M.G. Groot, and J.T.M. De Hosson, *In situ transmission electron microscopy study of the crystallization of Ge2Sb2Te5.* Journal of Applied Physics, 2004. **95**(3): p. 924-932.

[19] G. F. Zhou, H. J. Borg, J. C. N. Rijpers, M. Lankhorst, *Crystallization behavior of phase change materials: comparison between nucleation- and growth-dominated crystallization*. in *Optical Data Storage, 2000. Conference Digest*. 2000.

[20] M. L. Lee, L. P. Shi, Y. T. Tian, C. L. Gan, X. S. Miao, *Crystallization behavior of Sb70Te30 and Ag3In5Sb60Te32 chalcogenide materials for optical media applications.* physica status solidi (a), 2008. **205**(2): p. 340-344.

[21] M. Horie, N. Nobukuni, K. Kiyono, T. Ohno, *High-speed rewritable DVD up to 20 m/s with nucleation-free eutectic phase-change material of Ge(Sb70Te30)+Sb*, 2000, p. 135-143.

[22] Ghosh, G., *The Sb-Te (antimony-tellurium) system.* Journal of Phase Equilibria, 1994. **15**(3): p. 349-360.

[23] K. Kifune, Y. Kubota, T. Matsunaga, N. Yamada, *Extremely long period-stacking structure in the Sb-Te binary system.* Acta Crystallographica Section B, 2005. **61**(5): p. 492-497.

[24] K. Govaerts, M. H. F. Sluiter, B. Partoens, D. Lamoen, *Stability of Sb-Te layered structures: First-principles study.* Physical Review B, 2012. **85**(14): p. 144114.

[25] C. Guo, C. Li, and Z. Du, *Thermodynamic Re-modeling of the Sb-Te System Using Associate and Ionic Models.* Journal of Electronic Materials, 2014. **43**(11): p. 4082-4089.

[26] Z. Zhang, F. Zhou, and E.J. Lavernia, *On the analysis of grain size in bulk nanocrystalline materials via x-ray diffraction.* Metallurgical and Materials Transactions A, 2003. **34**(6): p. 1349-1355.

[27] Rowe, D.M., *CRC Handbook of Thermoelectrics.* CRC Press, Inc.: Boca Raton, 1995.

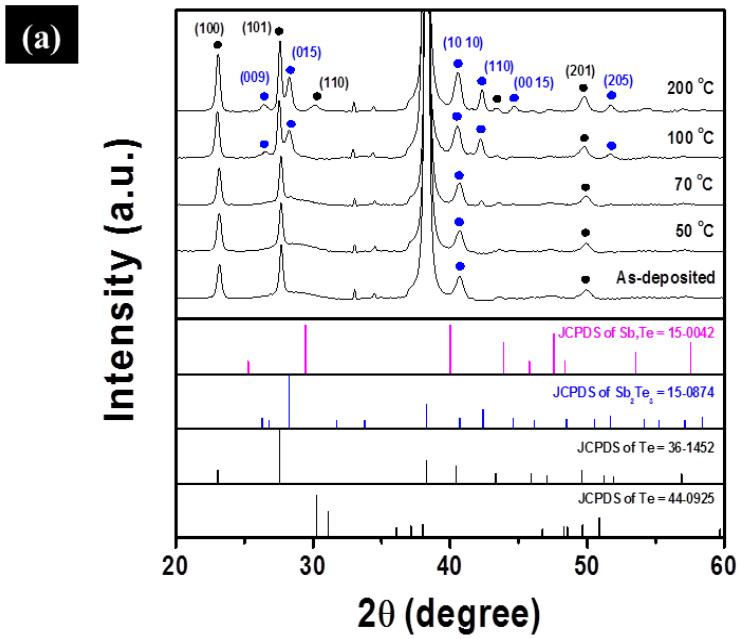
(a)
(100)
(101)
(015)
(009)
(110)
(10 10)
(110)
(00 15)
(201)
(205)
200 °C
100 °C
70 °C
50 °C
As-deposited
JCPDS of Sb,Te = 15-0042
JCPDS of Sb2Te3 = 15-0874
JCPDS of Te = 36-1452
JCPDS of Te = 44-0925
Intensity (a.u.)
20
30
40
50
60
2θ (degree)

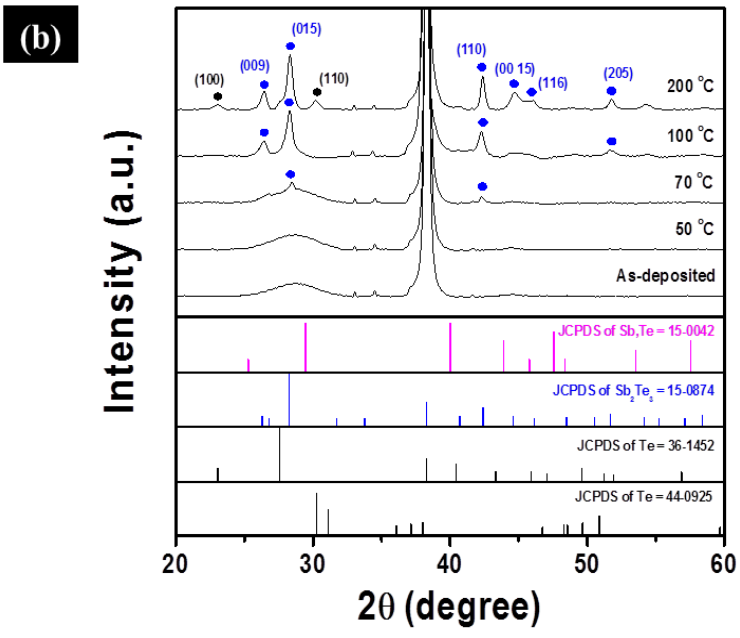
(b)
(100)
(009)
(015)
(110)
(110)
(00 15)
(116)
(205)
200 °C
100 °C
70 °C
50 °C
As-deposited
JCPDS of Sb,Te = 15-0042
JCPDS of Sb2Te3 = 15-0874
JCPDS of Te = 36-1452
JCPDS of Te = 44-0925
Intensity (a.u.)
20
30
40
50
60
2θ (degree)

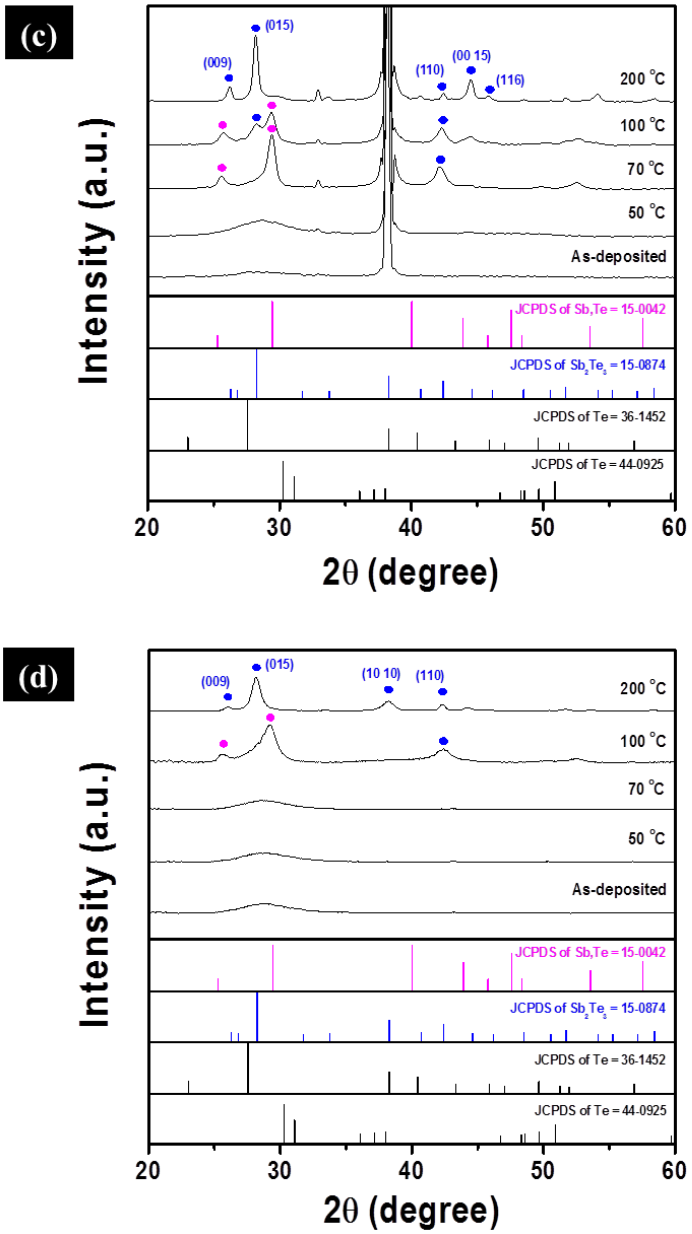

Figure 3.1 Annealing temperature-dependent XRD analysis of $Sb_{30}Te_{70}$ (a), $Sb_{33}Te_{67}$ (b), $Sb_{37}Te_{63}$ (c), and $Sb_{42}Te_{58}$ thin films.

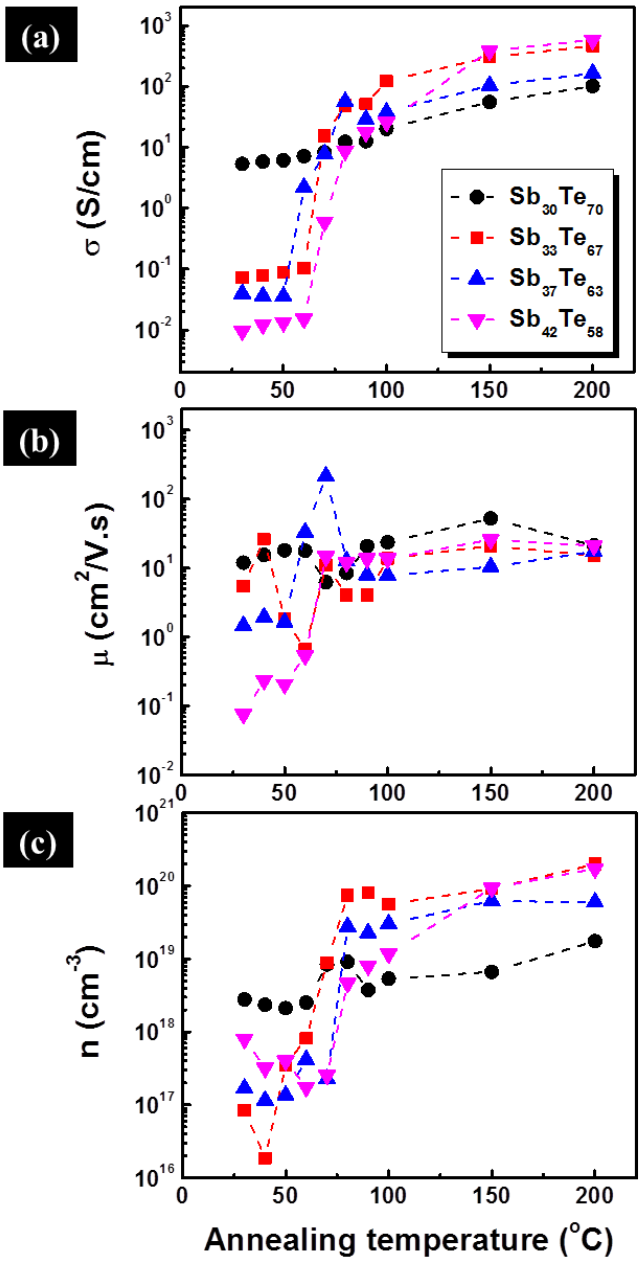

Figure 3.2 Electrical conductivity (a), Hall mobility (b), and carrier concentration (c) of Sb_xTe_{1-x} thin films as a function of annealing temperature. Measurement was conducted in room temperature.

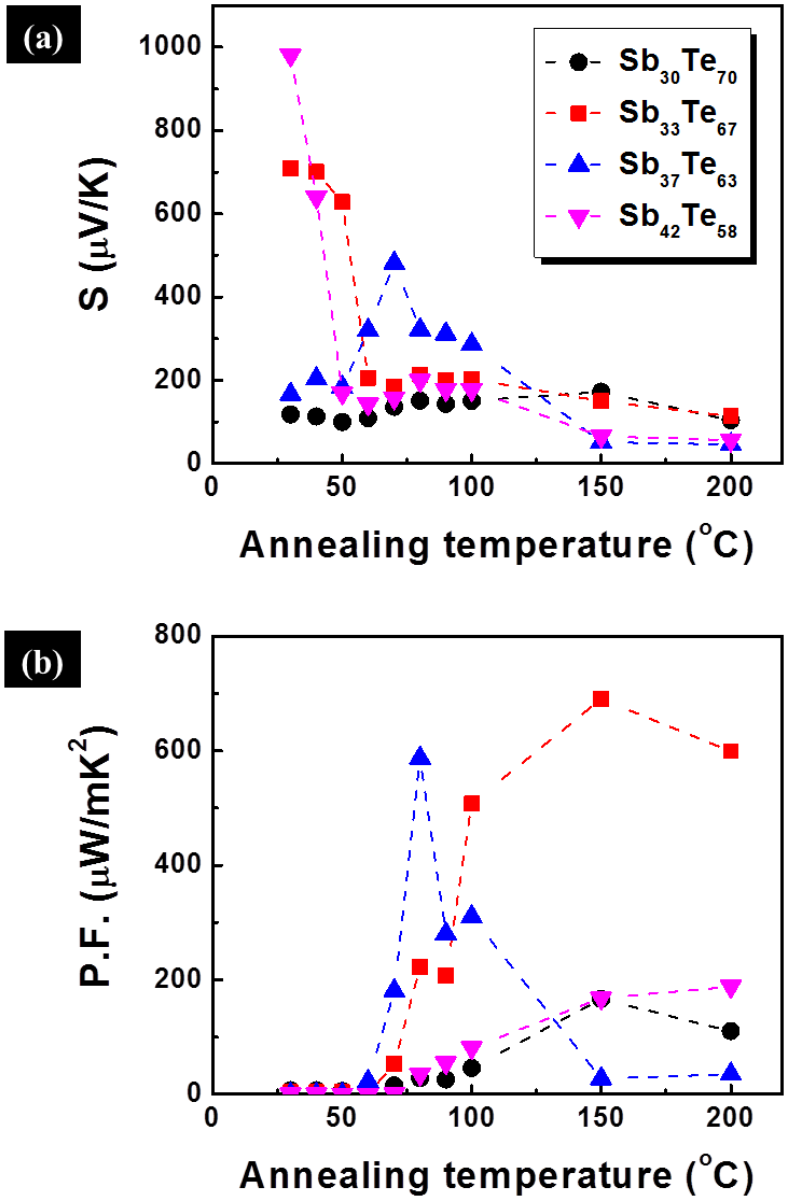

Figure 3.3 Seebeck coefficient (a) and Power factor (P.F.) of Sb_xTe_{1-x} thin films as a function of annealing temperature. Measurement was conducted in room temperature.

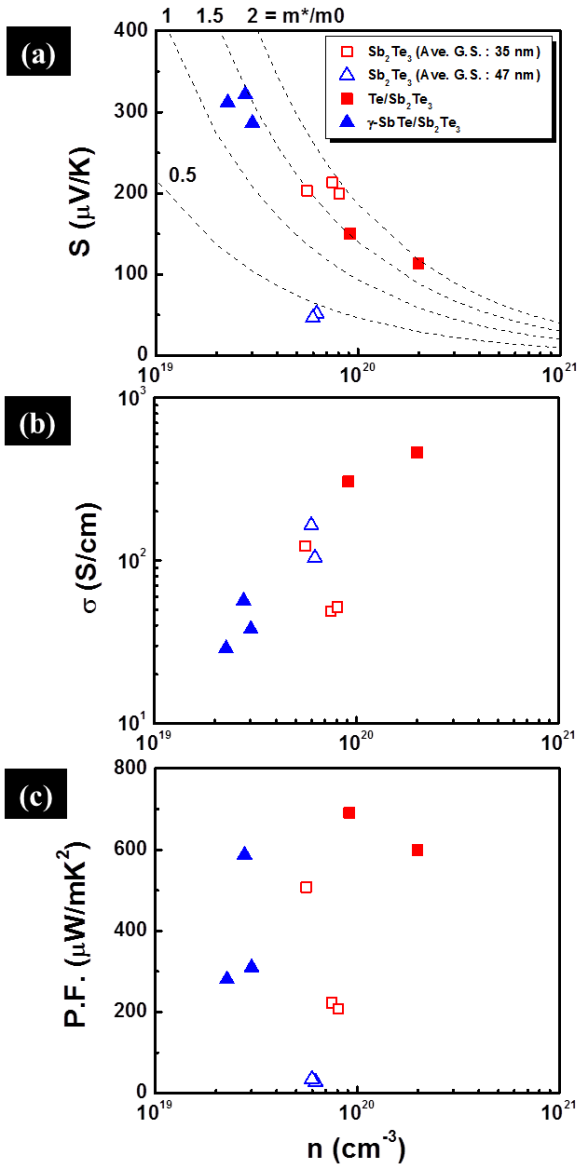

Figure 3.4 Dependence of nanoinclusion materials on electrical and thermoelectric properties of nanocrystalline Sb_2Te_3 film: Seebeck coefficient (a), electrical conductivity (b), and Power factor (c) of Single-phase, γ-SbTe phase, and Te phase embedded nanocrystalline Sb_2Te_3 thin films. Difference in shape of symbol indicates their average grain size difference.

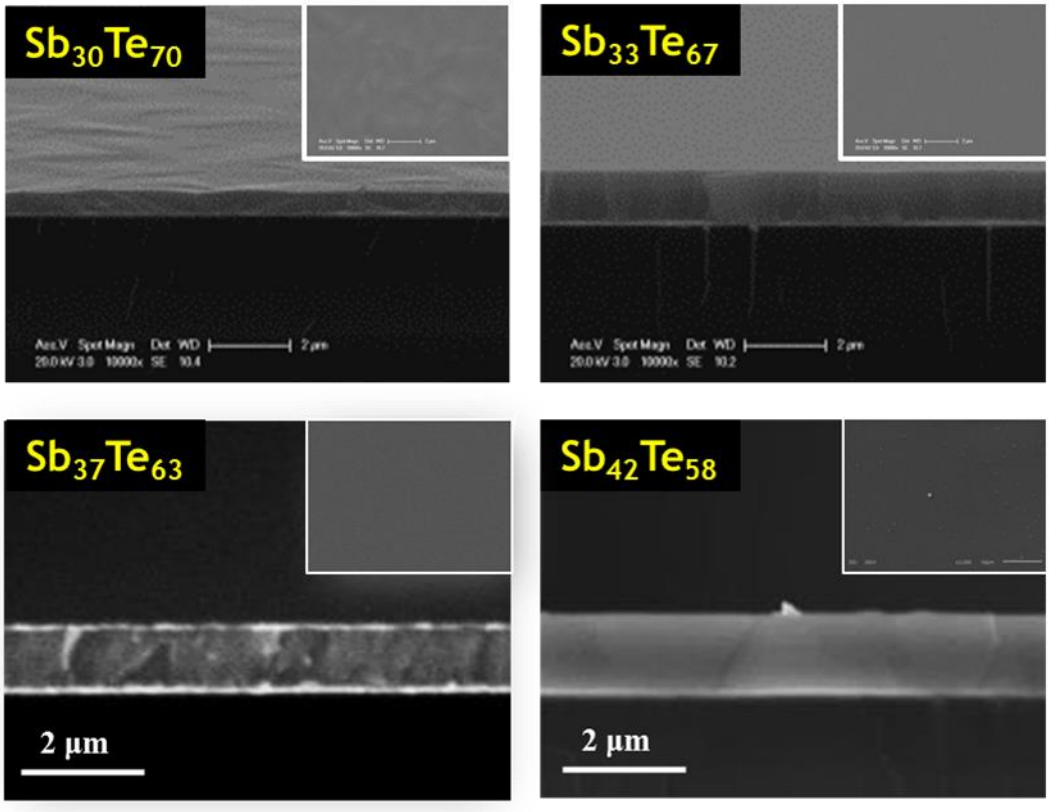

Figure 3.5 SEM images of as-deposited Sb_xTe_{1-x} thin films. Insets are indicated the surface morphology of each film.

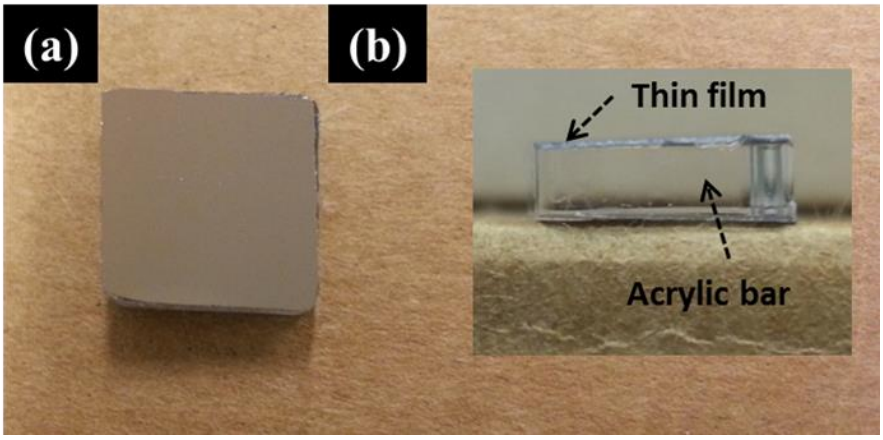

Figure 3.6 Schematics of measurement sample. The top-view (a) and cross-section view (b) of transferred Sb_xTe_{1-x} film on epoxy/ Acrylic bar.

CHAPTER 4 Composition-Dependent Structural and Thermoelectric Properties of Ag-Doped SbxTey Electrodeposits

4.1 Abstract

A direct correlation of the composition and crystal structure changes with the electrical and thermoelectrical properties successfully provided the optimum conditions of the Ag-doped Sb_xTe_y thin films for thermoelectric application. The modulated crystal structures and crystallographic orientation of the films based on the composition-dependent crystallization process was demonstrated by post annealing the composition-tailored amorphous films. Moreover, the Ag atoms were incorporated into the Sb_xTe_y thin film as an acceptor dopant to control the transport properties. Among the various compositions made in this work, it was found that the small amount of Ag doping did not influence the final crystal structure or its preferred orientation. Instead, Ag atoms were substituted into the Sb lattices as acceptor dopants to enhance the transport property of the films. The optimal power factor of ~1870 $\mu W/mK^2$ was obtained in the $Ag_{1.5}Sb_{31.5}Te_{67.1}$ film – retaining the single-phase of rhombohedral Sb_2Te_3 with a preferred orientation of (110) – with the highest conductivity of 1.82 x 10^3 S/cm and Seebeck coefficient of 101μV/K.

4.2 Introduction

The growing interest in using microdevices for thermoelectric (TE) generation under low temperature waste heat recovery systems has focus developments on low-dimensional TE

materials. For commercial, low temperature applications, a microdevice must have an efficiency of merit, zT > 1.5, where zT $=\alpha^2\sigma T/\kappa$, and where T is the absolute temperature, α is the Seebeck coefficient, σ and κ are the electrical and thermal conductivity, respectively. Even though 1-D nanostructures have yielded viable low temperature TE materials (e.g., Sb_2Te_3-Bi_2Te_3 among the various highly degenerate semiconductors) based on expectations of anomalous transport based on quantum confinement and distorted lattices structure effect,[1,2] their current synthesis is limited by slow deposition rates, poor parameter controls over crystal structure and crystallographic orientation, and expensive and complicated equipment. These prevailing conditions, limiting the scale-up integration of 1-D nanostructures, have led the field toward more controlling but facile synthesis methods yielding comparable or improved performance in 2-D TE nanostructures such as thin or thick films for commercial small-scale applications using microdevices under low-temperature operations.

Antimony telluride (Sb_2Te_3), with a narrow band gap energy of 0.1 ~ 0.28 eV, has been thoroughly investigated as a starting base material for a wide range of applications.[3-5] For example, tailoring the composition and crystallinity, including doping and/or alloying with other metals, have yielded thermally driven rapid and reversible amorphous-crystalline phase changes for optical and electronic switching applications. Specific to the Sb_2Te_3 as a TE material, crystals are observed to form in specific crystallographic directions. Such evidence points strongly toward anisotropy in the migrational characteristics of an interface assumed growing under a diffusion controlled mechanism– i.e. an interfacial kinetic coefficient strongly modified by

crystallographic effects. Here, a high zT depends not only on the microstructure and grain size of the crystalline phase and their interfaces, but it also depends on their crystallographic orientation. Such crystallographic anisotropy in the Sb_2Te_3 is due to its layered lattice structure consisting of atomic layers of Te held together by weak van der Waal forces while the Te-Sb atoms within the layers are held together by strong covalent bonds. Therefore, the goal is to utilize a synthesis method that offers the best process controls over the final crystalline structures and their growth direction which optimizes the electrical and the thermoelectric properties of the deposited film.[6]

The degree to which one can actually achieve such crystalline control over deposited films, however, completely depends on the applied synthesis technique. Various synthesis techniques, including the thermal evaporation,[7-10] sputtering deposition,[11,12] chemical vapor deposition,[13,14] and recently solution phase reaction,[15,16] have been utilized for the Sb_2Te_3 thin films to evaluate the improved electrical transport and thermoelectric properties. Room temperature measurements of the electrical conductivity, the Seebeck coefficient, and the power factor (P.F.) ranged from 40 to 3500 S/cm, 25 to 171μV/K, and 60 to 6,000μW/m.K^2, respectively. Such variations are probably related to deviations in the structural properties and in the level of native defects in the synthesized Sb_2Te_3 thin films. Although some of the conventional processes have successfully demonstrated competitive results with that of bulk single crystals of Sb_2Te_3, these methods are limited for scale-up due to their very slow film deposition rates, expensive and complicated equipment, and a lack of process parameters that can precisely control the film's final crystalline structure and uniformity in

crystallographic orientation which yield high zT materials suitable to manufacture TE microdevices.

Electrodeposition is one of the most versatile, repeatable and consistent film depositing techniques that overcome the above drawbacks of other deposition methods when it comes to facile, high volume manufacture of TE thin films. The reaction-kinetics associated with the formation of stable and/or meta-stable films can be simply controlled by varying electrochemical parameters including applied potential, electrolyte composition/concentration, temperature, agitation, and additives. Bachmann *et al.* demonstrated improvements in the morphology and composition of Sb_2Te_3 thin films that yielded a P.F. of ~ 852 $\mu W/m.K^2$ by utilizing a millisecond potentiostatic pulsed deposition technique followed by a post-annealing process.[17] Crystallographic parameters confirmed that the enhanced TE properties of the film were the direct result in improved film crystallinity. In addition, changes in the Sb_2Te_3 film's thermal conductivity were correlated with changes in the film's texture, microstructure, and orientation as a function of the pulse-interval reported by D.L. Medlin *et al*..[18]

Improved thermoelectric performance can be also achieved by modifying the microstructure and electronic band structure of thermoelectric materials.[19,20] Specifically, local distortions in the electronic band structure, presumed to be induced by structural defects from doping, can serve as critical scattering mechanisms leading to augmented transport properties.[21] Since the electrical and thermal conductivity and Seebeck coefficient are factors in determining zT, and each of these parameters in turn are dependent on scattering centers, there have been many studies trying to resolve these

three parameters as de-coupled functions of extrinsic carrier concentration under various time-temperature TE profiles. It is known that dopants such as Ag, In, and Tl in a narrow-gap layered Sb_2Te_3 structure can be located in Sb-sublattice, thus augmenting the concentration of antisite defects and holes.[22-24] Therefore, doping is viewed as a potential approach to optimize the thermoelectric properties of Sb_2Te_3 films by reducing its thermal conductivity while augmenting the carrier concentration.

In this work, a direct correlation of the composition and crystal structure changes with the electrical and thermoelectrical properties successfully provided the optimum conditions of the Ag-doped Sb_xTe_y thin films for thermoelectric application. The modulated crystal structures and crystallographic orientation of the films based on the composition-dependent crystallization process was demonstrated by post annealing the composition-tailored amorphous films. Moreover, the Ag atoms were incorporated into the Sb_xTe_y thin film as an acceptor dopant to control the transport properties.

4.3 Experimental Section

Amorphous Ag-doped Sb_xTe_y thin films were potentiostatically electrodeposited onto Si substrates terminated with Au (80 nm)/ Ni (20 nm) evaporated films. The electrolyte contained 2.4 mM TeO_2, 3.6 mM Sb_2O_3, 1 M HNO_3, and 33 mM L-tartaric acid as a complexing agent, and 100 μM $AgNO_3$ was poured into the final electrolyte mixture. Details of the electrolyte preparation is described elsewhere.[25] The electrodeposition was performed under an applied potential range from -0.1 to -0.14 V (V vs. SCE) at room temperature with stirring at 300 rpm. A Pt coated titanium and a saturated calomel

electrode (SCE) were used as the counter and the reference electrode, respectively. Film thickness was controlled by the total charge transferred at 2.8 mA.hr yielding films between 1~2 μm.

Morphology and composition of the synthesized Ag-doped Sb_xTe_y thin films were analyzed by scanning electron microscopy (SEM) (Jeol, JSM-5800) and energy dispersive X-ray spectroscopy (EDS). X-ray photoelectron spectroscopy (XPS) was used to identify the chemical binding states of the films, and crystallinity and crystal structure were investigated by X-ray diffraction (XRD) (Bruker D8 ADVANCE). A post-annealing process at 100 ^oC for 30 minutes under a reducing atmosphere of 5 % H_2/ 95 % Ar was performed to survey the crystallization process as a function of film composition.

As-deposited films were prepared for electrical characterization by transferring them from the conducting Si substrate to a non-conductive acrylic mandrel (Torr Seal epoxy - Varian Vacuum Products- Lexington, Massachusetts) which was cured over night at room temperature. The film's electrical conductivity, carrier concentration, and Hall mobility were all measured at room temperature by a custom-made Hall measurement unit with four-point probes in the van-der-Pauw configuration. The Seebeck coefficient ($S = \Delta V/\Delta T$) was determined by a custom-made Seebeck measurement system by plotting measured Seebeck voltages as a function of the temperature gradient (< 2 ^oC) across the sample.

4.4 Results and Discussion

4.4.1 Synthesis and Material Characterization

The composition of undoped and Ag-doped Sb_xTe_y thin films as a function of applied potential and electrolyte concentration is shown in Figure 4.6. Open symbols indicate the results of the electrolyte - 2.4 mM $HTeO_2^+$, 3.6 mM $[Sb(C_4H_2O_6)_2]^{-2}$, 33 mM $C_4H_6O_6$, 1M HNO_3- without Ag^+ doping, and the solid symbols indicate the results of the electrolyte with 100 µm Ag^+ doping. As the applied potential becomes more negative and closer to the over potential of Sb, the Sb content in the films increases. Mechanisms of the electrodeposition of Sb_xTe_y thin films in nitric baths are explained in our previous works.[25,26] The amount of Ag atoms incorporated within the Sb_xTe_y structure is controlled by modulating the applied potential. For example, when the potential was changed from -0.1 to -0.14 (V vs. SCE), the Ag in the Sb_xTe_y structure changed from 0.8 and 1.9 at. %, respectively - as confirmed by EDS. It is known that dopants such as Ag, In, and Tl in narrow-gap layered Sb_2Te_3 structures can be located in the Sb-sublattice; thus, the applied potential controls the concentrations of antisite defects and holes in the Ag-doped structures.[22,23] In our experiments, the Ag content was slightly reduced as the Sb content of the film increased. This result might be due to the competition between Sb and Ag during the electrodeposition. The morphologies of $Sb_{37}Te_{63}$, $Sb_{42}Te_{58}$, $Ag_{1.5}Sb_{31.5}Te_{67.1}$, $Ag_{1.9}Sb_{33.1}Te_{65}$, $Ag_{0.8}Sb_{38.7}Te_{60.5}$, and $Ag_{0.9}Sb_{41}Te_{58.1}$ thin films are shown in Figures 4.7(a-f). The surface morphologies of all the films (1-2 um thick) were smooth and dense and believed to be homogeneous.

The crystallinity and crystal structure of the electrodeposits were further investigated by XRD analysis. Figure 4.1(a) shows the XRD 2(Θ) scan results of the as-deposited films. Since no peaks were detected, except those for Au/Ni/Si from the original substrate, the results confirm that all the as-deposited films are amorphous. For the purpose of tailoring the crystallinity and crystal structure of the films, the post-annealing process was applied. To repeat, the films were annealed at 100 ^{o}C for 30 minutes in a reducing 5 % H_2, 95 % Ar environment. The XRD results of the annealed $Sb_{37}Te_{63}$, $Sb_{42}Te_{58}$, $Ag_{1.5}Sb_{31.5}Te_{67.1}$, $Ag_{1.9}Sb_{33.1}Te_{65}$, $Ag_{0.8}Sb_{38.7}Te_{60.5}$, and $Ag_{0.9}Sb_{41}Te_{58.1}$ thin films shown in Figure 4.1(b) are arranged in order of increasing Te composition. Overall, the Ag was not observable in any X-ray peaks due to its very low doping level.[24] However, two distinct crystal structures were apparent in the post annealed films when the Te content was between 58 and 67.1 at. %. Recently, we reported the observation of γ-SbTe/Sb_2Te_3 nanocomposites from the amorphous $Sb_{37}Te_{63}$ thin film after solid-state phase transition. Under the same annealing condition, however, the formation of the preferred crystal structure differed as the Te content. When the Te content was less than 60 at%, the formation of an intermediate phase, referred to γ-SbTe (JCPDS 15-0042), was predominant. When the Te content was greater than 63 at %, where the mixed two-phase was observed our results indicate that the film crystallized into the stable Sb_2Te_3 structure (JCPDS 15-0874) rather than the mixture or γ- SbTe phase - which is expected from the Sb-Te phase diagram. Based on various structural analyses on the Sb-Te system, consisting of many intermetallic stable and meta-stable phases, the crystal structures of this binary system are strictly determined by the chemical

composition.[27,28] Specifically, it is known that when the Te concentration is between 0 and 60 at. %, an almost continuous series of meta-stable structures (e.g., γ- and σ-phase) are observable.[29] The formation of different crystal structures in our films after crystallization is ascribed to the variation in their compositions. Interestingly, not only is the crystal structure a function of Te content, but we find that the crystal growth orientation is also a function of Te content. Unlike the $Ag_{1.9}Sb_{33.1}Te_{65}$ film, the $Ag_{1.5}Sb_{31.5}Te_{67.1}$ film has the preferred orientation toward the (110) direction, which is be expected to augment the electrical and thermoelectrical properties of the film due to its anisotropy.[6,30] Moreover, the $Ag_{0.9}Sb_{41}Te_{58.1}$ thin film, where the composition is relatively similar to the binary $Sb_{42}Te_{58}$ thin film, has a similar XRD pattern. Thus, among the various compositions made in this work, it was found that the small amount of Ag doping does not influence the film's final crystal structure or its preferred orientation. Both of these parameters were successfully varied by the Sb-Te composition-dependent crystallization induced by the post-annealing process.

The atomic-percent of Ag doping was confirmed by investigating the binding states of the films. Figure 4.2(a) shows a wide range XPS spectrum of the annealed $Ag_{1.9}Sb_{33.1}Te_{65}$ thin film. The spectrum revealed the presence of Sb, Te, and Ag in the film. The peaks assigned as Te 3d5 (572.9 eV), Te 3d3 (583.3 eV) (Figure 4.2d) ,and Sb 3d5 (529.2 eV), Sb3d3 (538.5 eV) (Figure 4.2c) represent Sb and Te metallic bonding.[31] Moreover, the clear peaks, indicating Ag 3d5 (368.3 eV) and Ag 3d3 (374.3 eV), verify the existence of Ag in the film (Figure 4.2b). In order to assess the bonding states of Ag within the compound, these binding energy were compared to XPS results of

Ag_2Te nanowires.[32] The binding energy of the peaks corresponding to Ag 3d5 and Ag 3d3 in the $Ag_{1.9}Sb_{33.1}Te_{65}$ film are the same as that of Ag_2Te nanowires. Therefore, it ascribed that the Ag atoms were substituted into the Sb sublattice and attributed to the Ag-Te metallic bonding in this film.

4.4.2 Electrical and Thermoelectric Characterization

Improved thermoelectric performance can be achieved by modifying the microstructure and electronic band structure of the thermoelectric materials. Specifically, the local distortion of the electronic band structure, which can be possibly induced by structural defects from doping, can serve critical scattering mechanisms, leading to unique transport properties. The effect of the Ag-doping on the electrical transport property was investigated by the Hall measurement. Fig. 4.3 shows the variation in the electrical conductivity, Hall mobility, and carrier concentration as a function of the (Ag+Sb)/Te ratio in the electrodeposits. The values were measured at room temperature after annealing at 100 ^oC for 30 min in order to correlate them with the varied crystallographic properties of the films. Symbols of empty circle and square represent the results from the undoped $Sb_{37}Te_{63}$ and $Sb_{42}Te_{58}$ films, respectively. The results from $Ag_{1.5}Sb_{31.5}Te_{67.1}$, $Ag_{1.9}Sb_{33.1}Te_{65}$, $Ag_{0.8}Sb_{38.7}Te_{60.5}$, and $Ag_{0.9}Sb_{41}Te_{58.1}$ films were indicated using the solid symbols with distinguished shapes. The conductivity of the film increased as its (Ag+Sb)/Te ratio increased – as the results of the mobility and carrier concentration changes. As shown in the Figure 4.3(c), the measured carrier concentration of Ag-doped films was relatively higher than that of undoped films. The Ag-doping effect

on the electrical transport was observed by comparison with two films ($Sb_{42}Te_{58}$ and $Ag_{0.9}Sb_{41}Te_{58.1}$) indicated as the (Ag+Sb)/Te ratio of 0.72. The carrier concentration of $Ag_{0.9}Sb_{41}Te_{58.1}$ rose threefold compared to it of $Sb_{42}Te_{58}$, and gradually increased up to 6.7×10^{20} cm^{-3} as the (Ag+Sb)/Te ratio decreased to 0.54 followed by slight drop at 0.49. On the contrary to the carrier concentration, the Hall mobility of the $Ag_{0.9}Sb_{41}Te_{58.1}$ film was reduced to almost one tenth of that of $Sb_{42}Te_{58}$. Such decline in the mobility of Ag-doped films were maintained as the (Ag+Sb)/Te ratio decreased to 0.54. However, an exceptional rise in the mobility was observed in the $Ag_{1.5}Sb_{31.5}Te_{67.1}$. The electrical conductivity of $Ag_{0.9}Sb_{41}Te_{58.1}$ was slightly reduced compared to it of $Sb_{42}Te_{58}$ due to a larger contribution of the reduced mobility than the increased carrier concentration. As the (Ag+Sb)/Te ratio decreased, however, the conductivity increased monotonically, and eventually represented the highest value in the $Ag_{1.5}Sb_{31.5}Te_{67.1}$ due to the increased mobility and carrier concentration simultaneously. In fact, the relationship between the concentration of anti-site defects in narrow band gap semiconductors and the bond polarization has been thoroughly investigated. For instance, the effect of various doping (e.g., In, Ti, S, Sn, and Ag) on the electronic structure and transport properties of the Sb_2Te_3 structure was explored to resolve the issue of the native anti-site defects.[22-24,33] An acceptor- or donor-like behavior of the incorporated dopants in Sb_2Te_3 is determined by their location within the lattice; i.e. either interstitial or substitutional. Specifically, the incorporation of Ag atoms into the Sb_2Te_3 structure is Sb-substitutional displaying acceptor-like behavior with localized σ-bonds. According to M. Stordeur *et al.,* Ag doping in single crystal Sb_2Te_3 increased the hole concentration, which led to the

increase in electrical conductivity.[22] This explanation is in good agreement with our experimental results where controlling the Ag content of the film tailors the conductivity of the film. However, it is worth to notice that the Ag-doped thin films tended to have lower mobility values compared to the undoped films. It was reported that the dopants such as Bi, Te, and In in the binary Sb-Te system were apprised to degrade the mobility at even low concentration.[24] This observation reveals that the small amount of Ag incorporation can tailor the electrical transports in the film along with the expectation of change in TE properties.

The electrical conductivity, Seebeck coefficient, and power factor (P.F. = $\sigma\alpha^2$) of undoped and Ag-doped Sb_xTe_{1-x} thin films are depicted as functions of (Ag+Sb)/Te ratio in Figure 4.4. The indicated values were measured at room temperature after the crystallization (at 100 ^oC for 30 min). As shown in the Figure 4.4(a), the electrical conductivity varied in the wide range of $10^1 \sim 10^3$ S/cm, which is proportional to the Te content in the films. Independent of Ag doping, a decrease in the film's (Ag+Sb)/Te ratio leads to an increase in electrical conductivity. The Seebeck coefficients in the films were positive at all of the annealing temperatures, indicating that the films were p-type semiconductors. The Seebeck coefficient of the Ag-doped films was independent of the Te content maintaining around 100μV/K. The abnormally high Seebeck coefficient of a film when (Ag+Sb)/Te =59 at. % is due to its unique two-phase γ-SbTe/Sb_2Te_3 thin film, where a γ-SbTe nanoinclusion is embedded in a nanocrystalline Sb_2Te_3 matrix. The strong energy-dependent charge scattering, called the energy filtering effect (EFE), was operational at the interfaces between two the phases, thus, increasing the Seebeck

coefficient. The slight reduction in the film's conductivity is consistent with the reduction in the net charge carrier concentration due to the EFE. A similar, but less effective, TE enhancement was observed in the $Sb_{42}Te_{58}$ film. This might be because the portion of rhombohedral structure, especially in the (015) oriented phase, was less developed compared to the $Sb_{37}Te_{63}$ film, reducing the EFE. Due to the uniform Seebeck values, the P.F. of the films was strongly dependent on the film's conductivity. Therefore, the Ag-doped enhanced conductivity contributed directly to the enhancement in the P.F. of the films.

The Seebeck coefficient and P.F. of the undoped and Ag-doped electrodeposits are plotted as functions of the electrical conductivity in Figure 4.5. The values from the bulk single crystal Sb_xTe_y (symbol of empty star) and reported results from electrodeposited Sb_2Te_3 thin films (symbol of empty circle and square) are also included for comparison. It is worth to notice that the sequence of the conductivities and P.F. from all samples is clearly correlated to their structural properties. As indicated in the XRD analysis (Figure 4.1), the preferred crystal structures and orientations were clearly varied among the films. The results represent that the $Ag_{0.8}Sb_{38.7}Te_{60.5}$ and $Ag_{0.9}Sb_{41}Te_{58.1}$ films with the mixed-phases displayed lower conductivity values compared to the $Ag_{1.5}Sb_{31.5}Te_{67.1}$ and $Ag_{1.9}Sb_{33.1}Te_{65}$ films which obtained predominately single-phase rhombohedral structures. In addition, not only the effect of the crystal structures, but the clear anisotropic behavior on the thermoelectric property was investigated as a function of crystallographic orientation of the films. Comparison between the $Ag_{1.5}Sb_{31.5}Te_{67.1}$ and the $Ag_{1.9}Sb_{33.1}Te_{65}$ films, which both have a single-phase rhombohedral structure, the

$Ag_{1.5}Sb_{31.5}Te_{67.1}$ thin film with preferred orientation toward (110) direction has a higher conductivity value. This anisotropic property can be explained by understanding the crystal structure of Sb_2Te_3. The crystal structure of rhombohedral Sb_2Te_3 is a layered anisotropic lattice structure with the Te and Sb atom layers arranged in the order of -Te_1-Sb-Te_2-Sb-Te_1- along the c-axis direction.[6] Different types of bindings such as van der Waal bonding between two adjacent Te_1 layers and covalent bonding between Te-Sb within the layers cause the strong anisotropic transport properties. The measured conductivity and P.F. values from this film are comparable to the published results obtained by the conventional synthesis techniques known as high conductivities (Figure 4.8). Specially, two-times higher P.F. of $Ag_{1.5}Sb_{31.5}Te_{67.1}$ film than that of the films prepared by the electrodeposition[17,34] might be due to the synergetic effect of the preferred crystal orientation and Ag doping, which were also supported by measurement of electrical transport properties. Therefore, this observation clearly manifests that precise control of the structural properties and doping leads to improvements of the electrical conductivity; thus, P.F. of the electrodeposits.

4.5 Conclusion

In conclusion, the thermoelectric and transport properties of electrodeposited Ag-doped Sb_xTe_y thin amorphous films were correlated and optimized with respect to chemical composition and their final crystallographic properties. A post-annealing process induced the final solid state amorphous-crystalline phase transition. Under the phase transition, the formation of the various phases ranged from the predominant metastable γ-SbTe

phase to the rhombohedral Sb_2Te_3 phase as the Te content was increased from 58 and 67.1 at. %. The change in the crystal's crystallographic orientation was also determined and correlated with the film's TE properties. Moreover, the Ag atoms incorporated into the Sb_xTe_y thin films acted as an acceptor dopant and increased the predominant hole carrier concentration. Among the various compositions, the optimized power factor of ~1870 $\mu W/mK^2$ was observed in the $Ag_{1.5}Sb_{31.5}Te_{67.1}$ thin film remained a single-phase of rhombohedral Sb_2Te_3 with a preferred orientation toward (110) with the highest conductivity of 1.82 x 10^3 S/cm.

4.6 References

[1] R.Venkatasubramanian, E. Siivola, T. Colpitts, B. O'Quinn, *Thin-film thermoelectric devices with high room-temperature figures of merit.* Nature, 2001. **413**(6856): p. 597-602.

[2] M. S. Dresselhaus, G. Dresselhaus, X. Sun, Z. Zhang, S. B. Cronin, T. Koga, *Low-dimensional thermoelectric materials.* Physics of the Solid State, 1999. **41**(5): p. 679-682.

[3] K. F. Hsu, S. Loo, F. Guo, W. Chen, J. S. Dyck, C. Uher, T. Hogan, E. K. Polychroniadis, M. G. Kanatzidis, *Cubic AgPbmSbTe2+m: Bulk Thermoelectric Materials with High Figure of Merit.* Science, 2004. **303**(5659): p. 818-821.

[4] T. Matsunaga, J. Akola, S. Kohara, T. Honma, K. Kobayashi, E. Ikenaga, R. O. Jones, N. Yamada, M. Takata, R. Kojima, *From local structure to nanosecond recrystallization dynamics in AgInSbTe phase-change materials.* Nat Mater, 2011. **10**(2): p. 129-134.

[5] H. Zhang, C.-X. Liu, X.-L. Qi, X. Dai, Z. Fang,; S.-C. Zhang, *Topological insulators in Bi2Se3, Bi2Te3 and Sb2Te3 with a single Dirac cone on the surface.* Nat Phys, 2009. **5**(6): p. 438-442.

[6] Rowe, D.M., *CRC Handbook of thermoelectrics.* CRC Press, 1995.

[7] L.M. Goncalves, C.C. P.Alpuim, D.M. Rowe, J.H. Correia, *Thermoelectric Properties of Bi2Te3 / Sb2Te3 Thin Films.* Materials Science Fórum, 2006. **514-516**: p. 156-160.

[8] H. Zou, D.M. Rowe, and S.G.K. Williams, *Peltier effect in a co-evaporated Sb2Te3(P)-Bi2Te3(N) thin film thermocouple.* Thin Solid Films, 2002. **408**(1–2): p. 270-274.

[9] M. Winkler, X. Liu, J. D. Konig, S. Buller, U. Schurmann, L. Kienle, W. Bensch, H. Bottner, *Electrical and structural properties of Bi2Te3 and Sb2Te3 thin films grown by the nanoalloying method with different deposition patterns and compositions.* Journal of Materials Chemistry, 2012. **22**(22): p. 11323-11334.

[10] N. Peranio, M. Winkler, Z. Aabdin, J. König, H. Böttner, O. Eibl, *Room temperature MBE deposition of Bi2Te3 and Sb2Te3 thin films with low charge carrier densities.* physica status solidi (a), 2012. **209**(2): p. 289-293.

[11] B. Fang, Z. Zeng, X. Yan, Z. Hu, *Effects of annealing on thermoelectric properties of Sb2Te3 thin films prepared by radio frequency magnetron sputtering.* Journal of Materials Science: Materials in Electronics, 2013. **24**(4): p. 1105-1111.

[12] Z.-H. Zheng, P. Fan, J.-T. Luo, G.-X. Liang, D.-P. Zhang, *Enhanced Thermoelectric Properties of Antimony Telluride Thin Films with Preferred Orientation Prepared by Sputtering a Fan-Shaped Binary Composite Target.* Journal of Electronic Materials, 2013. **42**(12): p. 3421-3425.

[13] A. Giani, A. Boulouz, F. Pascal-Delannoy, A. Foucaran, E. Charles, A. Boyer, *Growth of Bi2Te3 and Sb2Te3 thin films by MOCVD.* Materials Science and Engineering: B, 1999. **64**(1): p. 19-24.

[14] S. Zastrow, J. Gooth, T. Boehnert, S. Heiderich, W. Toellner, S. Heimann, S. Schulz, K. Nielsch, *Thermoelectric transport and Hall measurements of low defect Sb2Te3 thin films grown by atomic layer deposition.* Semiconductor Science and Technology, 2013. **28**(3): p. 035010.

[15] D.-K. Ko , Y. Kang, and C.B. Murray, *Enhanced Thermopower via Carrier Energy Filtering in Solution-Processable Pt–Sb2Te3 Nanocomposites.* Nano Letters, 2011. **11**(7): p. 2841-2844.

[16] Y. Zhang, M. L. Snedaker, C. S. Birkel, S. Mubeen, X. Ji, Y. Shi, D. Liu, X. Liu, M. Moskovits, G. D. Stucky, *Silver-Based Intermetallic Heterostructures in Sb2Te3 Thick Films with Enhanced Thermoelectric Power Factors.* Nano Letters, 2012. **12**(2): p. 1075-1080.

[17] C. Schumacher, K. G. Reinsberg, L. Akinsinde, S. Zastrow, S. Heiderich, W. Toellner, G. Rampelberg, C. Detavernier, J. A. C. Broekaert, K. Nielsch, J. Bachmann, *Optimization of Electrodeposited p-Doped Sb2Te3 Thermoelectric*

Films by Millisecond Potentiostatic Pulses. Advanced Energy Materials, 2012. **2**(3): p. 345-352.

[18] J. L. Lensch-Falk, D. Banga, P. E. Hopkins, D. B. Robinson, V. Stavila, P. A. Sharma, D. L. Medlin, Electrodeposition and characterization of nano-crystalline antimony telluride thin films. Thin Solid Films, 2012. 520(19): p. 6109-6117.

[19] I.V. Gasenkova, and T.E. Svechnikova, *Structural and Transport Properties of Sn-Doped Bi2Te3 – x Se x Single Crystals.* Inorganic Materials, 2004. **40**(6): p. 570-575.

[20] I. V. Gasenkova, M. K. Zhitinskaya, S. A. Nemov, T. E. Svechnikova, *Electron density redistribution in Sn-doped Bi2Te3.* Physics of the Solid State, 1999. **41**(11): p. 1805-1808.

[21] J.D. Sugar, and D.L. Medlin, *Precipitation of Ag2Te in the thermoelectric material AgSbTe2.* Journal of Alloys and Compounds, 2009. **478**(1–2): p. 75-82.

[22] J. Horák, P. Lošťák, L. Šiška, M. Stordeur, *The nature of silver impurity atoms in antimony telluride.* physica status solidi (b), 1982. **114**(1): p. 39-45.

[23] J. Horák, L. Koudelka, and J. Klikorka, *Antisite defects in narrow-gap layered chalcogenides of A2VB3VI type.* Reactivity of Solids, 1988. **5**(4): p. 351-359.

[24] R. J. Mehta, Y. Zhang, H. Zhu, D. S. Parker, M. Belley, D. J. Singh, R. Ramprasad, T. Borca-Tasciuc, G. Ramanath, *Seebeck and Figure of Merit Enhancement in Nanostructured Antimony Telluride by Antisite Defect Suppression through Sulfur Doping.* Nano Letters, 2012. **12**(9): p. 4523-4529.

[25] H. Jung, and N.V. Myung, *Electrodeposition of antimony telluride thin films from acidic nitrate-tartrate baths.* Electrochimica Acta, 2011. **56**(16): p. 5611-5615.

[26] I.-J. Yoo, Y. Song, D.C. Lim, N. V. Myung, K. H. Lee, M. Oh, D. Lee, Y. D. Kim, S. Kim, Y.-H. Choa, J. Y. Lee, K. H. Lee, J.-H. Lim, *Thermoelectric characteristics of Sb2Te3 thin films formed via surfactant-assisted electrodeposition.* Journal of Materials Chemistry A, 2013. **1**(17): p. 5430-5435.

[27] Ghosh, G., *The Sb-Te (antimony-tellurium) system.* Journal of Phase Equilibria, 1994. **15**(3): p. 349-360.

[28] K. Kifune, Y. Kubota, T. Matsunaga, N. Yamada, *Extremely long period-stacking structure in the Sb-Te binary system.* Acta Crystallographica Section B, 2005. **61**(5): p. 492-497.

[29] K. Govaerts, M. Sluiter, B. Partoens, D. Lamoen, Stability of Sb-Te layered structures: First-principles study, Physical Review B, 2012. **85**(14): p. 144114.

[30] M. Saleemi, A. Ruditskiy, M. S. Toprak, M. Stingaciu, M. Johnsson, I. Kretzschmar, A. Jacquot, M. Jägle, M. Muhammed, *Evaluation of the Structure and Transport Properties of Nanostructured Antimony Telluride (Sb2Te3).* Journal of Electronic Materials, 2014. **43**(6): p. 1927-1932.

[31] M.-J. Shin, D.-J.C., M.-J. Kang, S.-Y. Choi, *Chemical Bonding Characteristics of $Ge_2Sb_2Te_5$ for Thin Films.* Journal of the Korean Physical Society, 2004. **44**(1): p. 10~13.

[32] Zhou, W., et al., *Preparation and thermoelectric properties of sulfur doped Ag2Te nanoparticles via solvothermal methods.* Nanoscale, 2012. **4**(13): p. 3926-3931.

[33] J. Horlk, P.L., M. Matyas, *Point Defects in Sn-Doped SbsTes Single Crystds.* phys. stat. sol., 1985. **129**(381).

[34] M.-Y. Kim, and T.-S. Oh, *Electrodeposition and Thermoelectric Characteristics of Bi2Te3 and Sb2Te3 Films for Thermopile Sensor Applications.* Journal of Electronic Materials, 2009. **38**(7): p. 1176-1181.

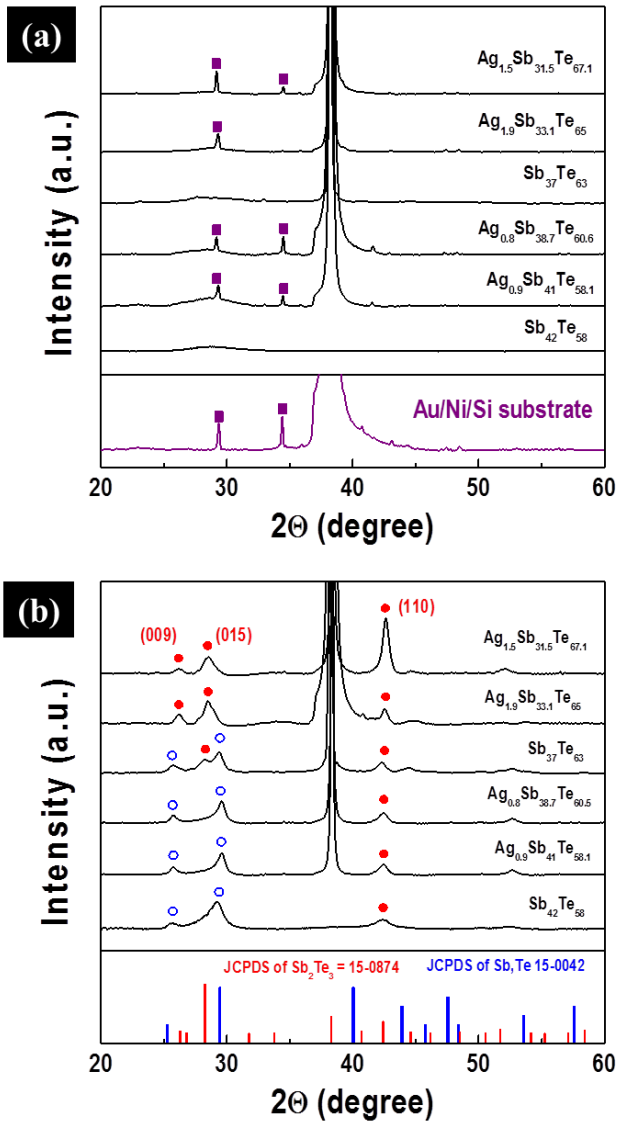

Figure 4.1 XRD analysis of $Sb_{37}Te_{63}$, $Sb_{42}Te_{58}$, $Ag_{1.5}Sb_{31.5}Te_{67.1}$, $Ag_{1.9}Sb_{33.1}Te_{65}$, $Ag_{0.8}Sb_{38.7}Te_{60.5}$, and $Ag_{0.9}Sb_{41}Te_{58.1}$ thin films as-deposited (a) and after annealing at 100 ^{o}C for 30 min (b). Symbol of solid square refers to substrate (Au/Ni/Si) peaks, solid circle refers to Sb_2Te_3 JCPDS 15-0874, symbol of empty circle refers to γ-SbTe JCPDS 15-0042.

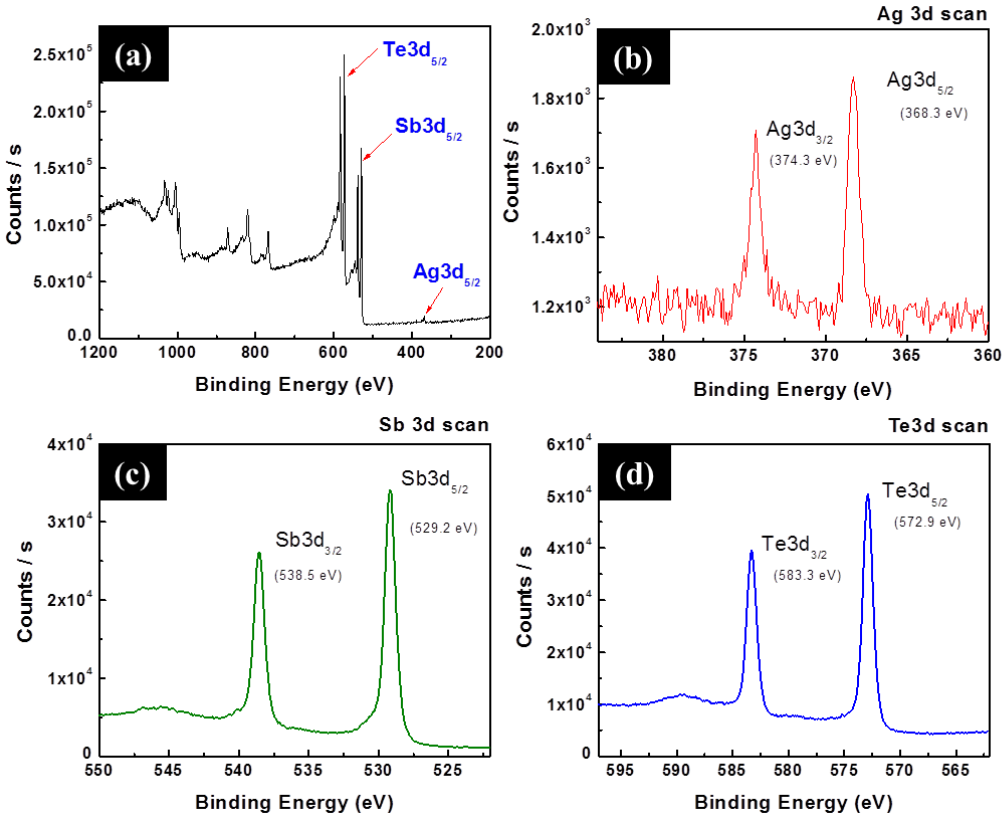

Figure 4.2 Binding states of $Ag_{1.9}Sb_{33.1}Te_{65}$ thin film confirmed by XPS analysis: wide range XPS spectra (a), and expanded scan of Ag 3d (b), Sb 3d (c), and Te 3d (d) of the film. The analysis was conducted at room temperature after annealing at 100 ^{o}C for 30 min.

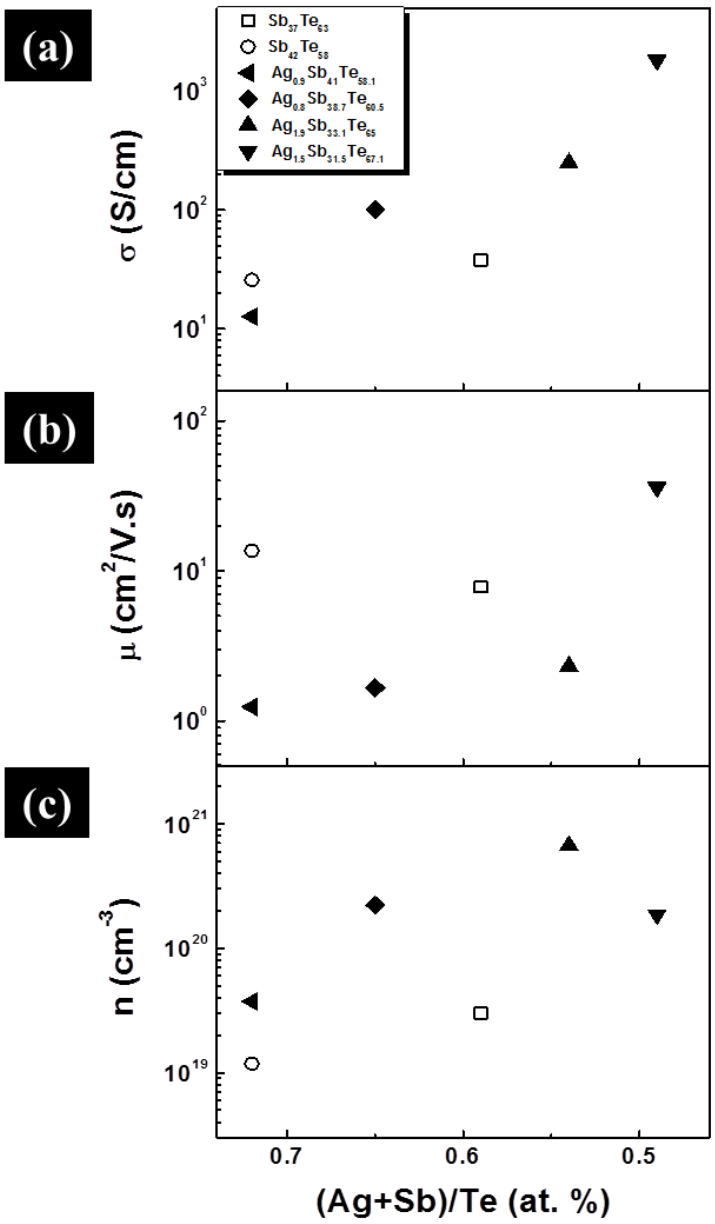

Figure 4.3 Electrical conductivity (a), Hall mobility (b), and carrier concentration (c) of undoped and Ag-doped Sb_xTe_y thin films as a function of Ag/Sb ratio. The measurement was conducted at room temperature after annealing at 100 ^oC for 30 min.

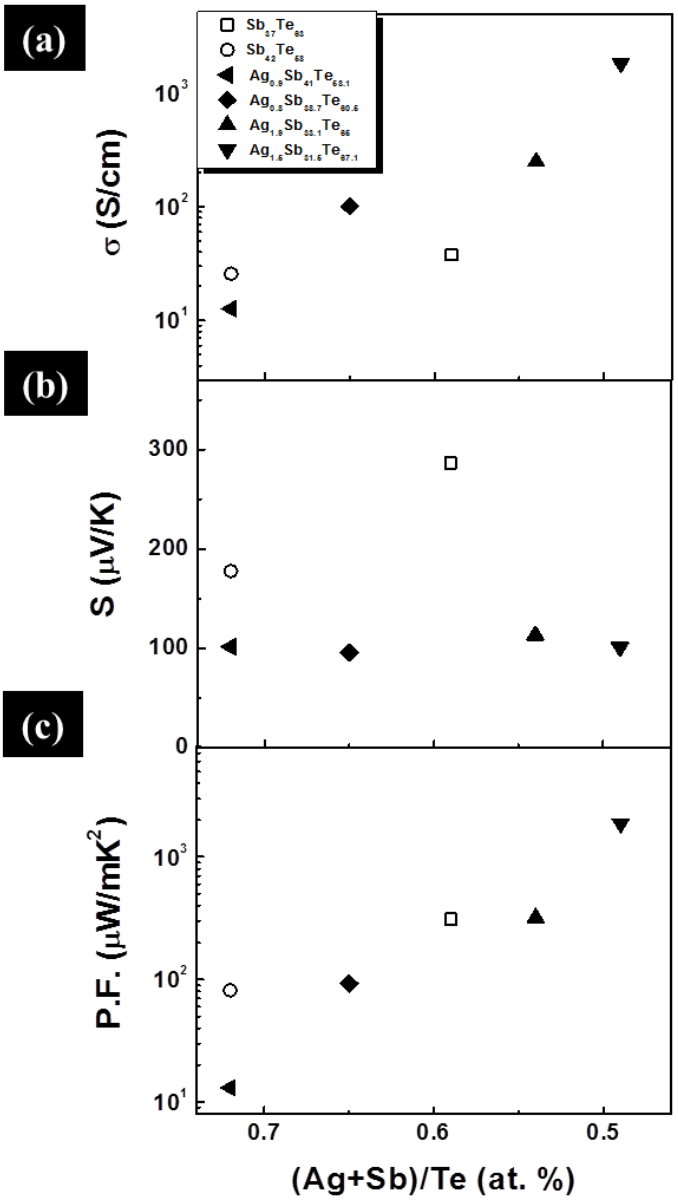

Figure 4.4 Thermoelectric properties of undoped and Ag-doped Sb_xTe_y thin films as a function of (Ag+Sb)/Te ratio in the films. The measurement was conducted at room temperature after annealing at 100 ^oC for 30 min.

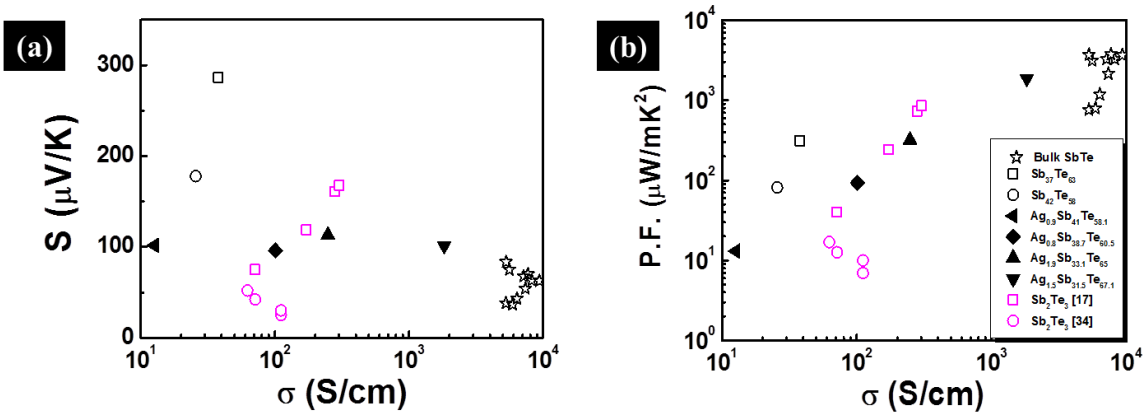

Figure 4.5 Seebeck coefficient (a) and power factor (b) of $Sb_{37}Te_{63}$, $Sb_{42}Te_{58}$, $Ag_{1.5}Sb_{31.5}Te_{67.1}$, $Ag_{1.9}Sb_{33.1}Te_{65}$, $Ag_{0.8}Sb_{38.7}Te_{60.5}$, and $Ag_{0.9}Sb_{41}Te_{58.1}$ thin films after annealing at 100 ^{o}C for 30 min. The values from the bulk single crystal SbxTey (symbol of empty star) and reported results from electrodeposited Sb_2Te_3 thin films (symbol of empty circle and square) are also included for comparison.

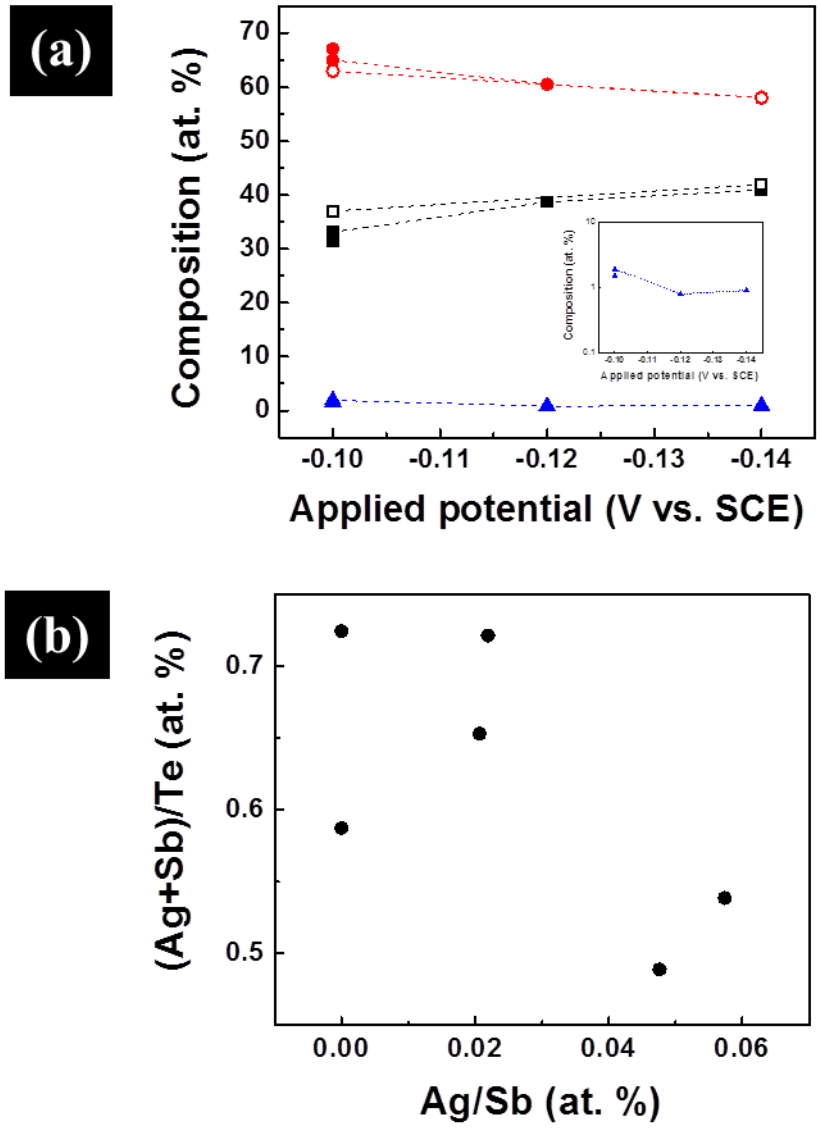

Figure 4.6 Composition of Ag-doped Sb_xTe_y thin films as a function of applied potentials and electrolyte concentrations (a). The electrolyte consisted of 2.4 $HTeO_2^+$, 3.6 $[Sb(C_4H_2O_6)_2]^{-2}$, 33 mM $C_4H_6O_6$, 1M HNO_3 (empty symbol), and 100 µm Ag^+ (solid symbol). Ratio of (Ag+Sb)/Te at. % as a function of Ag/Sb at. % (b).

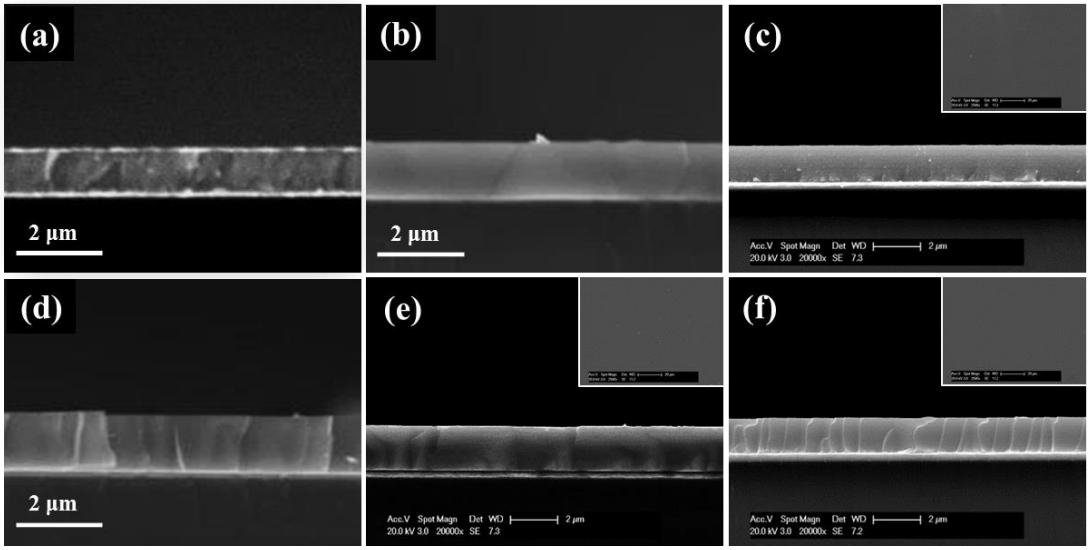

Figure 4.7 Morphology of (a)$Sb_{37}Te_{63}$, (b)$Sb_{42}Te_{58}$, (c)$Ag_{1.5}Sb_{31.5}Te_{67.1}$, (d)$Ag_{1.9}Sb_{33.1}Te_{65}$, (e)$Ag_{0.8}Sb_{38.7}Te_{60.5}$, and (f)$Ag_{0.9}Sb_{41}Te_{58.1}$ thin films confirmed by SEM analysis showing cross-section views. Inset images are top view of the thin films.

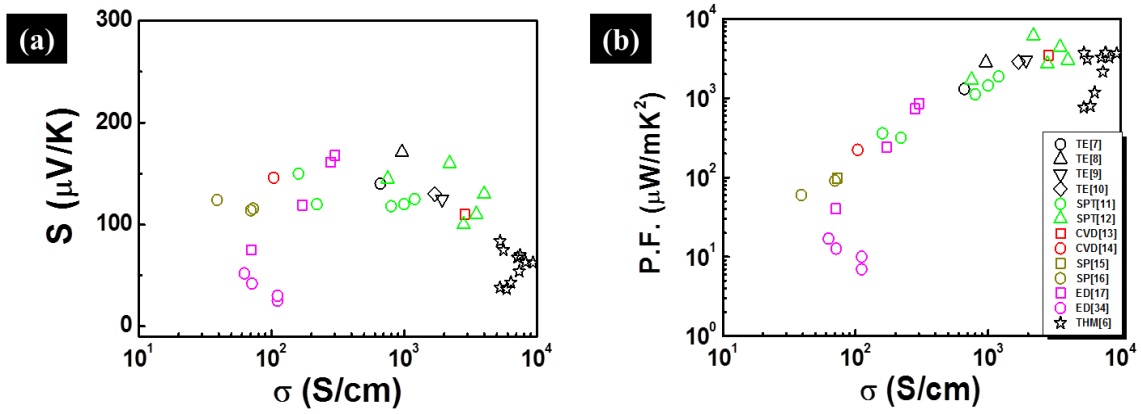

Figure 4.8 Seebeck coefficient (a) and power factor (b) of Sb_2Te_3 thin films as a function of electrical conductivity. The various synthesis techniques such as thermal evaporation (TE), sputtering deposition (SPT), chemical vapor deposition (CVD), solution phase reaction (SP), and electrodeposition (ED)[34] was utilized to fabricate Sb_2Te_3 thin films.

CHAPTER 5 Optimizing Thermoelectric Property of Antimony Telluride Nanowires by Tailoring Composition and Crystallinity

5.1 Abstract

In this work, an effect of the composition and microstructure changes on the electrical and thermoelectric properties of antimony telluride (Sb_xTe_y) nanowires was investigated to determine the optimum conditions that give the highest thermopower. For a systematical study, a facile template-directed electrodeposition technique was utilized to prepare amorphous Sb_xTe_y nanowires with well-controlled dimension and composition. Composition-dependent phase transition behavior of the nanowires, corresponding to the amorphous-to-crystalline solid state transition, was investigated by measuring their electrical resistivity changes where the electrical resistivity variation ratio ($\Delta\rho/\rho_0 = (\rho-\rho_0)/\rho_0$) was highly dependent on the Sb content. Temperature-dependent electrical properties (electrical resistivity, thermal activation energy (E_a), and field effect transistor (FET) mobility) of the amorphous and crystalline nanowires were also characterized before/after the phase transition. Material properties of the nanowires such as crystallinity, grain size, and phase segregation as a function of the Sb content were tailored by a post-annealing process. The tailored material properties successfully altered the electrical and thermoelectric properties of the nanowires. The highest thermopower of 318 μV/K at the carrier concentration of 1.1 x 10^{19} cm^{-3} was observed in the Te segregated Sb_2Te_3 (*i.e.*, $Sb_{32}Te_{68}$) nanowires.

5.2 Introduction

Antimony telluride (Sb_2Te_3), which is a narrow band gap and layered structure (space group of *R-3m*) metal chalcogenide, has been vigorously investigated along with tailoring its material characteristics for diverse applications including thermoelectrics (TE), non-volatile phase change random access memory (PCRAM), and recently topological insulators (TI). Sb_2Te_3 has attracted attention as a p-type TE material because of its promising TE performance under room temperature operation and its high thermoelectric figure-of-merit ($zT=S^2\sigma T/\kappa$), where S is the Seebeck coefficient ($\mu V\ K^{-1}$), σ is the electrical conductivity ($\Omega^{-1}m^{-1}$), and κ is the thermal conductivity ($Wm^{-1}K^{-1}$).[1-5] The key to enhance zT in TE materials is to "decouple" the interdependency among σ, κ, and S, which has been approached by engineering its material properties. For example, structural modifications, such as nano-crystalline,[6] composites,[7,8] crystallographic orientation[9-11] based on the high anisotropic properties of Sb_2Te_3, and the reduction of self-compensating antisite defects[12,13] through chemistry have been shown to independently contribute to the enhancement of thermoelectric properties. Sb_2Te_3 and its related compounds (*e.g.*, GeSbTe alloy) are also of significance because they can exhibit a highly stable amorphous phase and, due to its growth-dominated crystallization mechanism, they exhibit an extremely rapid/reversible amorphous-crystalline phase transition which is key to phase change materials for PCRAM[7,14,15] applications. A more recent and notable advancement is the use of stoichiometric single-crystalline Sb_2Te_3 in the presence of heavy elements[16] producing a topological insulator. Its protected surface state due to the spin-orbit coupling effect may pave a way to create

quantum computing and spintronics.[17-19] Therefore, due to the strong interrelation between material and transport properties, it is critical to independently engineer each of them for maximum performance on the target applications.

One-dimensional (1-D) Sb_2Te_3 nanowires have improved performance levels in both TE and PCRAM applications. Enhancements in thermopower were achieved by reducing the diameter of the nanowires,[18,20] and a PCRAM's power requirements were reduced while increasing reading, writing and erasing speeds based on reduced phase transition area.[14,21] Various methods have been applied to synthesize 1-D Sb_2Te_3 nanowires, including hydrothermal synthesis,[22] vapor-liquid-solid growth,[14] colloidal techniques,[23] and solvothermal technique.[24] In spite of their ability to control the dimensions and morphology of the deposited nanostructures, these techniques still lack control over the nanowires' final crystallinity, crystal structure, and defect levels, which are significant factors governing their properties.

A template-directed electrodeposition technique resolves these underlying issues while retaining tight controls over dimensions and morphology of the final nanostructures.[25,26] It is also known as a facile process because the nanostructure composition is tailored by simply varying the applied potential or easily doped by adding foreign elements into the electrolyte.[27,28] Moreover, configuring vertically grown nanowire arrays on a conductive seed layer can facilitate the characterization of electrical and thermoelectric properties without using complicated fabrication methods to form external leads. For example, experimenters measuring the Seebeck coefficient,[29] electrical properties,[29] and the thermal conductivity[30,31] on nanowires synthesized

from arrays embedded in AAO templates obtained comparable results on nanowires synthesize individually.

Even though there are a large number of studies focused on the characterizations of thermoelectric properties and solid-state memory switching behavior on 1-D nanostructured Sb_2Te_3, there is no systematic study on the Sb_xTe_y material system or its transport properties as a function of composition and crystallinity. To achieve the best thermoelectric performance, it is imperative to decouple the three main properties σ, κ, and S by establishing correlations among carrier conductivity, mobility, and concentration in relation to material composition, structural defects, crystallinity, and phase.

This paper presents the results of a study using the facile template-directed electrodeposition method to deposit amorphous Sb_xTe_y nanowires of various compositions by controlling the electrochemical parameters. The aim of the study was to obtain the highest thermopower and correlate this result with composition and final microstructure. The composition tailored Sb_xTe_y nanowires were synthesized in arrays embedded in AAO templates, and their Seebeck coefficient and carrier concentration were characterized and contrasted in terms of the Mott-relation. In addition, the effect of Sb content on the crystallization of the electrodeposited nanowires, corresponding to the post annealed amorphous-to-crystalline solid state phase transformation, was investigated by correlating electrical resistivity changes with respect to transport properties, such as the temperature-dependent resistivity, activation energy (E_a), and FET-mobility.

5.3 Experimental Section

Sb_xTe_y nanowires were potentiostatically electrodeposited using anodized aluminum oxide templates (AAO, nominal pore size of 250 nm, Whatman Inc.) in the absence of agitation. To form a working electrode, one side of the AAO template was sputtered with gold to serve as a seed layer. A Pt coated titanium and a saturated calomel electrode (SCE) were used as the counter and the reference electrode, respectively. An electrolyte was prepared by separately dissolving TeO_2 in concentrated HNO_3 and Sb_2O_3 in L-tartaric acid solutions at 50 ^oC. Once the oxides were completely dissolved, two solutions were mixed together and deionized water was added to reach final volume. The final concentrations of the prepared electrolytes were 10 mM $HTeO_2^+$, 0.5 M L-tartaric acid, and 1 M HNO_3. The concentration of $[Sb_2(C_4H_2O_6)_2]^{2-}$ in the electrolyte was varied 10 and 20 mM to achieve Sb_xTe_y nanowires with controlled Sb composition and crystallinity. The electrodeposition was carried out by ranging the applied potential from -0.1 V to -0.3 V vs. saturated calomel electrode (SCE) using a potentiostat (VMP2, Princeton Applied Research) at room temperature. After deposition, the AAO template was chemically dissolved in 1 M NaOH at room temperature for 5 hours to disperse nanowires. The suspended Sb_xTe_y nanowires were centrifuged and rinsed by D.I. water twice followed by dispersion in isopropyl alcohol (IPA).

The composition of synthesized Sb_xTe_y nanowires was analyzed by energy dispersive X-ray spectroscopy (EDS) (model IncaX-Sight, Oxford Instrument Inc.). Scanning electron microscopy (SEM) (model XLG-30FEG, Philips, Inc.) was employed to determine diameter and surface morphology of the nanowires. The crystallinity was

investigated using X-ray diffraction (XRD) (Empyrean, PANalytical) and selected area diffraction pattern (SAED) during the TEM analysis (TEM) (model JEM-2100F, JEOL).

Various measurement techniques were used to characterize the electrical and thermoelectric properties of the nanowires. A Mott-Shottky (M-S) analysis was performed on nanowires embedded in the AAO templates to measure their carrier concentration. The measurement configuration is illustrated in Figure 5.7. Impedance measurements were performed using a VMP3-Modular 16 Channels Potentiostat/ Galvanostat/ EIS (Biologic Instrument). The electrolyte composition for M-S analysis was a perchlorate solution consisted of 0.1 M $NaClO_4$ + 0.1 M $HClO_4$, the applied frequency was fixed to 50 kHz, and the amplitude of the ac signal was 10 mV.

The Seebeck coefficient ($S = \Delta V/\Delta T$) was obtained by a custom-made Seebeck voltage measurement system that provides a programmable fixed temperature gradient across the sample (Figure 5.8). The amorphous-to-crystalline solid state phase transition was monitored by changes in electrical resistivity of single nanowire correlate to its microstructure. Specifically, dispersed nanowires were drop-casted onto a highly doped Si (p-type) wafer. The wafer was epitaxially grown SiO_2 (300 nm), followed by patterning a photoresist layer with a 3 µm gap made by using a lithographical procedure. To minimize the effect of a native oxide layer on the nanowire surface, which might obstruct the formation of an ohmic contact between a nanowire and micro-fabricated electrode, a galvanic displacement reaction (GDR) method was introduced in the device fabrication process.[32] Electrical properties of the Sb_xTe_y nanowires were characterized

using a source-measure unit (model 2610A, Keithley) with a coldfinger cryogenic system (model CCS-350SH, Janis) by varying the temperature from 380 K to 100 K.

5.4 Results and Discussion

5.4.1 Synthesis and Material Characterization of Sb_xTe_y Nanowires

Sb_xTe_y nanowires were potentiostatically electrodeposited in the AAO templates with an average pore diameter of ~250 nm. The composition of the nanowires was controlled by varying the applied potential and concentration of $[Sb_2(C_4H_2O_6)_2]^{2-}$ in the electrolyte (Figure 5.8). It revealed that the Sb content increased monotonically as the applied potential decreased from -0.2 V to -0.3 V (vs. SCE). In addition, at fixed applied potential, as the $[Sb_2(C_4H_2O_6)_2]^{2-}$ concentration increased in the electrolyte the deposited Sb content greatly increased in the nanowires. The effect of applied potential and electrolyte concentration on the composition of the Sb_xTe_y thin films[33] and nanoribbons[34] were studied in our previous works. These works showed that the Sb content increased as the applied potential decreased because of the overpotential deposition of the Sb in addition to the underpotential deposition of the Sb_2Te_3.[33]

Changes in the microstructure as a result of crystallizing the as-deposited amorphous Sb_xTe_y nanowires by various post thermal treatments were investigated by TEM. Figure 5.1a-d show the TEM results of the amorphous phase and thermally-cycled Te-rich Sb_2Te_3 (*i.e.,* $Sb_{37}T_{63}$) nanowires. Rough surface morphology was indicated in both nanowires, which is partly caused by the shape of the templates. Selected-area electron

diffraction (SAED) (Figure 5.2b) of the as-deposited nanowire showed no clearly identified diffraction patterns, which is consistent with an amorphous phase. After the nanowires were exposed to the thermal cycle (300 K to 370K), however, the corresponding SAED patterns (Figure 5.2d) represented the lattice distances of 0.208 and 0.3 nm, which are attributed to the formation of a rhombohedral phase Sb_2Te_3 with crystal orientations in the (1 1 0) and (0 1 5) directions, respectively. The XRD results on $Sb_{37}T_{63}$ nanowires embedded in the AAO template showed similar results; namely, no peaks, indicating amorphous phase, for as-deposited films (Figure 5.1e-A), but identifiable peaks in post annealed samples in forming gas (95 % N_2, 5 % H_2) at 100 ^oC and 200 ^oC, as shown in Figures 5.1e-B & C, respectively. The 100 ^oC annealed sample showed peaks identified with crystal orientations in the (0 1 5), (10 10), and (1 1 0) directions (symbol of solid circle refers to Sb_2Te_3 JCPDS 15-0874), which match well with the TEM results. The Scherrer equation was employed to convert the XRD peaks information assigned into the d-spacing value and grain size of the Sb_xTe_y nanowires (Figure 5.9). An average grain size of the $Sb_{37}T_{63}$ nanowires was calculated to be ~ 23 nm with the d-spacing of 2.13 Å. The sample annealed at 200 ^oC showed an increase in grain size to ~28 nm and a d-spacing of 2.13 Å, which is well aligned with the reference value of the d-spacing of (1 1 0) direction of stoichiometric Sb_2Te_3 (JCPDS 15-0874), and indicating that the crystallinity of the material was improved. Interestingly, Te phase segregation (symbol of empty circle refers to Te JCPDS 36-1452) was also observed under these annealing conditions, meaning that the $Sb_{37}T_{63}$ nanowires contained two-mixed phases of tetragonal Te embedded in rhombohedral Sb_2Te_3 matrix.

XRD characterization of the composition dependent Sb_xTe_y nanowires was also assessed as a function of annealing temperature (Figure 5.9) to investigate the phase transition behavior not only in the stoichiometric intermetallic compound, but also in the wide range of Sb content nanowires ranging from 32 to 58 at. %. As shown in Figure 5.9 (a-d), independent of the Sb content, all as-deposited films show no peaks and are thus considered to be amorphous. After annealing, however, clearly defined peaks are visible indicating that the crystallinity of all samples was significantly improved. In addition, the $Sb_{32}Te_{68}$ nanowires also represented Te segregation after annealing at 100 ^{o}C and 200 ^{o}C (Figure 5.S9a). This is because the excess Te tends to precipitate out during the solid-state structural transformation.[35] The changes in grain size, d-spacing, and preferred orientation of the nanowires as a function of annealing temperature and Sb content were plotted in Figure 5.10. Shown in Figure 5.10a, as the Sb content increased the d-spacing values also slightly increased representing the gradual shift of lattice parameters. This could be explained by the existence of Sb_{Te} anti-site defects dominant in this system.[36] Moreover, it is also expected from the Sb-Te phase diagrams[37] that the Sb_2Te_3 phase has a very small portion in the entire system which suggests that some residue amorphous SbTe alloy or other crystalline phase, such as Sb, Sb-rich γ and δ phase, or Te phase may be present after the annealing.[38] The grain size of all nanowires increased as the annealing temperature increased. However, there was no clear trend on the grain size and preferred orientation change depending on the Sb content in the nanowires.

5.4.2 Electrical and Thermoelectric Properties of Sb_xTe_y Nanowires

Composition- and temperature-dependent electrical properties of single Sb_xTe_y nanowires were investigated in the temperature range from 380 to 100 K in vacuum. The electrical properties of a single nanowire were characterized using a two-terminal configuration by creating electrical contacts to the nanowires using a microfabrication technique. As a back-gated electrode, Si substrate was utilized. An inset in Figure 5.2a represents an optical image of an aligned single nanowire with Pt contacts. Temperature-dependent I-V curves (Figure 5.2a) on a single $Sb_{36}Te_{64}$ nanowire showed clean linear behavior indicating that an ohmic contact was successfully achieved by the GDR process described in the experimental section.[32] For the field effect transistor (FET) characteristics, the gate voltage was swept from -10 to +10 V at a fixed drain-source voltage of +0.5 V. Typical back-gated I_{DS}-V_G curves (Figure 5.2b), which I_{DS} continuously decreased as V_G increased, indicated that the electrodeposited $Sb_{36}Te_{64}$ nanowire is a p-type semiconductor. Moreover, FET hole mobility was determined by the measurement of transconductance (dI/dV_G) using Equation[32]:

$$\mu = \frac{dI}{dV_G}\left(\frac{L^2}{CV_{DS}}\right) \qquad \text{Equation 5.1}$$

where, C is the capacitance, and L is the length of the nanowire. The temperature-dependent electrical resistivity and FET-mobility of a $Sb_{36}Te_{64}$ (Figure 5.3a-c) and a $Sb_{53}Te_{47}$ (Figure 5.3d-f) nanowires were investigated in Figure 5.3. The sequence of the measurements were discretely designed in the attempt to observe the transport properties of both amorphous and nano-crystalline phased Sb_xTe_y nanowire and, by extension,

phase transition properties as a function of composition. In addition, activation energy (amorphous, E_{a0} and nano-crystalline, E_a) of the nanowires was calculated from Arrhenius Equation:

$$R = R_0 exp\left(-\frac{E_a}{2kT}\right) \quad \text{Equation 5.2}$$

where R_0 is the resistance at T=∞, E_a is the thermal activation energy for electrical conduction, *k* is the Boltzmann constant, and T is the temperature. First, the electrical resistivity as a function of temperature (300 - 100 K) was investigated in the amorphous nanowires. The resistivity of the amorphous $Sb_{36}Te_{64}$ and $Sb_{53}Te_{47}$ nanowire increased as the temperature decreased, which is a typical semiconductor behavior. As reported earlier, it is acknowledged that the transport property of crystalline Sb_2Te_3 is metal-like behavior and highly dependent on its mobility.[18] Therefore, it is important to manifest the structural properties such as crystallinity or stoichiometry of the studied materials to precisely interrelate the charge transports behaviors. The electrical resistivity changes of the nanowires in the low temperature region are analogous to the amorphous Sb_2Te_3 thin films that the transport property of the amorphous Sb_xTe_y nanowires follows the hopping mechanism.[39-41] Relatively small FET-mobility values and E_{a0} (= 0.144 eV of amorphous $Sb_{36}Te_{64}$ and 0.158 eV of amorphous $Sb_{53}Te_{47}$) also supported that the glassy-like crystal structure definitely reduced the mobility of the nanowires and led to significantly low electrical conductivity. As a second step of the measurements, the electrical properties were characterized along both ascending and decreasing temperature range, referred to (B) in Figure 3(a). During this thermal cycle, the electrical resistivity of

both nanowires reduced of approx. one order of magnitude because of the phase transition from amorphous to nano-crystalline phase, which was also confirmed by the TEM (Figure 5.1a-b). Furthermore, as a result of the improved crystallinity without reversible change, the enhanced FET-mobility and reduced E_a (= 0.06 eV of nano-crystalline $Sb_{36}Te_{64}$ and 0.09 eV of nano-crystalline $Sb_{53}Te_{47}$) were investigated in the low temperature TCR measurement. This result agrees well with the thermal activation energy of ~0.06 eV in crystalline Sb_2Te_3 thin film reported by V. D. Das *et al*.[40] The larger E_a indicated from the amorphous phase compared to the nano-crystalline phase may be assigned from the large concentration of localized states.[39] Yet, the lower FET-mobility of the $Sb_{53}Te_{47}$ nanowire compared to $Sb_{36}Te_{64}$ nanowire after the same thermal cycle represents the larger effect of charge carrier scattering originated from the excess Sb element. The temperature dependent FET-mobility of the nanowires is plotted in Figure 5.3c and f. As the temperature decreased, the measured FET-mobility of both nanowires before and after thermal cycle decreased. This indicated that the amorphous and nanocrystalline Sb_xTe_y nanowires conformed the ionized impurity dominated scattering.[42]

The composition-dependent electrical resistivity of Sb_xTe_y nanowires before (open circle) and after thermal-cycle (solid circle) were shown in Figure 5.4. The composition of the tailored Sb content was ranged from 36 to 53 at. %. As the Sb content increased the resistivity of the nanowires increased, which is explained by major anti-site defects caused by the existence of Sb atoms on Te lattice sites. Due to this native anti-site defects dominant properties, it is known that the electrical transports of the Sb_xTe_y is highly

determined by their composition,[34] which agrees well with our results in the nanowires. An inset represents electrical resistivity variation ratio ($\Delta\rho/\rho_0 = (\rho - \rho_0)/\rho_0$) as a function of Sb content. The higher ratio of resistivity variations were achieved as the Sb content increased in the nanowires. It is known that $Sb_{70}Te_{30}$ solid solution is a valid phase for phase change memory (PCM) device applications among the entire composition available in the Sb-Te binary system owing to its fast transition speed and low transition temperature, in addition, the difference in the crystallization temperature as a function of the Sb content.[43] This composition-dependent phase transition behavior was also observed in this nanowires study, promising for high performance PCM applications.

The effects of composition and annealing temperature on carrier concentration and Seebeck coefficient of Sb_xTe_y nanowires were investigated in room temperature (Figure 5.5). The Sb_xTe_y nanowire arrays embedded in the AAO templates were directly utilized to characterize the carrier concentration by Mott-Schottky (M-S) analysis and the Seebeck coefficient. From the linear fit of $1/C^2$ vs. V in the M-S plots according to equation:

$$\frac{1}{C^2} = \frac{2}{\varepsilon_o \varepsilon_r e N_A}\left(V - V_{fb} - \frac{k_B T}{e}\right) \qquad \text{Equation 5.3}$$

where C is the space-charge capacitance of the semiconductor, ε_o is the permittivity in vacuum, ε_r is the dielectric constant (ε_r of the antimony telluride was taken as 51[44]), V is the applied potential and T is the temperature, a sign of slopes confirms the carrier-type of the semiconductor.[45-47] Figure 5.11 represents the applied potential-dependent capacitance changes of the Sb_xTe_y nanowire arrays. The negative sign of slopes indicates

that as-deposited Sb_xTe_y nanowire arrays show a p-type semiconducting behavior, which is analogous to the result from a single-nanowire characterization by FET measurement as well. The change of the carrier concentration of the Sb_xTe_y nanowires as a function of the annealing temperature was shown in the Figure 5.5a. The values from the as-deposited nanowires with amorphous phases were in the range of 10^{18}-10^{19} cm^{-3}, followed by the increase of one- or two-orders of magnitude after annealed at 100 ^oC. After annealed at 200 ^oC, however, the carrier concentration of the nanowires, except for the one that had Sb content of 50 at.%, were reduced as less as ten-fold or much more. The increased carrier concentrations after annealed at 100 ^oC might be due to the generation of defects in the nanowires, which confirmed by the fairly contrast TEM image in the nanowire (Figure 5.1c) compared to the as-deposited nanowires (Figure 5.1a). Moreover, the slight mismatch of the d-spacing values from the nanowires annealed at 100 ^oC with the reference value, also confirmed that non-uniform phases existed in the nanowires (Figure 5.9a). On the other hand, the decrease of the carrier concentration in the nanowires after further annealed at 200 ^oC is believed owing to the results of reduction of the native defects and expansion in the grain sizes anticipated after the sufficient annealing process.[13] The increased grain size (Figure 5.9b) contributed to the decreased density of grain boundaries and defects, resulting in the reduction of the carrier concentration.

It is known that the major defects in the antimony telluride can alter the electrical and thermoelectric properties in the Sb_xTe_y nanostructures. The Seebeck coefficient of the composition-modulated Sb_xTe_y nanowires as a function of the annealing temperature

was described in Figure 5.5b as well. The positive Seebeck coefficient values also confirmed that the electrodeposited Sb_xTe_y nanowires are p-type characteristic. The values of the Seebeck coefficient from the as-deposited nanowires were varied within 59 ~ 215 μV/K, depending on the Sb content. Whereas slight reduction of the values were observed in the Te-rich nanowires after annealing at 100 ^oC, followed by a striking increment after 200 ^oC in the overall Sb_xTe_y nanowires. The highest value of the Seebeck coefficient was represented in the $Sb_{32}Te_{68}$ nanowires after annealed at 200 ^oC.

The changes of the Seebeck coefficient of the nanowires as a function of the annealing temperature can be attributed to the alternation of carrier concentration using Mott-relation given by:

$$S = \frac{8\pi^2 {k_B}^2}{3eh^2} m^* T \left(\frac{\pi}{3n}\right)^{2/3} \qquad \text{Equation 5.4}$$

where n is the carrier concentration, S is the Seebeck coefficient, k_B is the Boltzmann constant, h is the Planck constant, e is the electron charge, and m^* is the effective mass of the carrier. As for semiconductors obeying Boltzmann statistics, the Seebeck coefficient is found to be inversely proportional to the carrier concentration.[35] The relationship of these parameters in the electrodeposited nanowires is plotted in Figure 5.6. The Seebeck coefficient of annealed Sb_xTe_y nanowires at 100 ^oC was reduced compared to that of as-deposited nanowires due to their increased carrier concentration but still maintaining their linear relationships. Moreover, the increase in the Seebeck coefficient with reduced carrier concentration after further annealing is also in agreement with the Eq. 5.4. The Seebeck coefficient of the electrodeposited Sb_xTe_y nanowires with diversely tailored

structural properties was compared to the values of bulk single crystal Sb_xTe_y. The majority of the nanowires indicated the enhanced Seebeck values compared to the bulk Sb_xTe_y (~79 μV/K), which might be explained due to the increase in difference between the Fermi level and the average mobile carrier energy in the nanostructures.[12] It is emphasized that the $Sb_{32}Te_{68}$ nanowires, which indicated the highest Seebeck coefficient of 318 μV/K at the carrier concentration of 1.1 x 10^{19} cm^{-3} after annealed at 200 ^oC, represented the Te segregated phase in the XRD analysis (Figure 5.9a). A similar observation was reported in Sb_2Te_3 thin films showing that the films containing the Te nanodots showed the higher Seebeck coefficient (150 μV/K at carrier concentration of ~10^{19} cm^{-3}) than that of the films without Te nanodots (110 μV/K, ~10^{19} cm^{-3}).[35] The enhanced Seebeck coefficient may be attributed to the formation of a potential barrier at the Te-Sb_2Te_3 interfaces, which was confirmed by the increased effective mass of the carrier. Thus, the potential barriers might be also generated in the nanowires, leading to optimizing thermoelectric properties. Therefore, the tailor of the composition, crystallinity and their phases in the Sb_xTe_y nanowires can be the key to enhance the performance of the thermoelectric materials.

5.5 Conclusion

The template-directed electrodeposition was utilized to synthesize Sb_xTe_y nanowires where the composition of the nanowires was modulated by adjusting electrodeposition conditions. Material properties of the nanowires, such as crystallinity, grain size, and phase segregation as a function of the Sb content, were tailored by a post-annealing

process. The phase transition from amorphous to nanocrystalline phase was observed by XRD and TEM analysis. The tailored material properties successfully altered the electrical and thermoelectric properties of the nanowires. Composition-dependent phase transition behavior of the nanowires was investigated by measuring their resistivity changes where the resistivity variation ratio ($\Delta\rho/\rho_0$) was highly dependent on the Sb content in the nanowires. The carrier concentration of Sb_xTe_y nanowires decreased from ~10^{19} to ~10^{18} cm^{-3} as their grain size increased due to the reduced antisite defects. Temperature-dependent electrical properties of the amorphous and crystalline nanowires were also characterized before/after the phase transition. The highest thermopower of 318 μV/K at the carrier concentration of 1.1 x 10^{19} cm^{-3} was observed in the Te segregated $Sb_{32}Te_{68}$.

5.6 References

[1] Rowe, D.M., *CRC Handbook of thermoelectrics.* CRC Press, London, 1995.

[2] G.J. Snyder, and E.S. Toberer, *Complex thermoelectric materials.* Nat Mater, 2008. **7**(2): p. 105-114.

[3] R. Venkatasubramanian, E. Siivola, T. Colpitts, B. O'Quinn, *Thin-film thermoelectric devices with high room-temperature figures of merit.* Nature, 2001. **413**(6856): p. 597-602.

[4] X. Sun, Z. Zhang, and M.S. Dresselhaus, *Theoretical modeling of thermoelectricity in Bi nanowires.* Applied Physics Letters, 1999. **74**(26): p. 4005-4007.

[5] M.-G. Marisol, O.c.-C., P. Diaz-Chao, *Nanoengineering thermoelectrics for 21st century: Energy harvesting and other trends in the field.* Renewable and sustainable energy reviews, 2013. **24**: p. 288-305.

[6] K. F. Hsu, S. Loo, F. Guo, W. Chen, J. S. Dyck, C. Uher, T. Hogan, E. K. Polychroniadis, M. G. Kanatzidis, *Cubic AgPbmSbTe2+m: Bulk Thermoelectric Materials with High Figure of Merit.* Science, 2004. **303**(5659): p. 818-821.

[7] T. Matsunaga, J. Akola, S. Kohara, T. Honma, K. Kobayashi, E. Ikenaga, R. O. Jones, N. Yamada, M. Takata, R. Kojima, *From local structure to nanosecond recrystallization dynamics in AgInSbTe phase-change materials.* Nat Mater, 2011. **10**(2): p. 129-134.

[8] J. Kang, J. W. Roh, W. Shim, J. Ham, J.-S. Noh, W. Lee, , *Reduction of Lattice Thermal Conductivity in Single Bi-Te Core/Shell Nanowires with Rough Interface.* Advanced Materials, 2011. **23**(30): p. 3414-3419.

[9] X.Y. Wenzhong Wang, P. Bed, M. Yi, H. Qing, Y. Jian, C. Gang, R. Zhifeng, *Chemical Synthesis of Anisotropic Nanocrystalline Sb2Te3 and Low Thermal Conductivity of the Compacted Dense Bulk.* Journal of Nanoscience and Nanotechnology, 2008. **8**: p. 452-456.

[10] J. Chen, T. Sun, D. Sim, H. Peng, H. Wang, S. Fan, H. H. Hng, J. Ma, F. Y. C. Boey, S. Li, M. K. Samani, G. C. K. Chen, X. Chen, T. Wu, Q. Yan, *Sb2Te3*

Nanoparticles with Enhanced Seebeck Coefficient and Low Thermal Conductivity. Chemistry of Materials, 2010. **22**(10): p. 3086-3092.

[11] M. Saleemi, A. Ruditskiy, M. S. Toprak, M. Stingaciu, M. Johnsson, I. Kretzschmar, A. Jacquot, M. Jägle, M. Muhammed, *Evaluation of the Structure and Transport Properties of Nanostructured Antimony Telluride (Sb2Te3).* Journal of Electronic Materials, 2014. **43**(6): p. 1927-1932.

[12] R. J. Mehta, Y. Zhang, H. Zhu, D. S. Parker, M. Belley, D. J. Singh, R. Ramprasad, T. Borca-Tasciuc, G. Ramanath, *Seebeck and Figure of Merit Enhancement in Nanostructured Antimony Telluride by Antisite Defect Suppression through Sulfur Doping.* Nano Letters, 2012. **12**(9): p. 4523-4529.

[13] B. Fang, Z. Zeng, X. Yan, Z. Hu, *Effects of annealing on thermoelectric properties of Sb2Te3 thin films prepared by radio frequency magnetron sputtering.* Journal of Materials Science: Materials in Electronics, 2013. **24**(4): p. 1105-1111.

[14] J. S. Lee, S. Brittman, D. Yu, H. Park, *Vapor–Liquid–Solid and Vapor–Solid Growth of Phase-Change Sb2Te3 Nanowires and Sb2Te3/GeTe Nanowire Heterostructures.* Journal of the American Chemical Society, 2008. **130**(19): p. 6252-6258.

[15] M. Wuttig, and N. Yamada, *Phase-change materials for rewriteable data storage.* Nat Mater, 2007. **6**(11): p. 824-832.

[16] G.S. Nolas, J.S., H.J. Goldsmid, *Thermoelectrics: Basic principles and new materials developments.* Springer: New York, 2001.

[17] Qi, X.-L. and S.-C. Zhang, *Topological insulators and superconductors.* Reviews of Modern Physics, 2011. **83**(4): p. 1057-1110.

[18] Y. M. Zuev, J. S. Lee, C. m. Galloy, H. Park, P. Kim, *Diameter Dependence of the Transport Properties of Antimony Telluride Nanowires.* Nano Letters, 2010. **10**(8): p. 3037-3040.

[19] H. Zhang, C.-X. Liu, X.-L. Qi, X. Dai, Z. Fang, S.-C. Zhang, *Topological insulators in Bi2Se3, Bi2Te3 and Sb2Te3 with a single Dirac cone on the surface.* Nat Phys, 2009. **5**(6): p. 438-442.

[20] M. S. Dresselhaus, G. Dresselhaus, X. Sun, Z. Zhang, S. B. Cronin, T. Koga, *Low-dimensional thermoelectric materials.* Physics of the Solid State, 1999. **41**(5): p. 679-682.

[21] S.-H. Lee, Y. Jung, and R. Agarwal, *Highly scalable non-volatile and ultra-low-power phase-change nanowire memory.* Nat Nano, 2007. **2**(10): p. 626-630.

[22] W. Shi, J. Yu, H. Wang, H. Zhang, *Hydrothermal Synthesis of Single-Crystalline Antimony Telluride Nanobelts.* Journal of the American Chemical Society, 2006. **128**(51): p. 16490-16491.

[23] P. Christian, and P. O'Brien, *The preparation of antimony chalcogenide and oxide nanomaterials.* Journal of Materials Chemistry, 2005. **15**(46): p. 4949-4954.

[24] WangWang; B. Poudel, J. Yang, D. Z. Wang, Z. F. Ren, *High-Yield Synthesis of Single-Crystalline Antimony Telluride Hexagonal Nanoplates Using a Solvothermal Approach.* Journal of the American Chemical Society, 2005. **127**(40): p. 13792-13793.

[25] J. R. Lim, J. F. Whitacre, J. P. Fleurial, C. K. Huang, M. A. Ryan, N. V. Myung, *Fabrication Method for Thermoelectric Nanodevices.* Advanced Materials, 2005. **17**(12): p. 1488-1492.

[26] B. Yoo, F. Xiao, K. N. Bozhilov, J. Herman, M. A. Ryan, N. V. Myung, *Electrodeposition of Thermoelectric Superlattice Nanowires.* Advanced Materials, 2007. **19**(2): p. 296-299.

[27] V. Richoux, S. Diliberto, and C. Boulanger, *Pulsed Electroplating: a Derivate Form of Electrodeposition for Improvement of (Bi1−xSbx)2Te3 Thin Films.* Journal of Electronic Materials, 2010. **39**(9): p. 1914-1919.

[28] C. Schumacher, K. G. Reinsberg, R.Rostek, L. Akinsinde, S. Baessler, S. Zastrow, G. Rampelberg, P. Woias, C. Detavernier, J. A. C. Broekaert, J.

Bachmann, K. Nielsch, *Optimizations of Pulsed Plated p and n-type Bi2Te3-Based Ternary Compounds by Annealing in Different Ambient Atmospheres.* Advanced Energy Materials, 2013. **3**(1): p. 95-104.

[29] D. Pinisetty, M. Gupta, A. B. Karki, D. P. Young, R. V. Devireddy, *Fabrication and characterization of electrodeposited antimony telluride crystalline nanowires and nanotubes.* Journal of Materials Chemistry, 2011. **21**(12): p. 4098-4107.

[30] D.-A. Borca-Tasciuc, and G. Chen, *Anisotropic thermal properties of nanochanneled alumina templates.* Journal of Applied Physics, 2005. **97**(8):

[31] M. Muñoz Rojo, S. J.-M. Grauby, Rampnoux, O. Caballero-Calero, M. Martin-Gonzalez, S. Dilhaire, *Fabrication of Bi2Te3 nanowire arrays and thermal conductivity measurement by 3ω-scanning thermal microscopy.* Journal of Applied Physics, 2013. **113**(5):

[32] H. Jung, D.-Y. Park, F. Xiao, K. H. Lee, Y.-H. Choa, B. Yoo, N. V. Myung, *Electrodeposited Single Crystalline PbTe Nanowires and Their Transport Properties.* The Journal of Physical Chemistry C, 2011. **115**(7): p. 2993-2998.

[33] H. Jung, and N.V. Myung, *Electrodeposition of antimony telluride thin films from acidic nitrate-tartrate baths.* Electrochimica Acta, 2011. **56**(16): p. 5611-5615.

[34] H. Jung, J.-H. Lim, H. Park, J. Kim, Y.-H. Choa, N. V. Myung, *Lithographically Patterned p-Type SbxTey Nanoribbons with Controlled Morphologies and Dimensions.* The Journal of Physical Chemistry C, 2013. **117**(33): p. 17303-17308.

[35] I.-J. Yoo, Y. Song, D. Chan Lim, N. V. Myung, K. H. Lee, M. Oh, D. Lee, Y. D. Kim, S. Kim, Y.-H. Choa, J. Y. Lee, K. H. Lee, J.-H. Lim, *Thermoelectric characteristics of Sb2Te3 thin films formed via surfactant-assisted electrodeposition.* Journal of Materials Chemistry A, 2013. **1**(17): p. 5430-5435.

[36] G. Leimkühler, I. Kerkamm, and R. Reineke-Koch *Electrodeposition of Antimony Telluride.* Journal of The Electrochemical Society, 2002. **149**(10): p. C474-C478.

[37] C. Guo, C. Li, and Z. Du, *Thermodynamic Re-modeling of the Sb-Te System Using Associate and Ionic Models.* Journal of Electronic Materials, 2014. **43**(11): p. 4082-4089.

[38] Q. Huang, A.J. Kellock, and S. Raoux, *Electrodeposition of SbTe Phase-Change Alloys.* Journal of The Electrochemical Society, 2008. **155**(2): p. D104-D109.

[39] S.A. Baily, and D. Emin, *Transport properties of amorphous antimony telluride.* Physical Review B, 2006. **73**(16): p. 165211.

[40] V. Damodara Das, N. Soundararajan, and M. Pattabi, *Electrical conductivity and thermoelectric power of amorphous Sb2Te3 thin films and amorphous-crystalline transition.* Journal of Materials Science, 1987. **22**(10): p. 3522-3528.

[41] N.G. Patel, and P.G. Patel, *Electrical properties of polycrystalline Sb2Te3 films.* Journal of Materials Science, 1991. **26**(9): p. 2543-2546.

[42] S. Zastrow, J. Gooth, T. Boehnert, S. Heiderich, W. Toellner, S. Heimann, S. Schulz, K. Nielsch, *Thermoelectric transport and Hall measurements of low defect Sb 2 Te 3 thin films grown by atomic layer deposition.* Semiconductor Science and Technology, 2013. **28**(3): p. 035010.

[43] E. Morales-Sanchez, E. Prokhorov, J. Gonzalez-Hernandez, M. A. Hernandez-Landaverde, B. Chao, *Crystallization of SbTe Phase Change Optical Films*. in *Electrical and Electronics Engineering, 2007. ICEEE 2007. 4th International Conference on*. 2007.

[44] O. Madelung, U.R., M. Schulz, *Non-Tetrahedrally Bonded Elements and Binary Compounds I.* Landolt-Börnstein - Group III Condensed Matter, 1998. **41C**: p. 1-4.

[45] A. Zimmer, N. Stein, L. Johann, H. Terryn, C. Boulanger, *Characterizations of bismuth telluride films from Mott-Schottky plot and spectroscopic ellipsometry.* Surface and Interface Analysis, 2008. **40**(3-4): p. 593-596.

[46] E.A. Hernández-Pagán, W. Wang, and T.E. Mallouk, *Template Electrodeposition of Single-Phase p- and n-Type Copper Indium Diselenide (CuInSe2) Nanowire Arrays.* ACS Nano, 2011. **5**(4): p. 3237-3241.

[47] K. Tittes, and W. Plieth, *Electrochemical deposition of ternary and binary systems from an alkaline electrolyte—a demanding way for manufacturing p-doped bismuth and antimony tellurides for the use in thermoelectric elements.* Journal of Solid State Electrochemistry, 2007. **11**(2): p. 155-164.

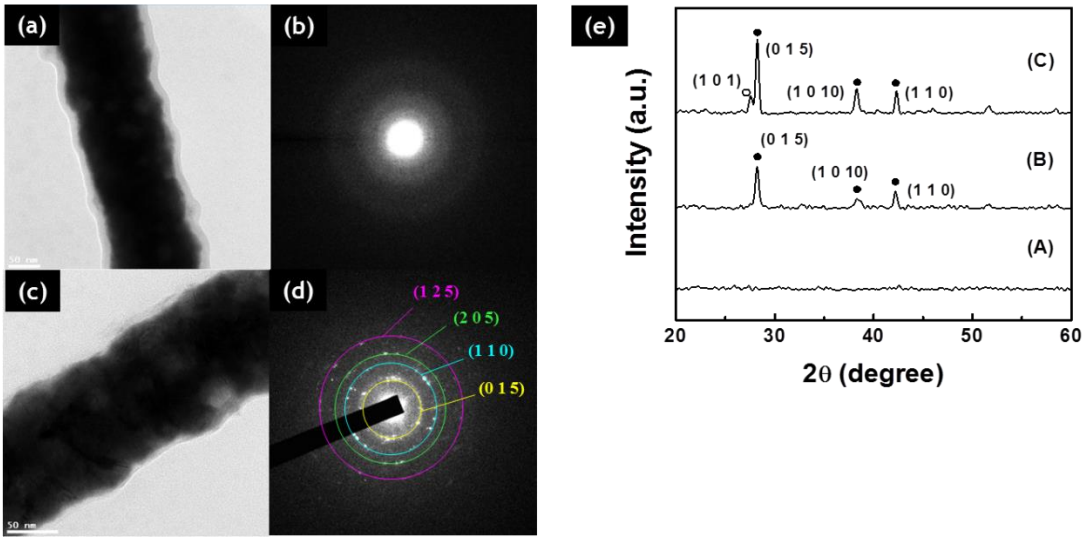

Figure 5.1 TEM images and SAED patterns of $Sb_{36}Te_{64}$ nanowire before (a,b) and after thermal-cycle (300 K to 370 K) (c,d). XRD analysis of the nanowire embedded AAO (e) [as-deposited (A), annealed at 100 ^{o}C (B), and 200 ^{o}C (C) for 2 hr]. Solid circle represents rhombohedral Sb_2Te_3 from JCPDS 15-0874, open circle represents tetragonal-Te from JCPDS 36-1452.

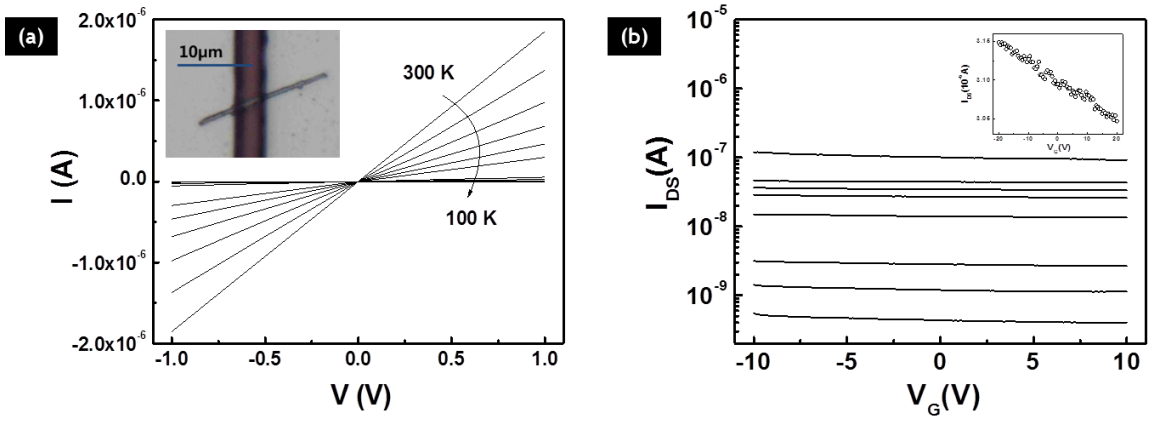

Figure 5.2 Temperature-dependent I-V curves (a) and back-gated I_{DS}-V_G curves at the fixed V_{DS} of +0.5 V (b) of a single $Sb_{36}Te_{63}$ nanowire. An inset in Fig. 2a represents an optical image of a real device with an aligned single nanowire with Pt contacts. An inset in Fig. 2b represents a back-gated I_{DS}-V_G curve at room temperature.

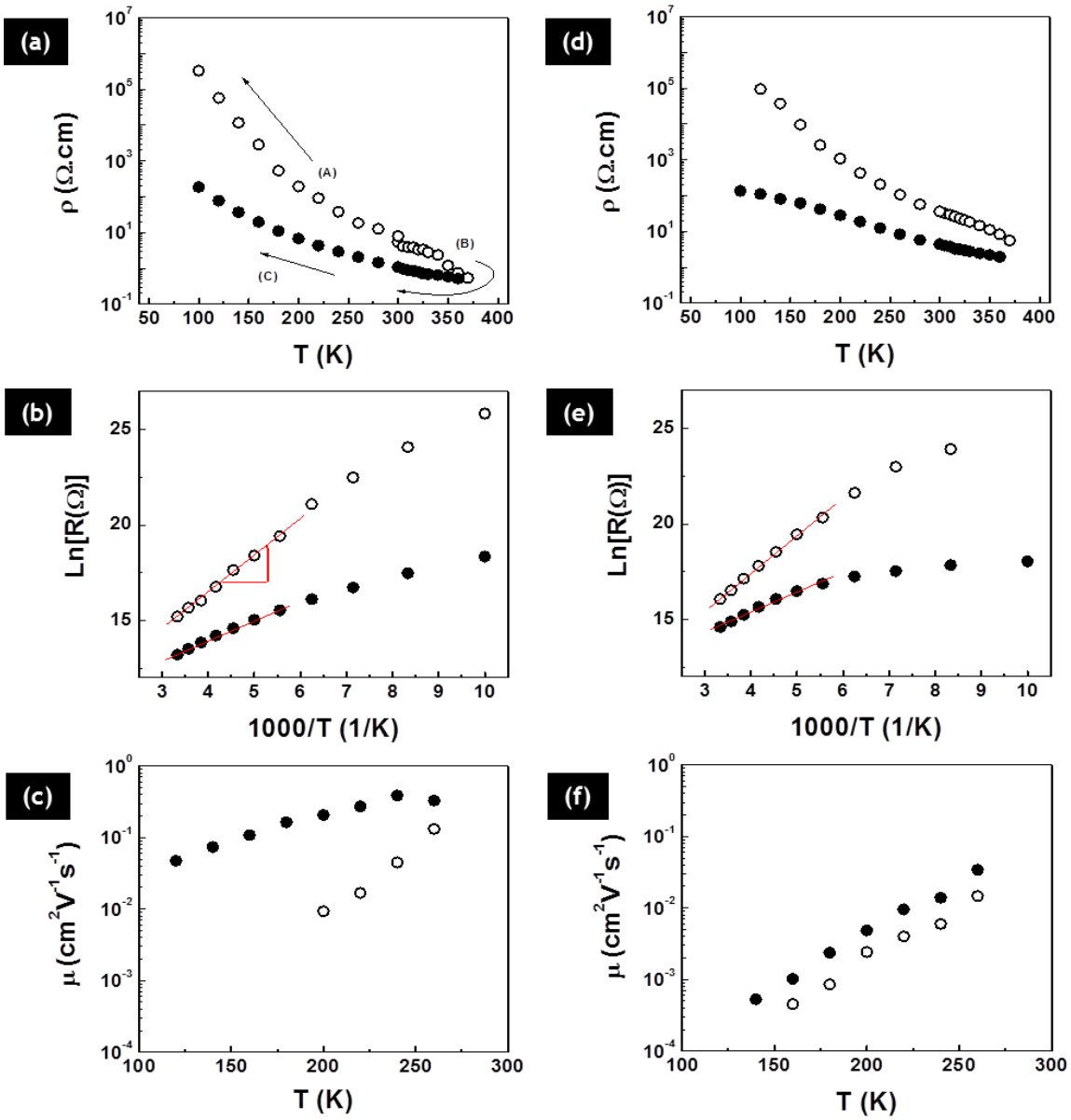

Figure 5.3 Temperature-dependent electrical resistivity, natural log of electrical resistance, and FET-mobility of as-deposited (open circle) and thermal-cycled (solid circle) $Sb_{36}Te_{64}$ (a-c) and $Sb_{53}Te_{47}$ (d-f) nanowires.

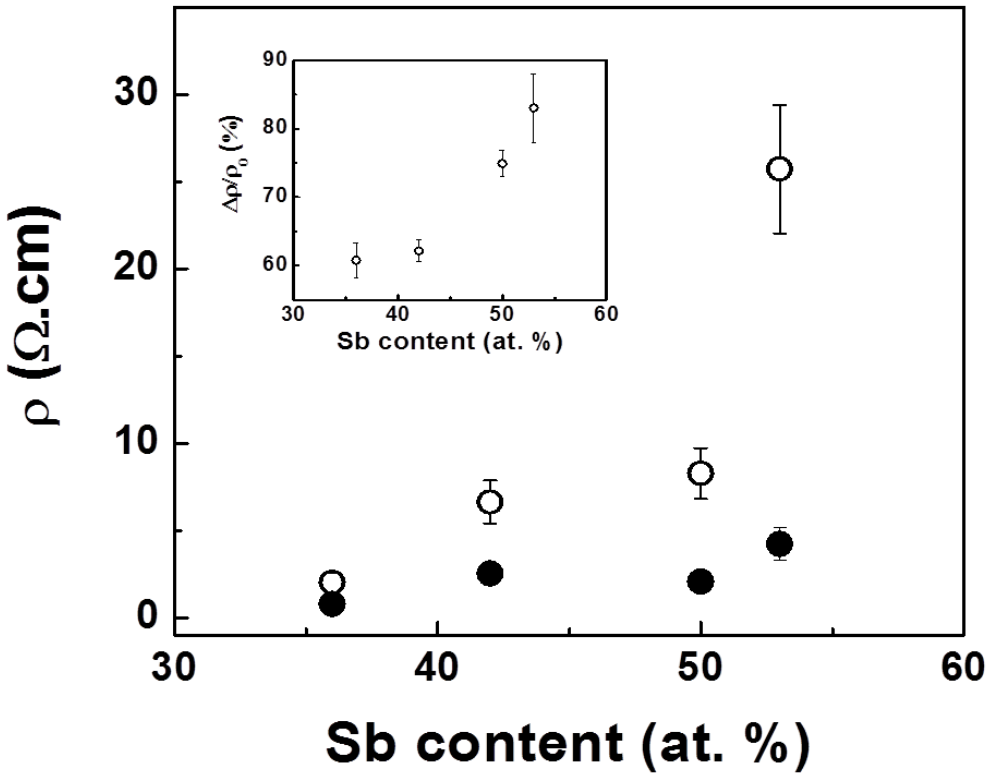

Figure 5.4 Composition-dependent electrical resistivity changes of Sb_xTe_y nanowires: electrical resistivity of nanowires before (open circle) and after thermal-cycle (solid circle). An inset represents resistivity variation ratio ($\Delta\rho/\rho_0$) as a function of Sb content.

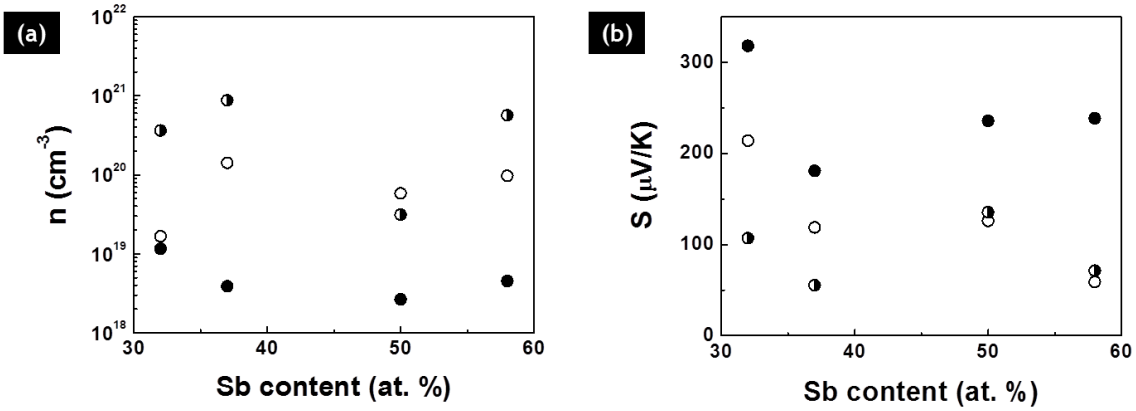

Figure 5.5 Composition and annealing effects on carrier concentration and Seebeck coefficient of Sb_xTe_y nanowires as-deposited (open circle), annealed at 100 ^oC (half-solid circle) and 200 ^oC (solid circle).

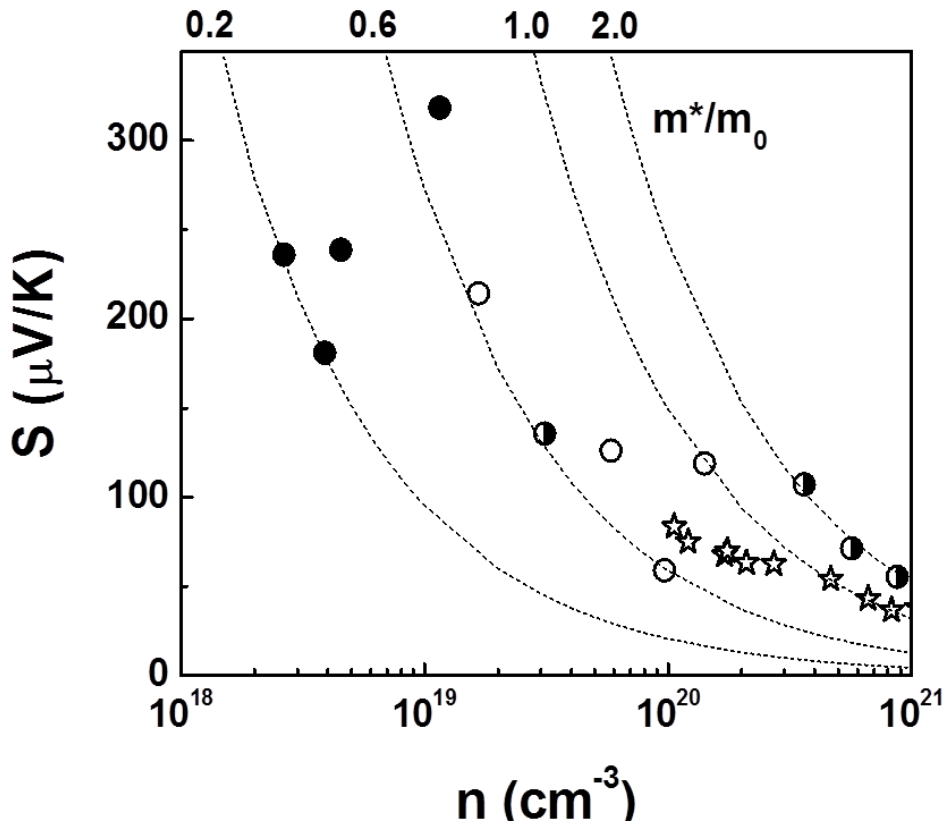

Figure 5.6 Seebeck coefficient as a function of carrier concentration (Pisarenko plot) at room temperature for as-deposited and annealed Sb_xTe_y nanowires. Dashed lines are theoretical fittings by Mott-relation. (as-deposited (open circle), annealed at 100 ^oC for 2hr (half-solid circle), annealed at 200 ^oC for 2hr (solid circle)).

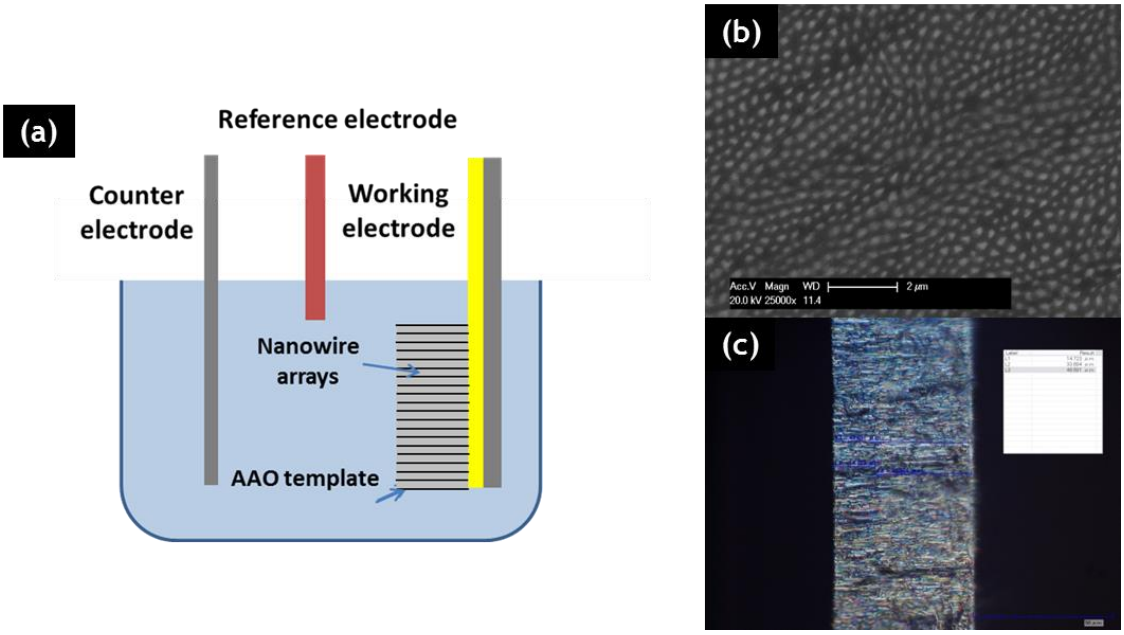

Figure 5.7 Schematic of Mott-Schottky analysis using Sb_xTe_y nanowire arrays embedded in an AAO template (a), SEM image of surface (b), and optical image of cross-section of AAO template with embedded nanowires(c).

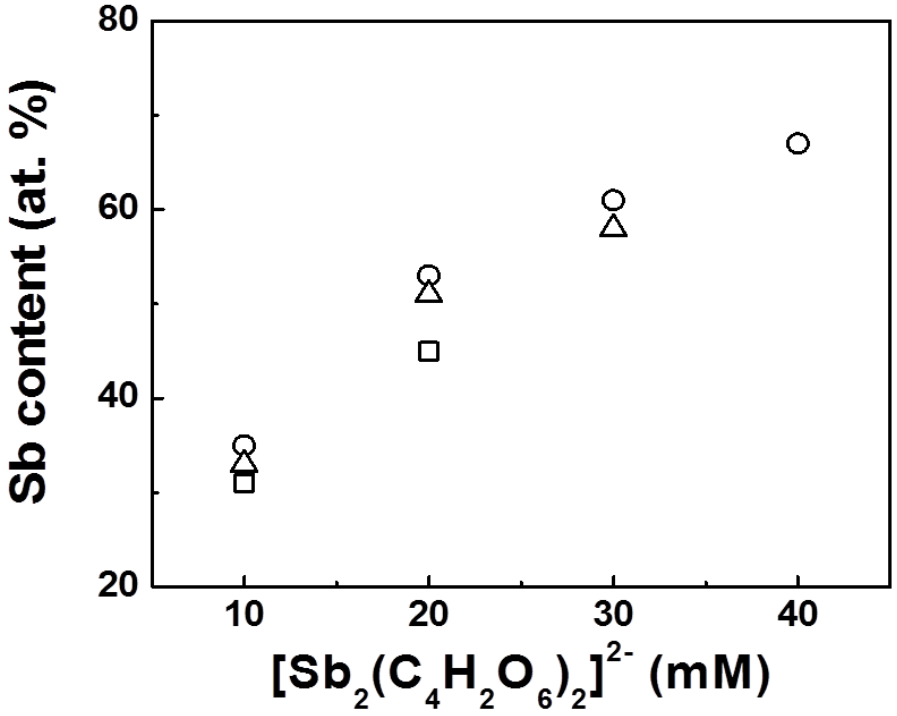

Figure 5.8 Effect of applied potential and $[Sb_2(C_4H_2O_6)_2]^{2-}$ concentration on Sb content in Sb_xTe_y nanowires (-0.2 V, square, -0.25 V, triangle, -0.3 V, circle).

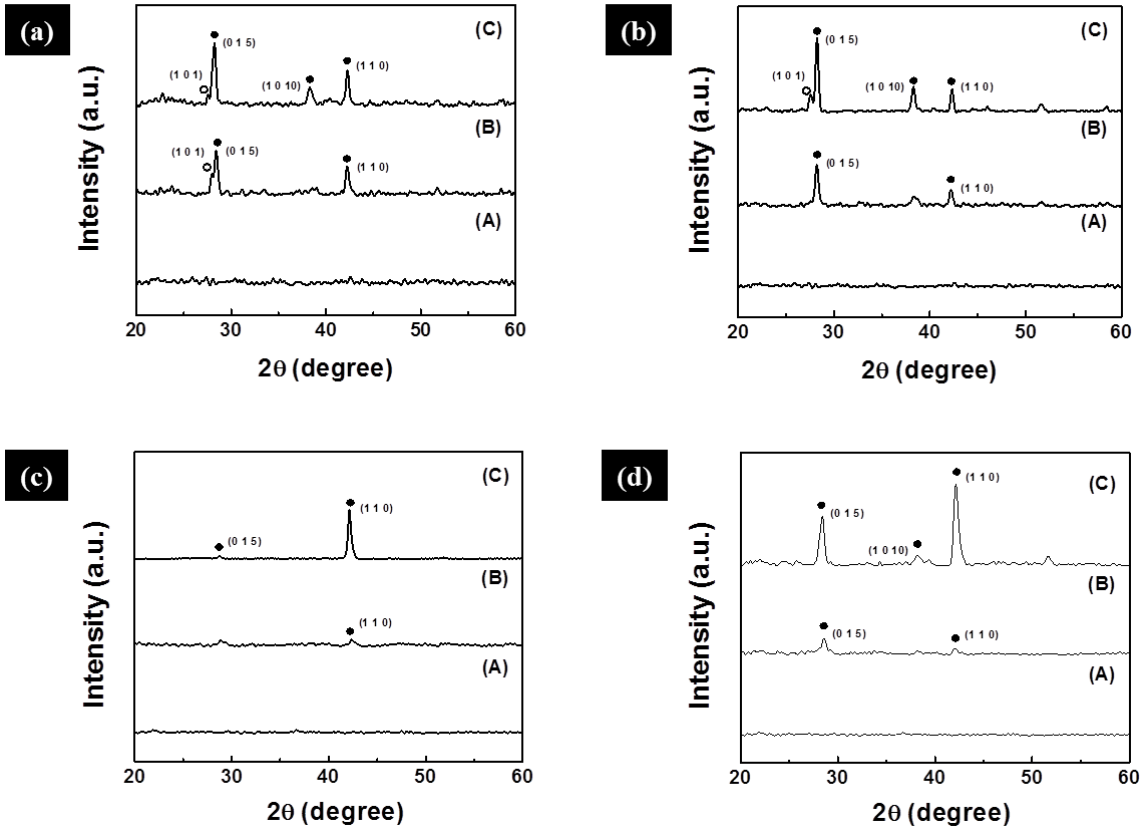

Figure 5.9 XRD analysis of as-deposited (A) and annealed (at 100 ^{o}C (B) and 200 ^{o}C (C) for 2 hr) $Sb_{32}Te_{68}$ (a), $Sb_{37}Te_{63}$ (b), $Sb_{50}Te_{50}$ (c), and $Sb_{58}Te_{42}$ (d) nanowires embedded in AAO templates. Solid circle represents rhombohedral Sb_2Te_3 from JCPDS 15-0874, open circle represents tetragonal-Te from JCPDS 36-1452.

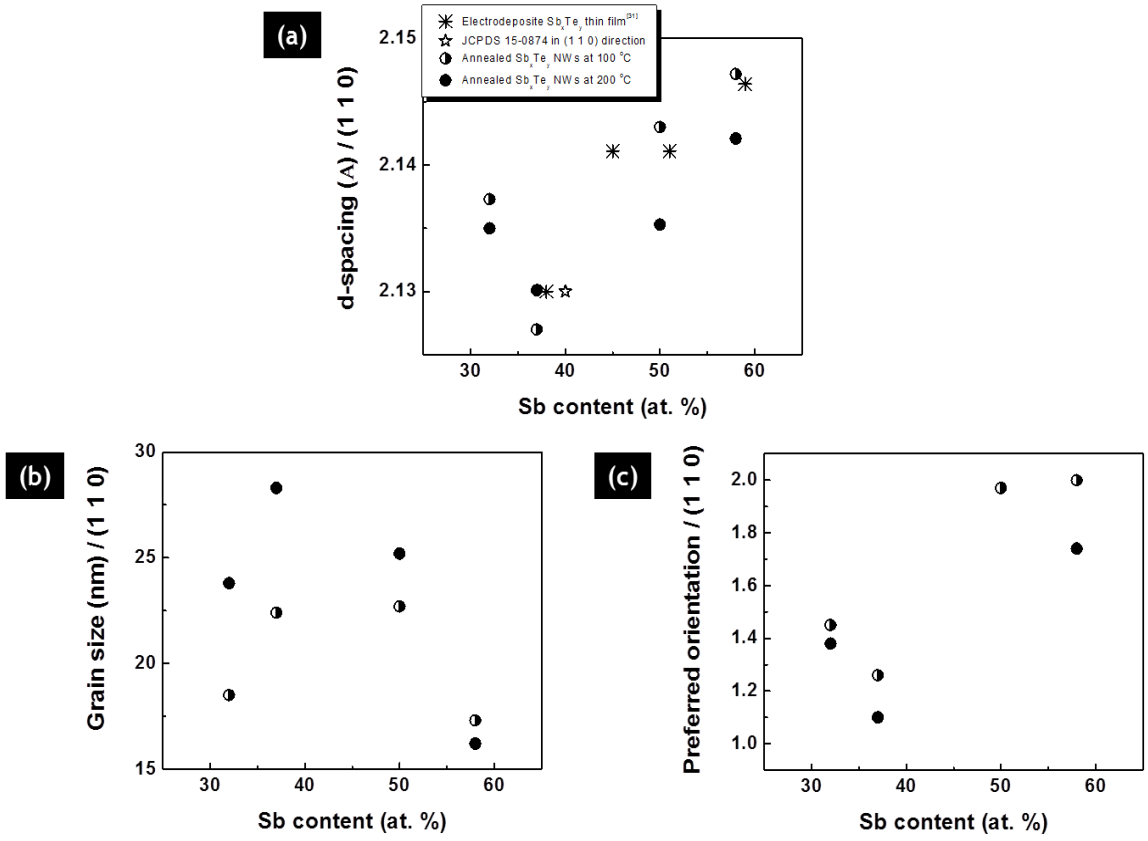

Figure 5.10 Annealing effects: d-spacing (a), grain size (b) and preferred orientation (c) of Sb_xTe_y nanowires after annealing at 200 ^oC for 2hr.

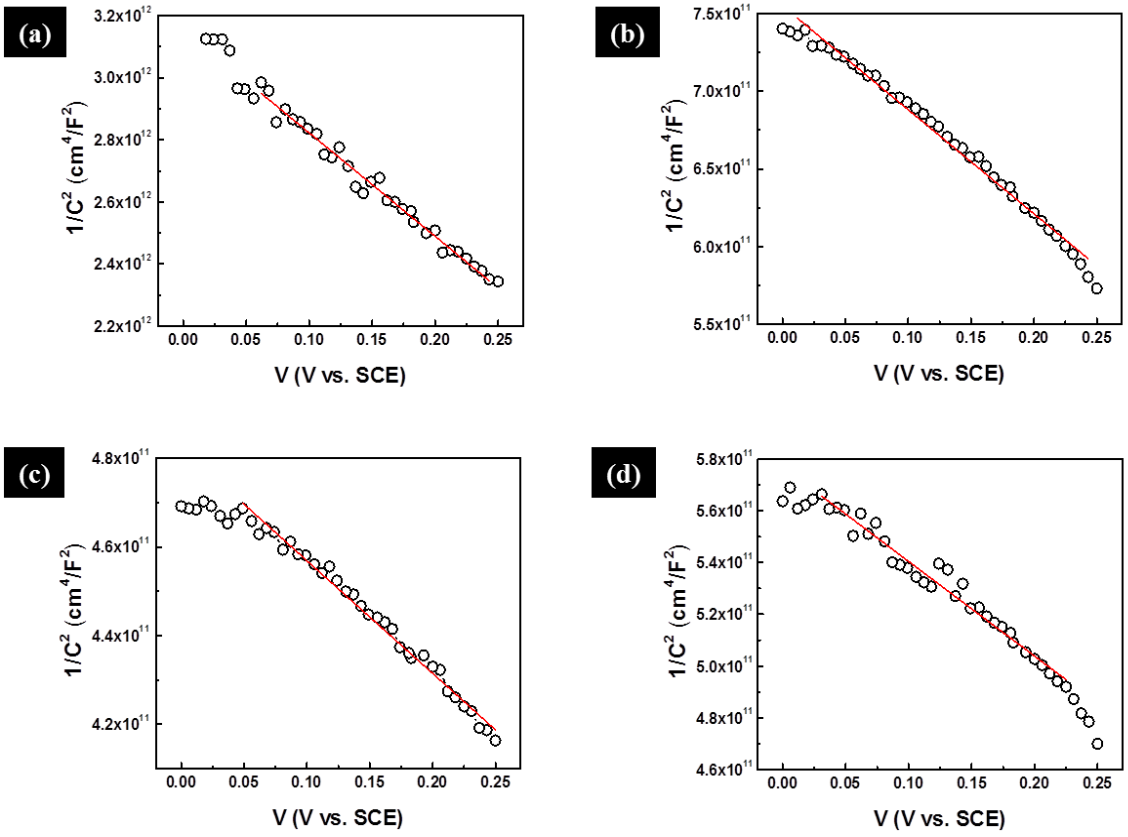

Figure 5.11 Mott-Schottky plots for as-deposited $Sb_{32}Te_{68}$ (a), $Sb_{37}Te_{63}$ (b), $Sb_{50}Te_{50}$ (c), and $Sb_{58}Te_{42}$ (d) nanowires embedded in AAO templates.

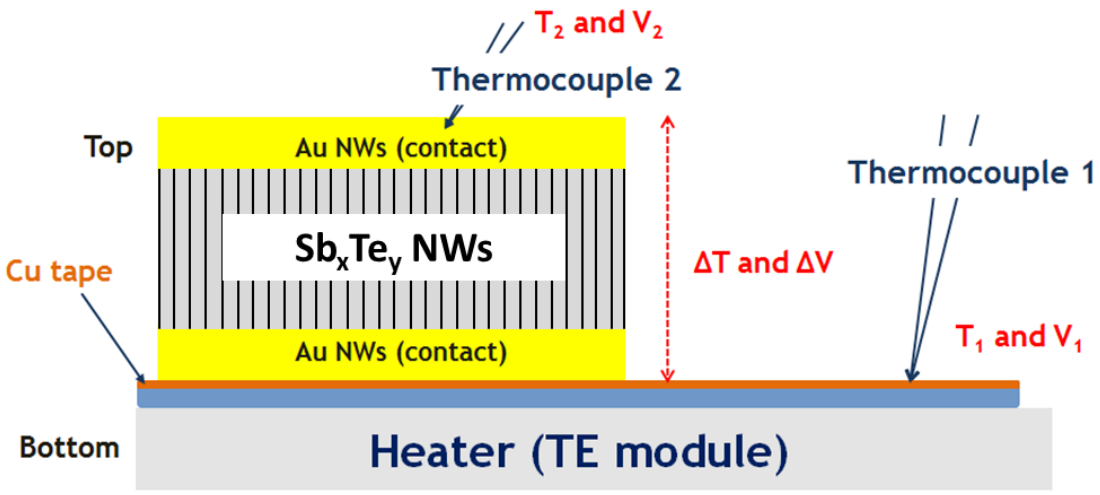

Figure 5.12 Schematic of Seebeck coefficient measurement of Sb_xTe_y nanowire arrays embedded in an AAO template.

CHAPTER 6 Thermoelectric Characteristics of Amorphous and Nanocrystalline $Ag_xSb_{2-x}Te_{3-x}$ Electrodeposits

6.1 Abstract

Silver antimony telluride ($Ag_xSb_{2-x}Te_{3-x}$) thin films with tailored compositions were electrochemically synthesized for the first time. To investigate the effect of crystallinity and composition on the thermoelectric properties, amorphous Ag-Sb-Te solid solutions with various compositions were first electrodeposited by tailoring the electrolyte concentration, followed by a thermally driven solid-state amorphous-to-nanocrystalline phase transition. The thermoelectric properties of the films were evaluated by measuring their electrical conductivity, Hall mobility, carrier concentration, and the Seebeck coefficient. The crystallographic properties of the various single-phased nanocrystalline $Ag_xSb_{2-x}Te_{3-x}$ thin films were highly correlated with the Ag content, and that the carrier concentration of the films could be controlled between 10^{16} ~ 10^{19} cm^{-3} without inducing a secondary phase. The composition dependent Seebeck coefficient ranged from 170 to ~2766 μV/K with the highest power factor peaked near the composition $AgSbTe_2$ (actual x ~ 0.98).

6.2 Introduction

Silver antimony telluride ($AgSbTe_2$) belongs to the cubic NaCl structure (*Fm-3m*) in which silver (Ag) and antimony (Sb) atoms randomly occupy Na sites. Such atomic

disorder in the $AgSbTe_2$ lattice structure has been shown to modulate the band gap energy from 0.026 ~ 0.6 eV, thereby transforming its electrical properties from a narrow-gap semiconductor to a semimetal[1-3] and induce anomalous optical and thermoelectric properties.[4-6] Specifically, as a p-type thermoelectric material, the ternary $AgSbTe_2$ bulk compounds have displayed Seebeck coefficient ranging from 40 ~ 295 μV/K, changes in electrical conductivity from 130 ~ 1450 S/cm, power factor ranging between 153 ~ 2340 $\mu W/mK^2$ and low thermal conductivity in the 0.3 ~ 0.7 W/mK range at room temperature.[2,3,7-15]

As efforts continue to enhance the thermoelectric performance of $AgSbTe_2$, scattering mechanisms of charge carriers (hole or electrons) have also been studied. For example, the nanosized Ag- and Sb-rich clusters in the $AgSbTe_2$ system enhanced the zT value to 2.2 at 800 K due to the appearance of resonant states in modified Te-Ag and Sb bonds.[16] In addition, the creation of two-phase mixture of the $AgSbTe_2$ system with a second phase (e.g., Ag_2Te and Sb_2Te_3) by solid-state precipitation also altered the scattering mechanism of charge carriers at hetero-phase interfaces; thereby, increasing the Seebeck coefficient, and lowering the thermal conductivity.[12,14,17] Although these works successfully improved the improved thermoelectric performance, the improvements were for bulk compounds not for low dimensional $AgSbTe_2$ nanostructures.

In thermoelectrics, the optimization of carrier concentration is critical for enhanced thermoelectric efficiency ($zT= \sigma S^2T/\kappa$) because the Seebeck coefficient *S*, and the electrical conductivity σ, and the thermal conductivity κ are dependent on the carrier

concentration. The electronic structure calculation for $AgSbTe_2$ shows that the valence-band top is composed of Te 5*p*, while the conduction-band bottom is of Ag 5*s* and Sb 5*p*.[18] As the band corresponding to the *s* states of Ag is shifted down to the top of the valence band, the bandgap of the $AgSbTe_2$ system is altered to the level of the carrier concentration. Other supporting experiments, such as replacing Ag atoms with dopants (e.g., Na, Bi, or In) of higher *s* state energies, were also found to be an efficient way to enhance the Seebeck coefficient.[18-20] Prior to doping, however, a level of p-type carrier (holes) of the $AgSbTe_2$ can be altered by controlling its chemical composition. Relatively weak binding of Ag within the lattices makes it energetically easy to form an Ag vacancy; i.e., a Frenkel pair/disorder and a strong source for holes. Like holes, an excess of Te can also increase the cation vacancy concentrations.

Finding a novel synthesis approach that facilitates the formation of stable and reproducible materials determines the commercial applicability for solid-state electronics. For example, inhomogeneous material leads to the undermined intrinsic material properties such as the transport properties. Electrodeposition is one of the most versatile and easiest solution-based synthesis techniques for low dimensional nanostructures in a cost effective and scalable manner.[21-24] Precise control over dimension, composition, morphology and degree of crystallinity can be achieved by simply varying the electrodeposition parameters such as applied potential, electrolyte concentration, temperature, agitation, and additives. Especially, based on the non- equilibrium reaction, non- or stoichiometric materials can be easily synthesized without changing other aspects of the material properties. Therefore, the strategy for high Seebeck coefficient and

electrical conductivity to maximize the power factor (P.F.=σS^2) can be extended to a better understanding of the composition- and crystallinity dependent electrical and thermoelectric properties. However, no systematic study has been devoted leading to a detailed understanding of how the thermoelectric and transport properties of $AgSbTe_2$ thin films change as a function of composition.

In this work, we synthesized $Ag_xSb_{2-x}Te_{3-x}$ thin films by using the electrodeposition technique and characterized them for their thermoelectric applications for the first time. The level of the carrier concentration was controlled by the chemical composition and crystallinity of the $Ag_xSb_{2-x}Te_{3-x}$ thin films. The composition and crystallinity of the films were tailored by the electrolyte concentration and a post-annealing process, respectively. The thermoelectric performance was evaluated by measuring the electrical conductivity, Hall mobility, carrier concentration and Seebeck coefficient of the films to find the optimum for the best thermoelectric efficiency. Furthermore, the crystallographic properties of the films were investigated as a function of the composition.

6.3 Experimental Section

6.3.1 Synthesis of $Ag_xSb_{2-x}Te_{3-x}$ Thin Films

$Ag_xSb_{2-x}Te_{3-x}$ thin films were potentiostatically electrodeposited with a control of the concentration of electrolytes and applied potentials. According to our previous works on the electrodeposition of binary Sb_xTe_y thin films, the morphology, crystallinity, and chemical composition of the thin films were highly dependent on the electrolyte concentration and applied potentials. In this work, the electrodeposition conditions for

dense and smooth morphology with an amorphous phase of the films were utilized from our previous work except the part of adding the $AgNO_3$ as an Ag^+ source in the electrolyte. The chemical composition of ternary $Ag_xSb_{2-x}Te_{3-x}$ thin films was tailored by controlling the $AgNO_3$ concentration in the electrolytes. The electrolyte was prepared by separately dissolving a 2.4 mM TeO_2 in a 1 M HNO_3 solution, a 3.6 mM Sb_2O_3 in a 33 mM L-tartaric acid solution at 60 ^oC, and 400 ~ 1000 μM $AgNO_3$ in a deionized water. The dissolved solutions were then mixed together and deionized water was added to reach final volume of 1 L. The concentration of $AgNO_3$ in the electrolyte was varied 400, 600, 800, and 1000 μM to achieve the ternary $Ag_xSb_{2-x}Te_{3-x}$ thin films with tailored composition. The working electrode was e-beam evaporated using Au (80 nm)/Ni (20 nm) films on a Si substrate, and a Pt coated titanium electrode and a saturated calomel electrode (SCE) were used as the counter and reference electrodes, respectively. A potential of -0.1 V (V vs. SCE) was applied for 10 minutes and the electrolyte was kept at 25 ^oC and magnetically stirred at 300 rpm. The deposited film was amorphous, dense, and smooth 2 cm in diameter with a uniform thickness of 1 μm.

6.3.2 Sample Preparation

For electrical and thermoelectric characterization, the thin films were transferred from the Au/Ni/Si substrate to a non-conductive Torr Seal epoxy substrate (Varian Vacuum Products, Lexington, Massachusetts). The entire film was successfully transferred without cracking. The final dimensions of the sample for characterization were 1 cm^2.

6.3.3 Characterization

Morphology and composition of the synthesized $Ag_xSb_{2-x}Te_{3-x}$ thin films were analyzed by scanning electron microscopy (SEM) (Jeol, JSM-5800) and energy dispersive X-ray spectroscopy (EDS). The effect of the composition on crystallinity and crystallographic properties of the $Ag_xSb_{2-x}Te_{3-x}$ thin films were investigated as a function of the Ag content by X-ray diffraction (XRD) (Bruker D8 ADVANCE). In addition, a post-annealing process was added to further enhance the structural properties, where the films were annealed at 100 ^oC for 30 min in a nitrogen atmosphere with 5 % hydrogen present. The electrical conductivity, Hall mobility, and carrier concentration of the film were investigated by a custom-made Hall measurement unit in the van der Pauw configuration with four-point probes. The Seebeck coefficient was determined by a custom-made Seebeck measurement system by plotting the measured Seebeck voltages as a function of temperature difference (<2 ^oC) across the sample ($S = \Delta V/\Delta T$).

6.4 Results and Discussion

6.4.1 Synthesis and Material Properties of $Ag_xSb_{2-x}Te_{3-x}$ Thin Films

The synthesis of ternary $Ag_xSb_{2-x}Te_{3-x}$ thin films using an electrodeposition was demonstrated. The control over the morphology, composition, and crystallinity of the ternary $Ag_xSb_{2-x}Te_{3-x}$ thin films was achieved by varying the concentration of Ag^+ in the electrolyte from 0 to 1000 μM. The composition of the films as a function of the concentration of Ag^+ is indicated in Figure 6.1. The applied potential was fixed as -0.1 V (V vs. SCE) for all of electrodeposition. The Ag content increased almost linearly with

the concentration of Ag^+ increased accompanied by the linear decrease of the Sb and Te content. As the Ag^+ concentration increased in the electrolyte, the relative deposition rate of Ag^+ on to the film enhanced, thus, the overall composition was competitively shifted under the fixed driving force. The morphology of the electrodeposited thin films was confirmed by SEM analysis as shown in Figure 6.7. Smooth and dense morphology was observed independently of the Ag content in all films. This morphology is a suitable configuration for precise Hall measurements. From this observation, the composition-modulated but independently maintained uniform morphology of the $Ag_xSb_{2-x}Te_{3-x}$ thin films were successfully synthesized by simply varying the electrolyte concentration.

The selected value for the applied potential was anticipated to synthesize the amorphous phase thin films according to our previous study. The initially amorphous phased thin films with tailored composition provide an additional opportunity to control the level of carrier concentration by developing and optimizing their crystallinity through a post-annealing process. Therefore, this approach is able to open the large window to manipulate the electrical conductivity for enhanced thermoelectric performance of the $Ag_xSb_{2-x}Te_{3-x}$ thin films. The crystallinity and crystal structure of the electrodeposited thin films were investigated by XRD analysis in Figure 6.2. As expected, the as-deposited thin films (Figure 6.2a) were all amorphous phases which is confirmed by no peak raised except the large Ag/Ni/Si substrate peak. The crystal structure of $AgSbTe_2$ is known as a rock-salt (NaCl) type structure with Te atoms occupying the Cl sites, and Ag and Sb atoms randomly arranged at the Na sites.[7] Due to this abnormal crystal structure, the atomic ordering and gap formation of ternary Ag-Sb-Te system can be systematically

differentiated as a function of the ratio of Ag/Sb and Te atom, which eventually affect a small intrinsic band gap and shallow impurity states of the system.[25] In order to form the ordered structures of the $Ag_xSb_{2-x}Te_{3-x}$ thin films the solid-state crystallization process was performed by the post-annealing process at 100 ^oC for 30 min in 90 % N_2/ 10 % H_2 atmosphere. The clearly defined peaks after annealing at all films were well matched with JCPDS standard for *Fm3m*-$AgSbTe_2$ (15-0540). More detailed crystallographic properties such as grain size and d-spacing of the $Ag_xSb_{2-x}Te_{3-x}$ thin films can be obtained by the Scherrer equation as a function of Ag content. The main peak (200) was selected for the analysis of composition-dependent d-spacing and grain size of the $Ag_xSb_{2-x}Te_{3-x}$ thin films after annealing as described in Figure 6.3. For comparison, the d-spacing value of standard $AgSbTe_2$ was referred in Figure 6.3a (symbol of empty star). Among the various samples, two films with x = 0.98 and 1.1 showed the similar d-spacing values compared to the ref. value (x=1). In contrast, when the portion of Ag was reduced or raised from x=1, their d-spacing values were about 0.5% higher than the ref. value. This might be the result of the large differences in the atomic radii among Ag (1.65 Å), Sb (1.33 Å), and Te (1.23 Å). The randomly substituted larger Ag atoms into smaller Sb and even Te lattice points can alter the distance of atomic lattices which was represented as varied d-spacing values as a function of the chemical composition changes. Meanwhile, the calculated grain sizes of the films ranged from roughly 8.5 to 9.75 nm, indicating that the synthesized films were nanocrystalline structures.

6.4.2 Electrical Transport and Thermoelectric Properties of $Ag_xSb_{2-x}Te_{3-x}$ Thin Films

Due to the intriguing physical property of $AgSbTe_2$ as a result of the randomly occupied Ag and Sb atoms in the lattices, several theoretical and experimental studies have been conducted for its impact on the electronic properties. According to Hoang *et al.*, the covalency effects play an important role in the energetics of disordered structures.[25] For instance, depending on the location of Ag atoms within the structures, reciprocative perturbation of hybridized Sb and Te *p*-bands leads to a rearrangement in the density of states (DOS) by shifting states near E_F. In addition, they also calculated the non-stoichiometry effect on the possible antisite defects generated from Ag substitution into Sb lattices, and indicated an enhancement in the DOS near E_F. Therefore, manipulating the order and the amount of Ag/Sb in the Ag-Sb-Te system enables one to control the DOS near the E_F, thereby making a new narrow band-gap semiconductors for thermoelectric applications is anticipated. Here, the composition-dependent electrical conductivity, Hall mobility, and carrier concentration of $Ag_xSb_{2-x}Te_{3-x}$ thin films are described in Figure 6.4. The room temperature measurement was conducted on amorphous phase (symbol of empty circle) and nanocrystalline (symbol of solid circle) films in order to observe the crystallinity effect on their transport properties as well. As shown in Figure 6.4a, the lowest conductivity of ~0.02 S/cm was observed in the $Ag_{25}Sb_{21}Te_{54}$ thin film with the lowest carrier concentration of 1.28×10^{15} cm^{-3} and the mobility of 104 cm/V.s. As the composition was deviated from stoichiometry (x=1), the conductivity of amorphous thin films slightly increased up to 0.05 S/cm. This trend was

consistent with that of the carrier concentration. In contrast, the mobility values of the films showed the opposite trend. After annealing at 100 ^{o}C for 30 min, compared to the amorphous films, almost 1000 times higher values of electrical conductivity were observed in all of the films because of their enhanced crystallinity (Figure 6.2b). Interestingly, the carrier concentration and Hall mobility of the nanocrystalline $Ag_xSb_{2-x}Te_{3-x}$ thin films were strictly dependent on the composition. Among the various composition films, the lowest carrier concentration of 1.62 x 10^{16} cm^{-3} with the highest mobility of 8250 cm^2/V.s was observed in the nanocrystalline $Ag_{25}Sb_{21}Te_{54}$ thin film (x=0.98). As the composition was deviated far from the stoichiometry (x=1), the carrier concentration of the films drastically increased, but the mobility concurrently decreased. According to V. Jovovic, who supported a narrow bandgap semiconductor behavior of $AgSbTe_2$ with a longitudinal and transverse galvanomagnetic and thermomagnetic transport coefficients, the $AgSbTe_2$ was not assumed to have an equal number of electrons and holes ($n \neq p$) as non-stoichiometry between the sum of Ag-Sb and Te - resulting in two-carrier system.[3,15] This charge unbalance must be due to non-stoichiometry possibly related Ag vacancies, which can contribute to the electrical transport as a major charge carrier. The $Ag_{33}Sb_{19}Te_{48}$ (x=1.24), $Ag_{28}Sb_{22}Te_{48}$ (x=1.1), and $Ag_{15}Sb_{27}Te_{58}$ (x=0.63) thin films with Ag vacancies demonstrated the increased carrier concentration compared to that of the $Ag_{25}Sb_{21}Te_{54}$ thin film (x=0.98), which is close to intrinsic composition, but showing an opposite trend in the mobility. This reduction in the mobility is because the increase in the defect density as the dopant contributes to disorder at higher concentrations. The electrical conductivity as a combined outcome from both

components was demonstrated that the excess of Ag content in the ternary $Ag_xSb_{2-x}Te_{3-x}$ thin films had a decrease in the conductivity.

In thermoelectrics, the optimization of carrier concentration is critical for improvement of the performance of thermoelectric materials because of its interdependence on the electrical conductivity σ, the Seebeck coefficient S, and thermal conductivity κ in $zT = \sigma S^2T/\kappa$. In order to adjust the carrier concentrations of $Ag_xSb_{2-x}Te_{3-x}$ thin films for the thermoelectric applications, the level of antisite defects were controlled by synthesizing the varied composition from the stoichiometry. The composition-dependent Seebeck coefficient and power factor (P.F.) of $Ag_xSb_{2-x}Te_{3-x}$ thin films (x = 0.64, 0.98, 1.1, and 1.24) were plotted in Figure 6.5. Similar to the measurement of electrical transport properties, the measurement was conducted at room temperature in the amorphous and nanocrystalline thin films with a variation of composition. The Seebeck coefficients were positive for all films, indicating that $Ag_xSb_{2-x}Te_{3-x}$ thin films show a p-type semiconductor. Among the amorphous thin films, the peak Seebeck coefficient of ~2766 μV/K was observed in the $Ag_{25}Sb_{21}Te_{54}$ thin film (x=0.98), followed by abrupt decrease in Te- or Ag-rich thin films (Figure 6.5a). This trend is consistent with the corresponding the lowest carrier concentration in the $Ag_{25}Sb_{21}Te_{54}$ thin film (x=0.98) and increases in Te- or Ag-rich thin films (Figure 6.4c). The huge variation of Seebeck coefficient instantly affected to their P.F. values due to the correspondingly smaller variation of conductivity (Figure 6.5b). After annealing, the Seebeck coefficient from all films was reduced of 170 to 405 μV/K, which was a significant drop compared to that of amorphous thin films (980 ~ 2766 μV/K). It is

attributed to the increase in carrier concentration of the films after annealing that is inversely proportional to the Seebeck coefficient.[26] The excess of Ag content in the ternary $Ag_xSb_{2-x}Te_{3-x}$ thin films showed a clear opposite behavior of Seebeck coefficient in comparison with the conductivity. Therefore, as the Ag content increased, the Seebeck coefficient increased leading to an optimum condition found to obtain the highest P.F. in the $Ag_{25}Sb_{21}Te_{54}$ thin film (x=0.98). The high Seebeck coefficient of 303 μV/K in combination with the electrical conductivity of 21.3 S/cm yields the highest P.F. of ~196 $\mu W/mK^2$.

The summary of the published literature data of transport and thermoelectric properties using bulk $AgSbTe_2$ bulk compounds is listed in Table 6.S1.[2,3,8-14] The various efforts have been conducted to enhance the thermoelectric performance of $AgSbTe_2$, for example, the creation of two-phase mixture of the $AgSbTe_2$ system with a second phase (e.g., Ag_2Te and Sb_2Te_3) by solid-state precipitation altering the scattering mechanism of charge carriers at hetero-phase interfaces; thereby, increasing the Seebeck coefficient. For comparison of the thermoelectric characteristics in the $Ag_xSb_{2-x}Te_{3-x}$ thin films, the Seebeck coefficient was plotted as a function of the carrier concentration along with the reported data in Figure 6.6. Because there was no literature data available for 2-dimensional nanostructured $AgSbTe_2$ film, the comparison was only made with the results from the bulk alloys. As indicated, the relatively higher Seebeck coefficient values from the amorphous $Ag_xSb_{2-x}Te_{3-x}$ thin films (open symbol) along with the lower carrier concentration were reduced after annealing due to the enhanced carrier concentration of the nanocrystalline $Ag_xSb_{2-x}Te_{3-x}$ thin films (solid symbol). Based on this investigation,

the carrier concentration of the nanocrystalline $Ag_xSb_{2-x}Te_{3-x}$ thin films increased almost two-fold by the post-annealing treatment, resulting in the Seebeck coefficient ranging from 170 to 405 μV/K. Although there values are still lower than the best $AgSbTe_2$ bulk compounds, the variation of the P.F. values in the $Ag_xSb_{2-x}Te_{3-x}$ thin films with carrier concentration demonstrated that the control of chemical composition along with the crystallinity is important parameters to enhance the thermoelectric performance of ternary $Ag_xSb_{2-x}Te_{3-x}$ thin films.

6.5 Conclusion

In conclusion, we demonstrated the composition-dependent electrical transport and thermoelectric properties of ternary $Ag_xSb_{2-x}Te_{3-x}$ thin films synthesized by the simple electrodeposition method. The modulated level of carrier concentration (10^{16} ~10^{19} cm^{-3}) of the films as a function of composition and crystallinity was successfully correlated to the electrical conductivity and Seebeck coefficient. This correlation leads us to achieve the optimum power factor film. The maximum power factor of ~196 $\mu W/mK^2$ was achieved in the $Ag_{25}Sb_{21}Te_{54}$ thin film (x = 0.98) which is near the intrinsic composition of $AgSbTe_2$ (x=1) with a lowest carrier concentration of 1.62 x 10^{16} cm^{-3} and the highest Hall mobility of 8250 $cm^2/V.s$. From this observation, we confirmed that electrodeposition is a promising method to prepare the ternary $AgSbTe_2$ thin film for thermoelectric applications by adjusting the carrier concentrations with a simple and easy control over composition and crystallinity of the films.

6.6 References

[1] L.-H. Ye, K. Hoang, A. J. Freeman, S. D.Mahanti, J. He, T. M. Tritt, M. G. Kanatzidis, *First-principles study of the electronic, optical, and lattice vibrational properties of AgSbTe2.* Physical Review B, 2008. **77**(24): p. 245203.

[2] K. Wojciechowski, J. Tobola, M. Schmidt, R. Zybala, *Crystal structure, electronic and transport properties of AgSbSe 2 and AgSbTe 2.* Journal of Physics and Chemistry of Solids, 2008. **69**(11): p. 2748-2755.

[3] V. Jovovic, and J. Heremans, *Measurements of the energy band gap and valence band structure of AgSbTe2.* Physical Review B, 2008. **77**(24): p. 245204.

[4] H.A. Zayed, A.M. Ibrahim, and L.I. Soliman, *Optical absorption behaviour of AgSbTe2 thin films.* Vacuum, 1996. **47**(1): p. 49-51.

[5] J. Xu, B. Liu, Z. Song, S. Feng, B. Chen, *Crystallization and C-RAM application of Ag-doped Sb2Te3 material.* Materials Science and Engineering: B, 2006. **127**(2–3): p. 228-232.

[6] J. Tominaga, T. Kikukawa, M. Takahashi, R. T. Phillips, *Structure of the optical phase change memory alloy, Ag–V–In–Sb–Te, determined by optical spectroscopy and electron diffraction.* Journal of Applied Physics, 1997. **82**(7): p. 3214-3218.

[7] R. Wolfe, J.H. Wernick, and S.E. Haszko, *Anomalous Hall Effect in AgSbTe2.* Journal of Applied Physics, 1960. **31**(11): p. 1959-1964.

[8] E.F. Hockings, *The thermal conductivity of silver antimony telluride.* Journal of Physics and Chemistry of Solids, 1959. **10**(4): p. 341-342.

[9] R.W. Armstrong, J.W. Faust, and W.A. Tiller, *A Structural Study of the Compound AgSbTe2.* Journal of Applied Physics, 1960. **31**(11): p. 1954-1959.

[10] H. Ma, T. Su, P. Zhu, J. Guo, X. Jia, *Preparation and transport properties of AgSbTe2 by high-pressure and high-temperature.* Journal of Alloys and Compounds, 2008. **454**(1–2): p. 415-418.

[11] H. Wang, J.-F. Li, M. Zou, T. Sui, *Synthesis and transport property of AgSbTe2 as a promising thermoelectric compound.* Applied Physics Letters, 2008. **93**(20):

[12] S. N. Zhang, T. J. Zhu, S. H. Yang, C. Yu, X. B. Zhao, *Improved thermoelectric properties of AgSbTe2 based compounds with nanoscale Ag2Te in situ precipitates.* Journal of Alloys and Compounds, 2010. **499**(2): p. 215-220.

[13] J. Xu, H. Li, B. Du, X. Tang, Q. Zhang, C. Uher, *High thermoelectric figure of merit and nanostructuring in bulk AgSbTe2.* Journal of Materials Chemistry, 2010. **20**(29): p. 6138-6143.

[14] S. N. Zhang, T. J. Zhu, S. H. Yang, C. Yu, X. B. Zhao, *Phase compositions, nanoscale microstructures and thermoelectric properties in Ag2−ySbyTe1+y alloys with precipitated Sb2Te3 plates.* Acta Materialia, 2010. **58**(12): p. 4160-4169.

[15] D. Morelli, V. Jovovic, and J. Heremans, *Intrinsically Minimal Thermal Conductivity in Cubic I-V-VI2 Semiconductors.* Physical Review Letters, 2008. **101**(3): p. 035901.

[16] D. Bilc, S. D. Mahanti, E. Quarez, K.-F. Hsu, R. Pcionek, M. G. Kanatzidis, *Resonant States in the Electronic Structure of the High Performance Thermoelectrics : The Role of Ag-Sb Microstructures.* Physical Review Letters, 2004. **93**(14): p. 146403.

[17] D.L. Medlin, and J.D. Sugar, *Interfacial defect structure at Sb2Te3 precipitates in the thermoelectric compound AgSbTe2.* Scripta Materialia, 2010. **62**(6): p. 379-382.

[18] B.L. Du, H. Li, and X.F. Tang, *Enhanced thermoelectric performance in Na-doped p-type nonstoichiometric AgSbTe2 compound.* Journal of Alloys and Compounds, 2011. **509**(5): p. 2039-2043.

[19] R. Mohanraman, R. Sankar, F. C. Chou, C. H. Lee, Y.-Y. Chen, *Enhanced thermoelectric performance in Bi-doped p-type AgSbTe2 compounds.* Journal of Applied Physics, 2013. **114**(16):

[20] R. Mohanraman, R. Sankar, K. M. Boopathi, F.-C. Chou, C.-W. Chu, C.-H. Lee, Y.-Y. Chen, *Influence of In doping on the thermoelectric properties of an*

AgSbTe2 compound with enhanced figure of merit. Journal of Materials Chemistry A, 2014. **2**(8): p. 2839-2844.

[21] H. Jung, and N.V. Myung, *Electrodeposition of antimony telluride thin films from acidic nitrate-tartrate baths.* Electrochimica Acta, 2011. **56**(16): p. 5611-5615.

[22] F. Xiao, C. Hangarter, B. Yoo, Y. Rheem, K.-H. Lee, N. V. Myung, *Recent progress in electrodeposition of thermoelectric thin films and nanostructures.* Electrochimica Acta, 2008. **53**(28): p. 8103-8117.

[23] X. Feng, Y. Bongyoung, L. Kyu-Hwan, V. M. Nosang, *Electro-transport studies of electrodeposited (Bi 1− x Sb x) 2 Te 3 nanowires.* Nanotechnology, 2007. **18**(33): p. 335203.

[24] F. Xiao, B. Yoo, M. A. Ryan, K.-H. Lee, N. V. Myung, *Electrodeposition of PbTe thin films from acidic nitrate baths.* Electrochimica Acta, 2006. **52**(3): p. 1101-1107.

[25] K. Hoang, S. Mahanti, J. Salvador, M. Kanatzidis, *Atomic Ordering and Gap Formation in Ag-Sb-Based Ternary Chalcogenides.* Physical Review Letters, 2007. **99**(15): p. 156403.

[26] J. Heremans, and O.P. Hansen, *Temperature dependence of excess carrier density and thermopower in tin-doped bismuth. Pseudo-parabolic model.* Journal of Physics C: Solid State Physics, 1983. **16**(23): p. 4623.

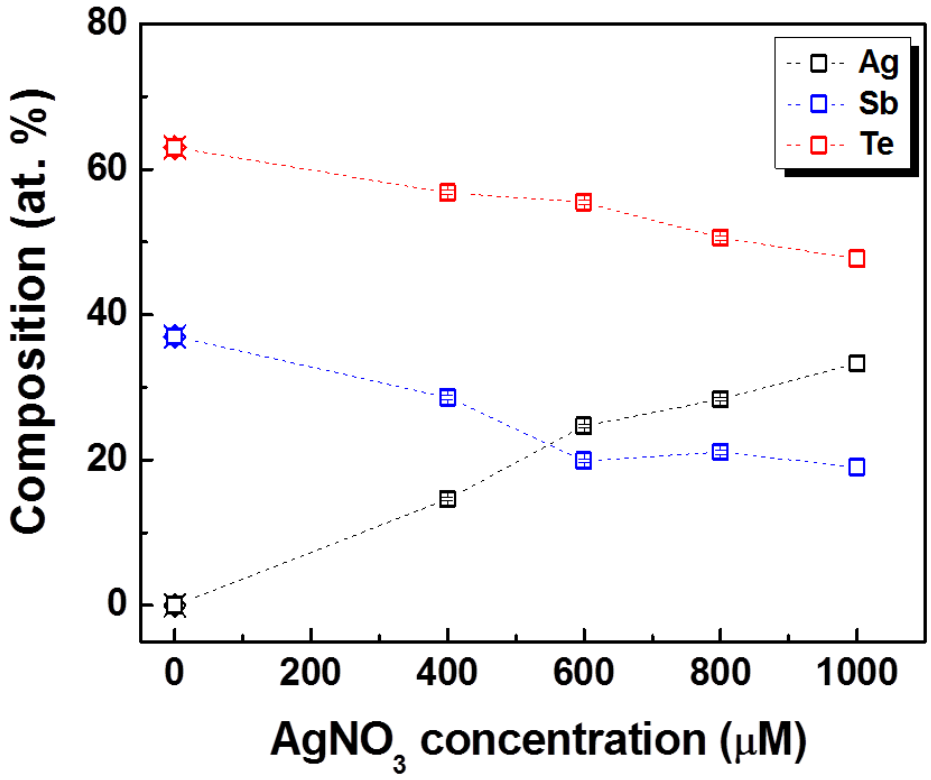

Figure 6.1 Composition of $Ag_xSb_{2-x}Te_{3-x}$ thin films as a function of $AgNO_3$ concentration in an electrolyte. Applied potential was fixed as -0.1 (V vs. SCE).

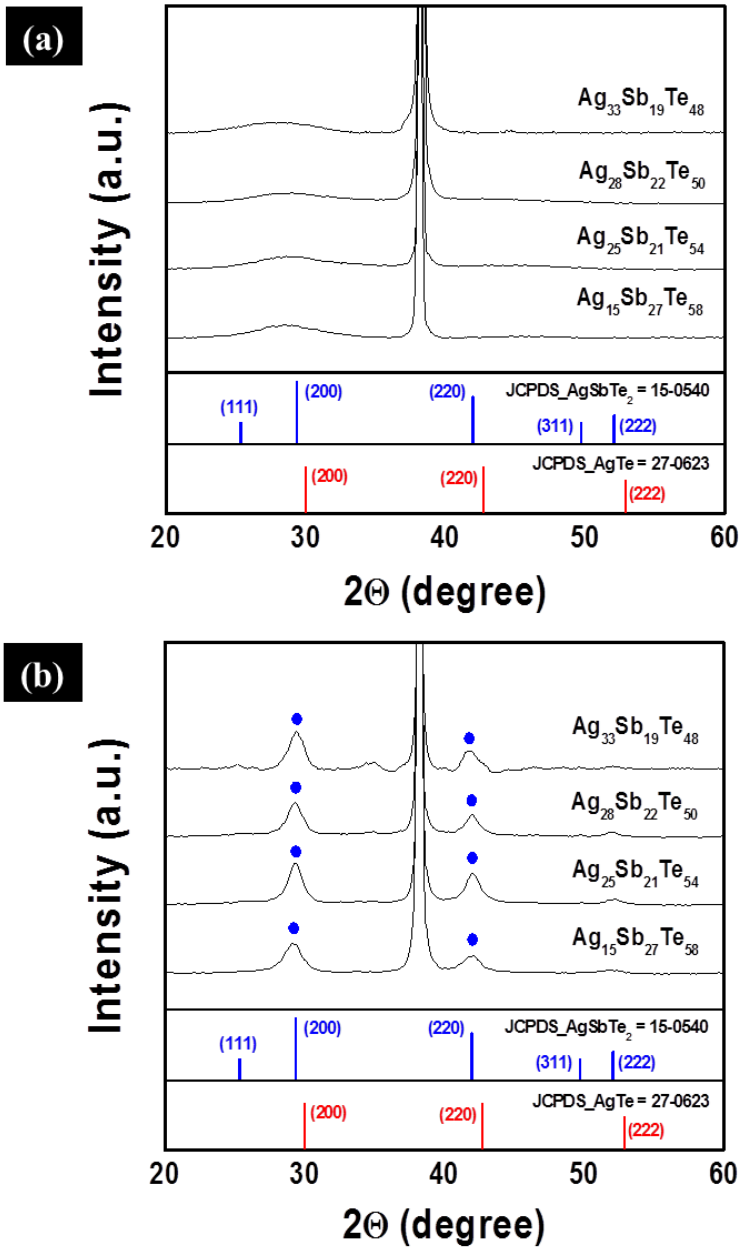

Figure 6.2 XRD analysis of $Ag_{15}Sb_{27}Te_{58}$, $Ag_{25}Sb_{21}Te_{54}$, $Ag_{28}Sb_{22}Te_{50}$, and $Ag_{33}Sb_{19}Te_{48}$ thin films as-deposited (a) and after annealing at 100 ^{o}C for 30 min (b). Symbol of solid circle refers to $AgSbTe_2$ JCPDS 15-0540.

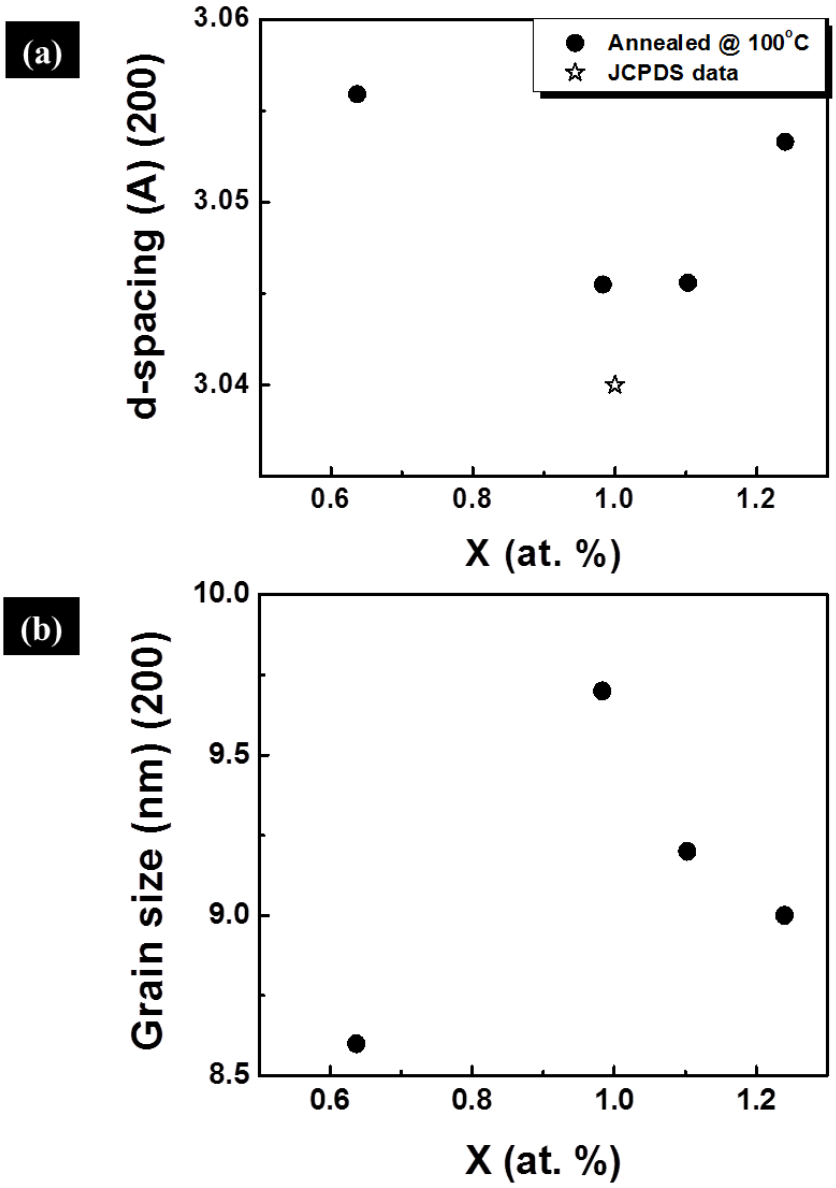

Figure 6.3 Composition-dependent d-spacing (a) and grain size (b) of $Ag_xSb_{2-x}Te_{3-y}$ thin films (x = 0.64, 0.98, 1.1, and 1.24). The results were from the XRD analysis of the films after annealing at 100 ^oC for 3 min.

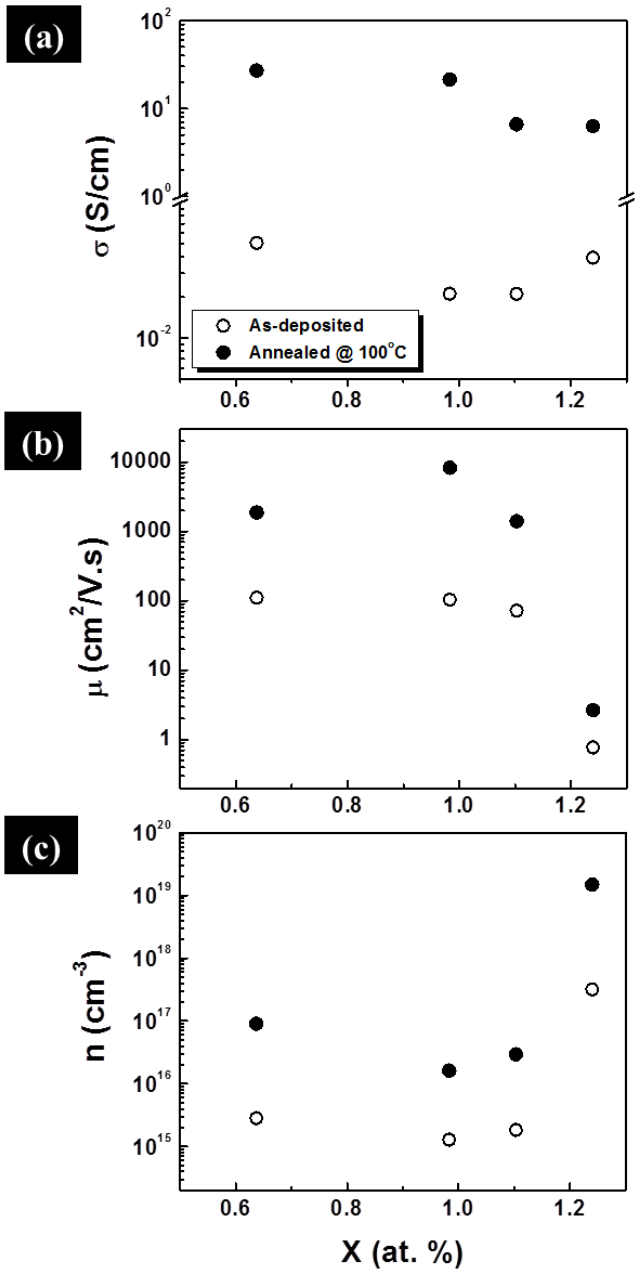

Figure 6.4 Electrical properties of $Ag_xSb_{2-x}Te_{3-x}$ thin films (x = 0.64, 0.98, 1.1, and 1.24) at room temperature. The measurement was conducted on amorphous and crystallized films to observe the crystallinity effect on their transport properties as well.

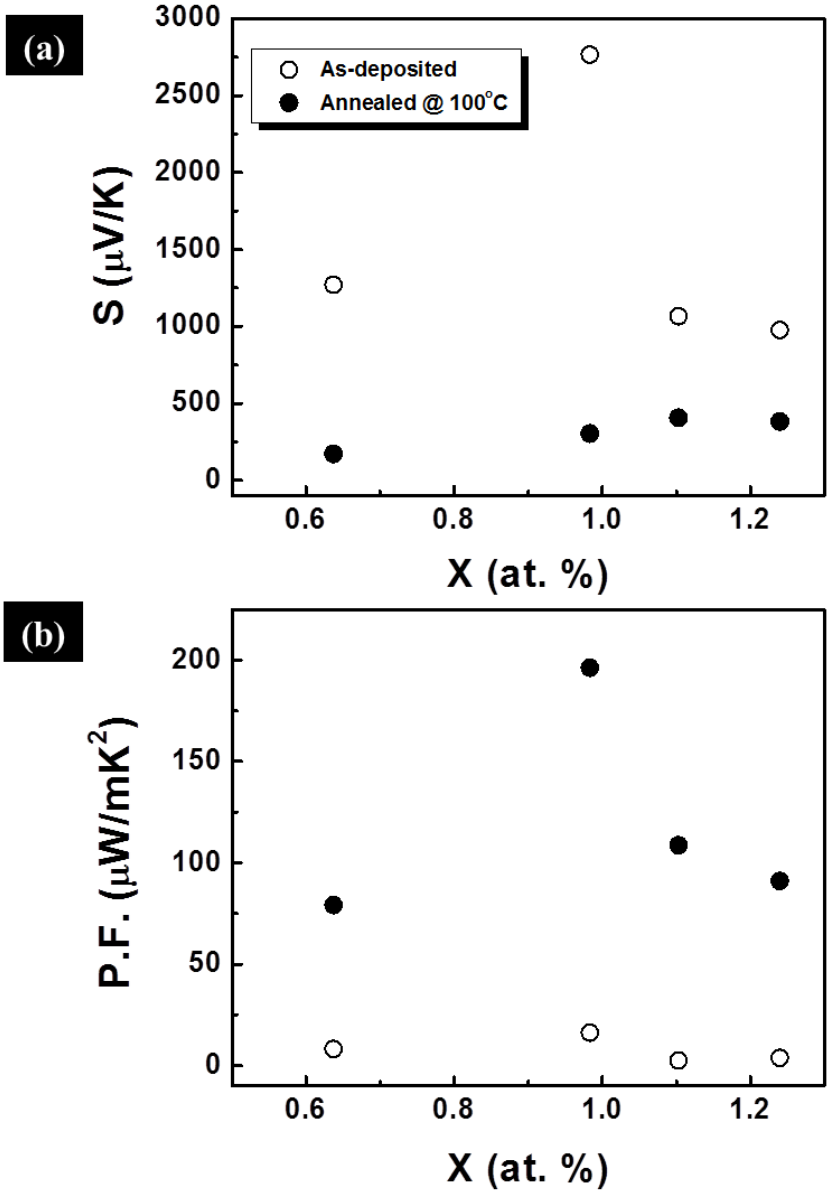

Figure 6.5 Thermoelectric properties of $Ag_xSb_{2-x}Te_{3-x}$ thin films (x = 0.64, 0.98, 1.1, and 1.24) at room temperature.

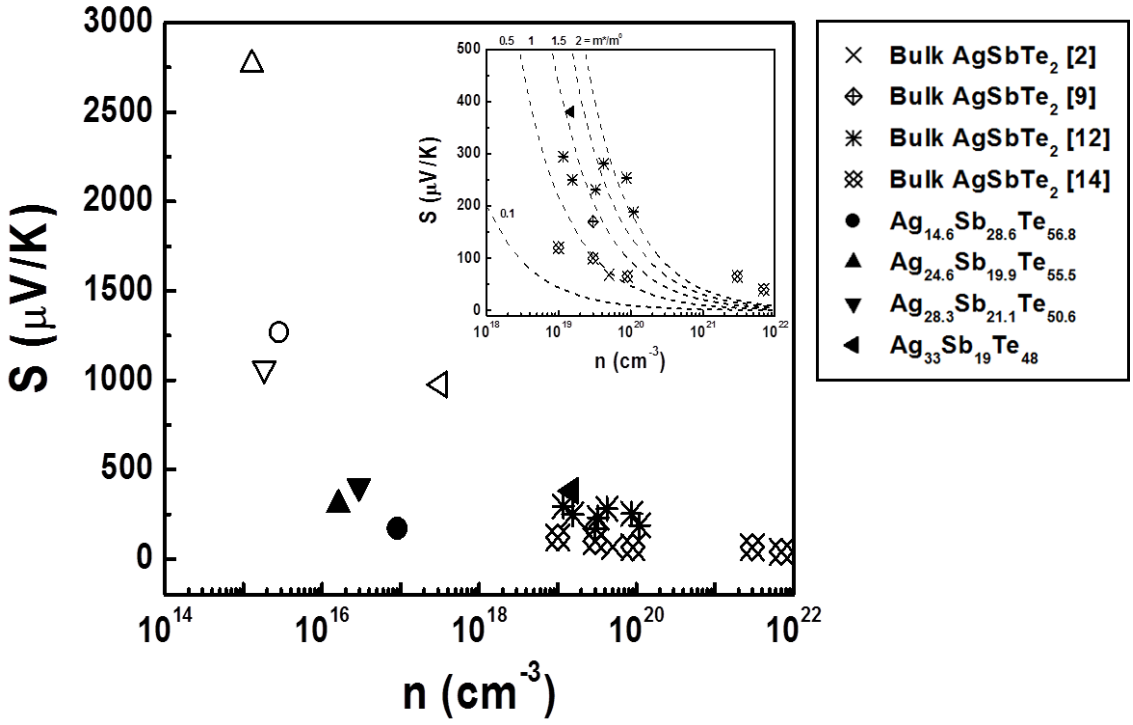

Figure 6.6 Seebeck coefficient of $Ag_xSb_{2-x}Te_{3-x}$ thin films (x=0.64, 0.98, 1.1, and 1.24) as a function of carrier concentration (Pisarenko plot) at room temperature. Open symbol refers to as-deposited films, and solid symbol refers to annealed films at 100 ^oC for 30 min. Inset refers to the zoom-in plot in the carrier concentration ranging from 10^{18} to 10^{22} cm^{-3} for clear indication.

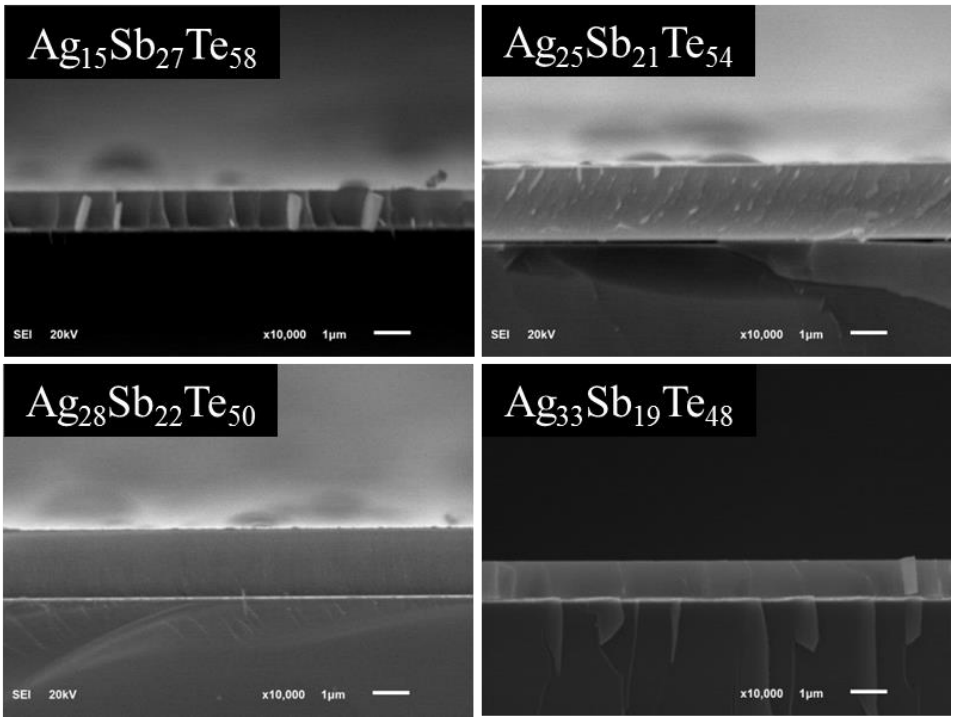

Figure 6.7 SEM images of $Ag_xSb_{2-x}Te_{3-x}$ thin films (x = 0.64, 0.98, 1.1, and 1.24).

CHAPTER 7 High Mobility-Dependent Thermoelectric Performance of Ternary BixSb2-xTey electrodeposits

7.1 Abstract

In this work, we characterized the electrical transport and thermoelectric properties of ternary bismuth antimony telluride ($Bi_xSb_{2-x}Te_y$) electrodeposits by controlling the film's chemical composition and structural properties. The composition of potentiostatically electrodeposited nanocrystalline $Bi_xSb_{2-x}Te_y$ thin films was systematically tailored by controlling the [Sb]/[Bi] ratio in the electrolytes, followed by a post-annealing process which brought about the crystallographic properties and structural defects. Room-temperature measurements of electrical conductivity, Hall mobility, carrier concentration, and Seebeck coefficient revealed that the substitution of Bi with Sb reduced the carrier concentration, whereas the mobility inversely increased. The net effect of increasing the Bi content and controlling the post annealed structural changes & defects was to increase the electrical conductivity, σ, where the increase in mobility dominated the reduction in carrier concentration such that their product increased. Judiciously, the reduction in carrier concentration was dominated in enhancing the Seebeck coefficient; therefore, the power factor was increased in ternary $Bi_xSb_{2-x}Te_y$ thin films.

7.2 Introduction

Advancements in thermoelectric materials of a high thermoelectric efficiency ($zT=\sigma S^2T/\kappa$) where S is the Seebeck coefficient, and σ is the electrical conductivity, and κ is the thermal conductivity, have been restricted by the interdependency of these parameters. Therefore, the approach to realize optimum thermoelectric materials for example, a high electrical conductivity, and Seebeck coefficient, but a low thermal conductivity has been trying to decouple the σ, S, and κ.[1] According to various theoretical and experimental studies, chalcogenides with a narrow energy band gap (E_g < 0.2 eV),[2] specifically, antimony telluride (Sb_2Te_3) and bismuth telluride (Bi_2Te_3) and the derivative materials including bismuth antimony telluride $(Bi_{0.5}Sb_{1.5})Te_3$ and bismuth telluride selenide $Bi_2(Te_{0.8}Sb_{0.2})_3$ have successfully demonstrated the best thermoelectric performance at room temperature operation. By virtue of recently advanced nanotechnology and fabrication techniques, the enhanced zT values of 2.4 in Bi_2Te_3/Sb_2Te_3 superlattice, and zT of 1.5 in nanocrystalline BiSbTe bulk alloy were recorded at room temperature.[3,4]

The bismuth antimony telluride ($Bi_xSb_{2-x}Te_y$) is anticipated as the best room temperature thermoelectric material due to the reduced thermal conductivity introduced by the substitution of Bi/Sb in the lattice structure. Especially, unique anisotropic electronic properties originated from a weak van der Waals bonding between the Te atoms along the hexagonal *c*-axis of BiSbTe allowed the additional reduction of thermal conductivity and directionality on thermoelectric performance.[5,6] Conventional synthesis techniques for the $Bi_xSb_{2-x}Te_y$ thin films such as molecular beam epitaxy

(MBE),[7] metalorganic chemical vapor deposition (MOCVD),[2,8] and solution synthesis techniques,[9,10] which are normally considered as directional crystallization techniques, however, showed the lack of control over the compositional and structural properties due to limited engineering controls. Compared to them, the electrodeposition technique provides diverse parameters to tailor the deposited film properties,-including the applied potential, electrolyte concentration, temperature, agitation, and additives. Due to these advantages, various studies have investigated the synthesis and characterization of electrical and thermoelectrical properties of the $Bi_xSb_{2-x}Te_y$ thin films. However, these finding were limited in the deposition conditions for better composition and morphology of the $Bi_xSb_{2-x}Te_y$ thin films with the expectation of improved thermoelectric performance.[11-19]

Furthermore, composition and morphology are not the only factors contributing to the thermoelectric properties, the effect of unique microstructures was also proposed in order to understand the high *zT* of the nano-grained bulk BiSbTe attributing to the increased conductivity and largely decreased thermal conductivity.[20] According to Lan *et al.*, besides the precipitates, various low dimensional defects such as point defects or impurities, dislocations, and structural modulations were commonly observed in the nano-grained bulk alloy, which were responsible for the large scattering of phonons and electrons.[20] In addition, by adjusting adequate impurities such as Bi vacancy and Te antisite defects, the carrier type of the BiSbTe solid solution exhibited the transition between n- or p-type characteristics.[10,20,21] However, only limited works have shown the systematical investigation of compositional and structural modification to optimize

the thermoelectric performance of the $Bi_xSb_{2-x}Te_y$ thin films by adjusting the carrier concentration. In this work, we synthesized the $Bi_xSb_{2-x}Te_y$ thin films by using the potentiostatic electrodeposition technique. In order to achieve the high thermoelectric performance, the electrical conductivity, mobility, and carrier concentration of the $Bi_xSb_{2-x}Te_y$ films were tailored by controlling the amount of Bi substitution in the binary SbTe film. In addition, the effect of structural improvement on the thermoelectric properties was investigated by the post annealing process, showing the drastic increase in both electrical conductivity and Seebeck coefficient, therefore, the high power factor in the $Bi_{13}Sb_{25}Te_{62}$ film.

7.3 Experimental Section

7.3.1 Synthesis of $Bi_xSb_{2-x}Te_y$ Thin Films

$Bi_xSb_{2-x}Te_y$ thin films were potentiostatically electrodeposited with a control of the concentration of electrolytes at a fixed applied potential. According to our previous works on the electrodeposition of binary Sb_xTe_{1-x} and ternary $Ag_xSb_{2-x}Te_{3-x}$ thin films, the morphology of the films was highly dependent on the applied potentials. In order to electrodeposit a uniform and dense morphology of $Bi_xSb_{2-x}Te_y$ films, we used the previous conditions for the electrodeposition of dense and uniform morphology of Sb_xTe_{1-x} films such as applied potential, deposition temperature, and agitation, and supplied the $Bi(NO_3)_35H_2O$ as an Bi^{3+} source in the electrolyte. The chemical composition of ternary $Bi_xSb_{2-x}Te_y$ thin films was tailored by controlling the $Bi(NO_3)_35H_2O$ concentration in the electrolytes. The electrolyte was prepared by

separately dissolving a 2.4 mM TeO_2 in a 1 M HNO_3 solution, a 3.6 mM Sb_2O_3 in a 33 mM L-tartaric acid solution at 60 ^oC, and 400 ~ 1000 μM $Bi(NO_3)_35H_2O$ in a deionized water. The dissolved solutions were then mixed together and deionized water was added to reach final volume of 1 L. The concentration of $Bi(NO_3)_35H_2O$ in the electrolyte was varied, including 400, 600, 800, and 1000 μM to achieve the ternary $Bi_xSb_{2-x}Te_y$ thin films with tailored composition. The working electrode was e-beam evaporated using Au (80 nm)/Ni (20 nm) films on a Si substrate, and a Pt coated titanium electrode and a saturated calomel electrode (SCE) were used as the counter and reference electrodes, respectively. A potential of -0.1 V vs. saturated calomel electrode (SCE) was applied and the electrolyte was kept at 25 ^oC and magnetically stirred at 300 rpm.

7.3.2 Sample Preparation

For electrical and thermoelectric characterization, the thin films were transferred from the Au/Ni/Si substrate to a non-conductive Torr Seal epoxy substrate (Varian Vacuum Products, Lexington, Massachusetts). The entire film was successfully transferred without cracking. The final dimensions of the sample for characterization were 1 cm^2.

7.3.3 Characterization

Morphology and composition of the synthesized $Bi_xSb_{2-x}Te_y$ thin films were analyzed by scanning electron microscopy (SEM) (Jeol, JSM-5800) and energy dispersive X-ray spectroscopy (EDS). The effect of the composition on crystallinity and crystallographic properties of the $Bi_xSb_{2-x}Te_y$ thin films were investigated as a function of the Bi content

by X-ray diffraction (XRD) (Bruker D8 ADVANCE). In addition, a post-annealing process was added to further enhance the structural properties, where the films were annealed at 200 ^{o}C for 30 min in a nitrogen atmosphere with 5 % hydrogen present. The annealing process with sequentially varied annealing temperatures ranging from 30 to 200 ^{o}C for 30 min in the nitrogen atmosphere with 5 % hydrogen was added to investigate the effect of improvement of crystallinity on electrical and thermoelectric properties. The electrical conductivity, Hall mobility, and carrier concentration of the film were investigated by a custom-made Hall measurement unit in the van der Pauw configuration with four-point probes. The Seebeck coefficient was determined by a custom-made Seebeck measurement system by plotting the measured Seebeck voltages as a function of temperature difference (<2 ^{o}C) across the sample ($S = \Delta V/\Delta T$).

7.4 Results and Discussion

7.4.1 Synthesis and Material Properties of $Bi_xSb_{2-x}Te_y$ Thin Films

Due to the high thermoelectric performance of Bi_2Te_3 based alloys near room temperature, the electrodeposition of $Bi_xSb_{2-x}Te_y$ films has been widely performed with the object of enhancing their electrical and thermoelectric properties. For this aim, the influence of the various electrodeposition parameters such as the applied potential, the [Sb]/[Bi] ratio and the type of acid added in the electrolyte was studied in correlation with morphology, composition, and crystallinity which are critical factors in determining the thermoelectric performance of the films.[15,17,18,22] The dependence of the Seebeck coefficient on the composition of the films was clearly manifested; however, the

independent control over uniform morphology was still challenged using the direct electrodeposition technique. In this work, the ternary $Bi_xSb_{2-x}Te_y$ thin films were potentiostatically electrodeposited at fixed applied potential of -0.1 V (vs. SCE). The control over the chemical composition of the film was achieved by varying the concentration of Bi^{3+} in the electrolyte from 0 to 1 mM. The composition of the ternary $Bi_xSb_{2-x}Te_y$ as a function of the Bi^{3+} concentration is indicated in Figure 7.1. As the Bi^{3+} concentration increased, the Bi content in the films linearly increased along with a decrease in the Sb content. The Te content, however, remained in the similar range of the Bi^{3+} at 0.6 mM, but it dropped slightly as the Bi^{3+} content further increased. The substitution of Bi into Sb site is expected from the underpotential deposition (UPD) reaction mechanism of the ternary Bi-Sb-Te alloy in the electrodeposition.[15] In a nitric acid system, the reduction potential of Bi and Te approach a common value that is less negative than the reduction potential of Sb is more negative than them.[17] Therefore, at the fixed concentration of $[Sb_2(C_4H_2O_6)_2]^{2-}$ and $HTeO_2^+$, the increase of the Bi^{3+} concentration in the electrolyte provided the competitive reduction of Bi with Te^{IV+} ($Te^0 \rightarrow T^{IV+} + e^-$) instead of Sb. Including the $(Bi_{0.25}Sb_{0.75})_2Te_3$, which is known as the best composition for optimum thermoelectric performance in bulk,[3] its slightly deviated compositions (i.e., $Bi_{13}Sb_{25}Te_{62}$, $Bi_{18}Sb_{28}Te_{54}$, and $Bi_{22}Sb_{24}Te_{54}$) were achieved where we can expect to have an ability to tailor the carrier concentration in the films.[10] The morphology of the as-deposited films was confirmed by SEM analysis as shown in Figure 7.2. As indicated in the cross-section views (insets in the Figure 7.2), four films had a thickness of 1 ~ 2 μm with dense structures. The surface morphology of the

electrodeposited $Bi_xSb_{2-x}Te_y$ films was shown to consist of nano-grains. Specifically, micron-scale grain clusters were observed on the surface of the $Bi_{10}Sb_{30}Te_{60}$ film. This heterogeneous grain growth of the $Bi_xSb_{2-x}Te_y$ films with the rough surface is consistent with the reported results from the potentiostatically electrodeposited $(Bi_{0.25}Sb_{0.75})_2Te_3$ thin films in the nitric acid bath.[16] A comprehensive study on the crystallinity and crystal structure of the electrodeposited $Bi_xSb_{2-x}Te_y$ films was conducted by XRD analysis. The improvement of crystallographic properties of the films was expected by annealing the as-deposited films at 200 ^oC for 30 min in the nitrogen atmosphere with 5 % hydrogen. The crystallinity of as-deposited films in Figure 7.3a indicated that the initial crystallinity differed as a function of composition of the films. The define peaks were matched with a reflection peak of R-3m $(Bi_{0.25}Sb_{0.75})_2Te_3$ phase (JCPDS card 49-1713) corresponding to (0 1 5) and (1 1 0). The values of the full width at half-maximum (FWHM) of (0 1 5) peak and the calculated grain size by the Scherrer equation are shown in Figure 7.4. As noticed, the larger FWHM values, indicating poor crystallization, were obtained in the films with less Bi contents. In fact, this relationship is consistent with the reported observation where the crystallinity of the $(Bi_xSb_{1-x})_2Te_3$ films was influenced by the [Sb]/[Bi] ratio in the electrolyte.[15] According to them, the better crystallinity of the films was investigated as the [Sb]/[Bi] ratio decreased. Correspondingly, the FWHM and grain size of the as-deposited films increased as the [Sb]/[Bi] ratio decreased in our electrolytes (Table 7.S1). The improved crystallinity of the entire films after the post-annealing process was confirmed with the increased grain size and decreased FWHM values. Interestingly, the degree of the improvement in the crystallinity was dependent on

the composition of the films. As noticed Figure 7.4a, the significant changes of the FWHM were observed in the $Bi_{10}Sb_{30}Te_{60}$ and $Bi_{13}Sb_{25}Te_{62}$ which had initially almost amorphous phases along with the large changes in the grain sizes. In addition, the precipitation of Sb was observed in the $Bi_{10}Sb_{30}Te_{60}$ film. On the other hand, the $Bi_{18}Sb_{28}Te_{54}$ and $Bi_{22}Sb_{24}Te_{54}$ thin films, which formed the nanocrystalline in the as-deposited state, indicated no significant changes in the FWHM, thus, grain size remained the same after annealing at 200 ^{o}C.

7.4.2 Electrical and Thermoelectric Properties of $Bi_xSb_{2-x}Te_y$ Thin Films

The electrical conductivity, Hall mobility, and carrier concentration of the $Bi_xSb_{2-x}Te_y$ thin films were investigated as a function of Bi content in Figure 7.5. Measurements were conducted before and after the post-annealing process. Figure 7.5a shows the electrical conductivity of the as-deposited (symbol of open circle) and annealed (symbol of solid circle) films as a function of Bi content. Compared to the conductivity (3.9×10^{-2} S/cm) of the as-deposited binary $Sb_{37}Te_{63}$ thin film, the conductivity of as-deposited $B_xSb_{2-x}Te_y$ films continuously raised over one-order of magnitude as the Bi content increased. Contrary to the conductivity, the carrier concentration of the as-deposited films drastically decreased almost three-order of magnitude at the Bi content of 10 at. % in the film, followed by a slight rally and retained as the Bi content increased. The change of the Hall mobility showed the opposite trend to that of carrier concentration. The significant increase in the mobility at the Bi content of 10 at. % followed by small dip and rose up as the Bi content increased explained that the electrical conductivity of the

$B_xSb_{2-x}Te_y$ films were dominantly affected by the change of the mobility. After annealing at 200 ^oC for 30 min, the enhanced values of electrical conductivity were observed in all of the films; however, there was the difference in the degree of the changes. As noticed, the highest conductivity of 250 S/cm was observed in the $Bi_{13}Sb_{25}Te_{62}$ film followed by the second highest conductivity of 225 S/cm in the $Bi_{10}Sb_{30}Te_{60}$ film, which were higher than the of Bi undoped binary $S_{37}Te_{63}$ film (164 S/cm). The conductivity ratio of the tree films varied nearly a thousand-fold as compared to their as-deposited values. On the other hand, the changes of the conductivity of the $Bi_{18}Sb_{28}Te_{54}$ and $Bi_{22}Sb_{24}Te_{54}$ films after annealing remained ten-fold. Such variation in the electrical conductivity changes is related to their crystal structure changes. As represented in the grain size changes (Figure 7.4b), the films with large changes in the grain size after annealing also demonstrated the significantly increased electrical conductivities. Moreover, the carrier concentration of the annealed films also clearly showed the composition-dependent relationship. Compared to the binary $Sb_{37}Te_{63}$, the monotonically decreased carrier concentration as the Bi content increased up to Bi content of 18 at. % and maintained is corresponding to the reduction of the carrier concentration of $Bi_{10.8}Sb_{29.2}Te_{60}$ and $Sb_{9.2}Sb_{30.8}Te_{60}$ films compared to that of Sb_2Te_3 and Bi_2Te_3 synthesized by metaloganic chemical vapor deposition (MOCVD) technique.[2] It is known that Sb_xTe_{1-x} and $Bi_xSb_{2-x}Te_y$ have the same crystal structures (R-3m) with the substation of Bi into the Sb site. Moreover, the antisite defect expected in the Sb_xTe_{1-x} system due to the similar electron affinity between Sb and Te atoms suggests that the optimization of the thermoelectric performance of BiSbTe system can be approached by adjusting the Bi content. The substitution of Bi into

the Sb-Te structures enables to form the Bi-Te structures, resulting in the reduction of the acceptors.[10] Moreover, the increased probability for the formation of Bi-Te bindings also allows creating a Te antisite in the system which creates an electron.[20,23] This competitive formation of negative carrier concentration is possible to compensate the background free holes in the binary $Sb_{37}Te_{63}$ films, which is consistent with the significantly low values of the carrier concentration. Furthermore, as the Bi content increased, the increased Hall mobility was also corresponded to the reduction of the carrier concentrations as well. Therefore, in order to optimize the electrical transport properties of the ternary $B_xSb_{2-x}Te_y$ films for the best thermoelectric performance, it is conclude that the adjusting the composition is the dominant factor to control because of the inevitable bipolar effect.

The clear transition of carrier type from p-type to n-type was investigated by measuring the Seebeck coefficient of (symbol of open circle) and annealed (symbol of solid circle) $B_xSb_{2-x}Te_y$ films as a function of Bi content in Figure 7.6a. Among the as-deposited $B_xSb_{2-x}Te_y$ films, only the $Bi_{10}Sb_{30}Te_{60}$ film showed the positive Seebeck coefficient which representing its p-type characteristics. Compared to the binary $Sb_{37}Te_{63}$ film, however, its value was significantly higher because of the reduced carrier concentration, corresponding to Mott relationship. Meanwhile, as the Bi content increased, the measured Seebeck coefficient values became negative and decreased down to -160 μV/K in the $Bi_{22}Sb_{24}Te_{54}$ film. This value is well matched with the reported Seebeck coefficient of -149 μV/K in the nanocrystalline $Bi_{30}Sb_{10}Te_{60}$ film.[10] Based on the measurements the power factor (P.F. = σS^2) of the as-deposited $B_xSb_{2-x}Te_y$ films plotted in Figure 7.6a

represented that none of the films showed the better performance that the binary $Sb_{37}Te_{63}$ film. After annealing, however, the composition showing the carrier type transition was shifted to the Bi content of 22 at. %. Except for the $Bi_{22}Sb_{24}Te_{54}$ film, the $Bi_{10}Sb_{30}Te_{60}$, $Bi_{13}Sb_{25}Te_{62}$, and $Bi_{18}Sb_{28}Te_{54}$ films represented positive Seebeck coefficients showing that they are p-type semiconducting behaviors. From this observation, it is concluded that the reduction and formation of the various defects, which are responsible for the major charge carrier to contribute the transport of the films, are highly dependent not only on the chemical composition but also on the crystallinity of the $B_xSb_{2-x}Te_y$ films. This investigation can be applied to understand such variation of the reported thermoelectric performance and n-or p-type of $B_xSb_{2-x}Te_y$ system using various synthesis techniques. In our system, the highest P.F. was obtained from the nanocrystalline $Bi_{13}Sb_{25}Te_{62}$ film as for the p-type thermoelectric material at room temperature, which was the result of the highest conductivity obtained by adjusting the Hall mobility with reduced carrier concentration, leading to the highest Seebeck coefficient.

Detail characterization on the transition behavior of the $Bi_{13}Sb_{25}Te_{62}$ film was conducted by measuring the electrical conductivity and Seebeck coefficient as a function of the annealing temperature. The annealing temperature was varied from room temperature to 200 ^oC and maintained for 30 min for each step. As shown in Figure 7.7, the negative Seebeck coefficient was maintained by annealed at 40 ^oC. After annealing at 50 ^oC, however, the measured Seebeck coefficient started showing the positive values in addition to the drastic changes in the electrical conductivities. This transition behavior is a response of the crystallinity changes of the films after annealing. Due to the

enhancement of both the Seebeck coefficient and conductivity, the P.F. of the films also increased as a function of the annealing temperature. After the drastic change at 80 ^{o}C, the P.F. of the $Bi_{13}Sb_{25}Te_{62}$ film continuously increased up to 490 $\mu W/mK^2$ after annealed at 200 ^{o}C which is a comparable value to some results from bulk $Bi_{10}Sb_{30}Te_{60}$ materials.

7.5 Conclusion

In conclusion, we demonstrated an effective approach to optimize the electrical and thermoelectric property of electrodeposited ternary $Bi_xSb_{2-x}Te_y$ thin films by tailoring their chemical composition and the crystallinity. The substitution of Sb with Bi from the binary $Sb_{37}Te_{63}$ thin film systematically revealed the role of Bi in the electrical transport properties of ternary system. Resultantly, the highest conductivity was achieved in the nanocrystalline $Bi_{13}Sb_{25}Te_{62}$ film which was mainly due to the improved mobility induced by the significantly reduced carrier concentration. Such reduction of the carrier concentration was explained by the compensation of the antisite defects due to the addition of Bi. This behavior was also supported by observation of the carrier type transition indicated by the Seebeck coefficient.

7.6 References

[1] G.J. Snyder, and E.S. Toberer, *Complex thermoelectric materials.* Nat Mater, 2008. **7**(2): p. 105-114.

[2] A. Boulouz, S. Chakraborty, A. Giani, F. P. Delannoy, A. Boyer, Schumann, J. ,*Transport properties of V–VI semiconducting thermoelectric BiSbTe alloy thin films and their application to micromodule Peltier devices.* Journal of Applied Physics, 2001. **89**(9): p. 5009-5014.

[3] R. Venkatasubramanian, E. Siivola, T. Colpitts, B. O'Quinn, *Thin-film thermoelectric devices with high room-temperature figures of merit.* Nature, 2001. **413**(6856): p. 597-602.

[4] B. Poudel, Q. Hao, Y. Ma, Y. Lan, A. Minnich, B. Yu, X. Yan, D. Wang, A. Muto, D. Vashaee, X. Chen, J. Liu, M. S. Dresselhaus, G. Chen, Z. Ren, *High-Thermoelectric Performance of Nanostructured Bismuth Antimony Telluride Bulk Alloys.* Science, 2008. **320**(5876): p. 634-638.

[5] S. Cho, Y. Kim, A. DiVenere, G. K. Wong, J. B. Ketterson, J. R. Meyer, *Antisite defects of Bi2Te3 thin films.* Applied Physics Letters, 1999. **75**(10): p. 1401-1403.

[6] D. L. Partin, J. Heremans, D. T. Morelli, C. M. Thrush, C. H. Olk, T. A. Perry, *Growth and characterization of epitaxial bismuth films.* Physical Review B, 1988. **38**(6): p. 3818-3824.

[7] A. Boyer, and E. Cissé, *Properties of thin film thermoelectric materials: application to sensors using the Seebeck effect.* Materials Science and Engineering: B, 1992. **13**(2): p. 103-111.

[8] A. Mzerd, B. Aboulfarah, A. Giani, A. Boyer, *Elaboration and characterization of MOCVD (Bi1- x Sb x)2 Te3 thin films.* Journal of Materials Science, 2006. **41**(5): p. 1659-1662.

[9] M. Scheele, N.Oeschler, I. Veremchuk, K. G. Reinsberg, A. M. Kreuziger, A. Kornowski, J. Broekaert, C. Klinke, H. Weller, *ZT Enhancement in Solution-Grown Sb(2-x)BixTe3 Nanoplatelets.* Acs Nano, 2010. **4**(7): p. 4283-4291.

[10] Y. Zhao, J. S. Dyck, B. M. Hernandez, C. Burda, *Enhancing Thermoelectric Performance of Ternary Nanocrystals through Adjusting Carrier Concentration.* Journal of the American Chemical Society, 2010. **132**(14): p. 4982-4983.

[11] P. Magri, C. Boulanger, and J.M. Lecuire, *Synthesis, properties and performances of electrodeposited bismuth telluride films.* Journal of Materials Chemistry, 1996. **6**(5): p. 773-779.

[12] A. L. Prieto, M. S. Sander, M. Martin-Gonzalez, R. Gronsky, T. Sands, A. M. Stacy, *Electrodeposition of ordered Bi2Te3 nanowire arrays.* Journal of the American Chemical Society, 2001. **123**(29): p. 7160-7161.

[13] M. Nedelcu, M. Sima, A. S. Manea, M. F. Lazarescu, R. V. Ghita, F. Craciunoiu, T. Visan, *Bi2-xSbxTe3 thick thermoelectric films obtained by electrodeposition from hydrochloric acid solutions.* Journal of Optoelectronics and Advanced Materials, 2002. **4**(1): p. 99-106.

[14] M. S. Sander, R. Gronsky, T. Sands, A. M. Stacy, *Structure of bismuth telluride nanowire arrays fabricated by electrodeposition into porous anodic alumina templates.* Chemistry of Materials, 2003. **15**(1): p. 335-339.

[15] D. Del Frari, S. Diliberto, N. Stein, C. Boulanger, J.-M. Lecuire, *Comparative study of the electrochemical preparation of Bi2Te3, Sb2Te3, and (BixSb1−x)2Te3 films.* Thin Solid Films, 2005. **483**(1–2): p. 44-49.

[16] D. Frari, S. Diliberto, N. Stein, C. Boulanger, J.-M. Lecuire, *Pulsed electrodeposition of (Bi1-xSbx)2Te3 thermoelectric thin films.* Journal of Applied Electrochemistry, 2006. **36**(4): p. 449-454.

[17] F. Li, and W. Wang, *Electrodeposition of BixSb2−xTey thermoelectric thin films from nitric acid and hydrochloric acid systems.* Applied Surface Science, 2009. **255**(7): p. 4225-4231.

[18] F.H. Li, and W. Wang, *Electrodeposition of BixSb2-xTey thermoelectric thin films from nitric acid and hydrochloric acid systems.* Applied Surface Science, 2009. **255**(7): p. 4225-4231.

[19] C. Schumacher, K. G. Reinsberg, R. Rostek, L. Akinsinde, S. Baessler, S. Zastrow, G. Rampelberg, P. Woias, C. Detavernier, J. A. C. Broekaert, J. Bachmann, K. Nielsch, *Optimizations of Pulsed Plated p and n-type Bi2Te3-Based Ternary Compounds by Annealing in Different Ambient Atmospheres.* Advanced Energy Materials, 2013. **3**(1): p. 95-104.

[20] Y. Lan, B. Poudel, Y. Ma, D. Wang, M. S. Dresselhaus, G. Chen, Z. Ren, *Structure Study of Bulk Nanograined Thermoelectric Bismuth Antimony Telluride.* Nano Letters, 2009. **9**(4): p. 1419-1422.

[21] R. Martin-Lopez, B. Lenoir, A. Dauscher, H. Scherrer, S. Scherrer, *Preparation of n-type Bi–Sb–Te thermoelectric material by mechanical alloying.* Solid State Communications, 1998. **108**(5): p. 285-288.

[22] F.H. Li, F.L. Jia, and W. Wang, *Studies of the electrochemical reduction processes of Bi3+, HTeO2+ and their mixtures.* Applied Surface Science, 2009. **255**(16): p. 7394-7402.

[23] P. Pecheur, and G. Toussaint, *Tight-binding studies of crystal stability and defects in Bi2Te3.* Journal of Physics and Chemistry of Solids, 1994. **55**(4): p. 327-338.

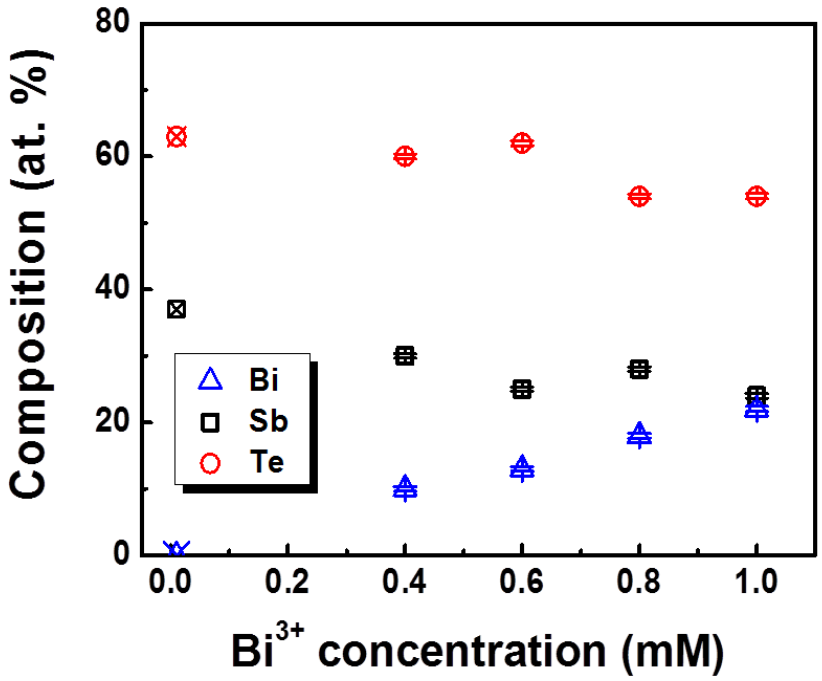

Figure 7.1 Effect of Bi^{3+} concentration on the composition of the $Bi_xSb_{2-x}Te_y$ electrodeposits.

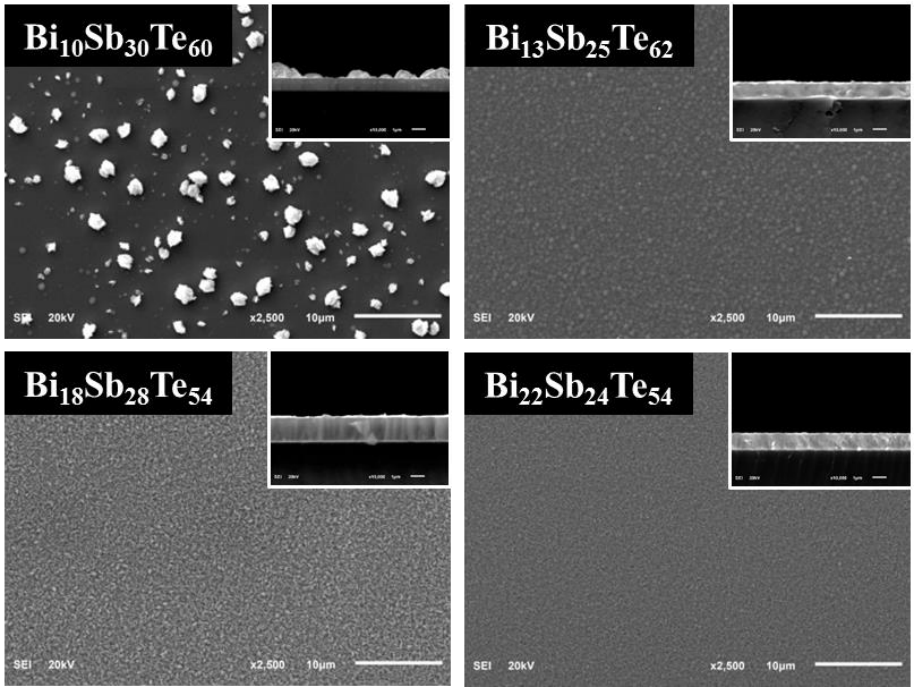

Figure 7.2 SEM of as-deposited $Bi_{10}Sb_{30}Te_{60}$, $Bi_{13}Sb_{25}Te_{62}$, $Bi_{18}Sb_{28}Te_{54}$, and $Bi_{22}Sb_{24}Te_{54}$ thin films.

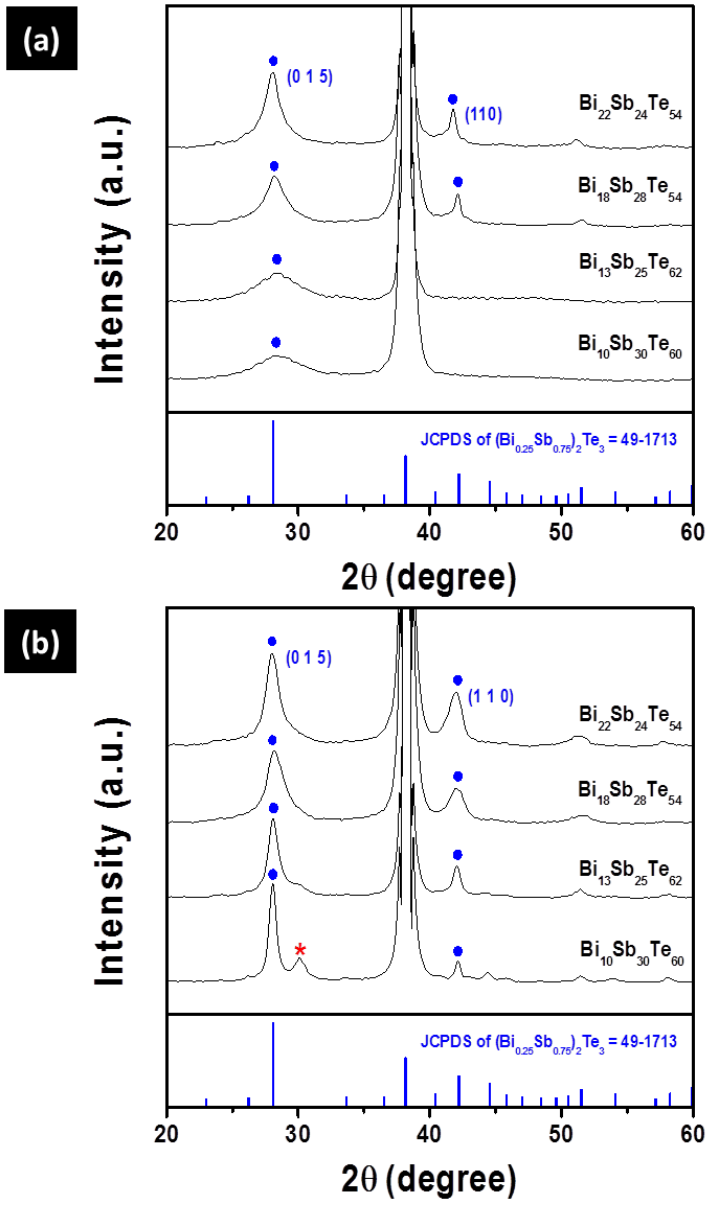

Figure 7.3 XRD analysis of as-deposited (a) and after annealed at 200 ^{o}C for 30 min in 5 % H_2/ 95 % N_2 $Bi_{10}Sb_{30}Te_{60}$, $Bi_{13}Sb_{25}Te_{62}$, $Bi_{18}Sb_{28}Te_{54}$, and $Bi_{22}Sb_{24}Te_{54}$ thin films.

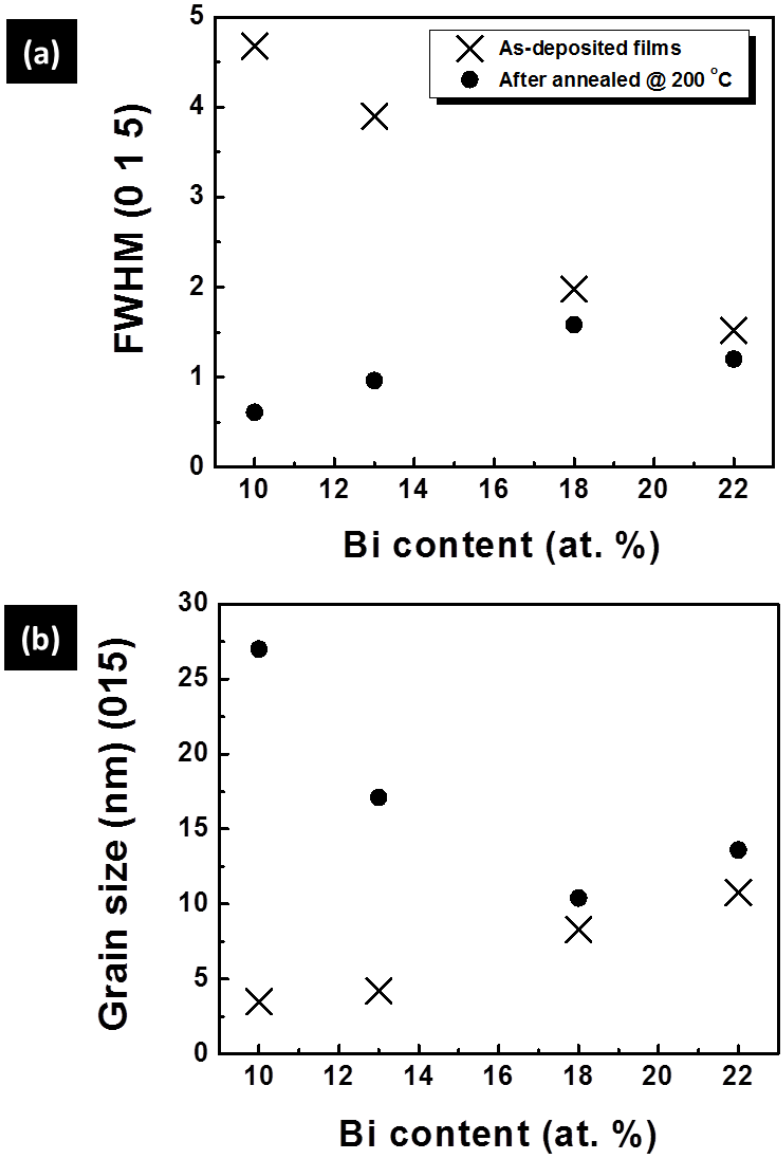

Figure 7.4 Composition-dependent FWHM (a) and grain size (b) of $Bi_xSb_{2-x}Te_y$ thin films.

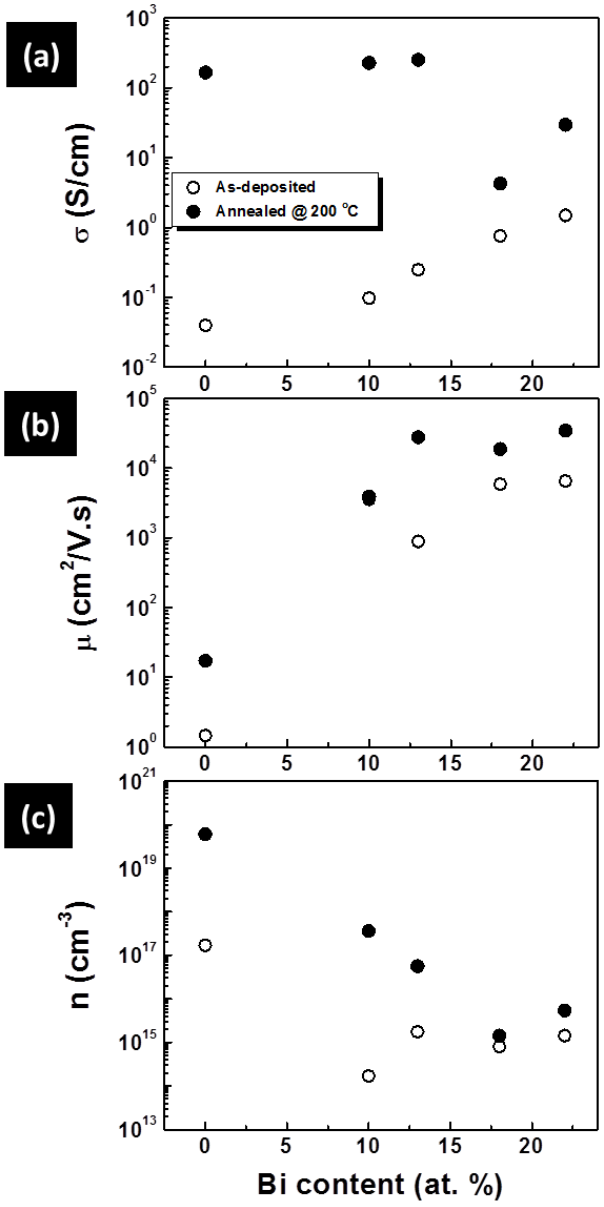

Figure 7.5 Electrical conductivity (a), Hall mobility (b), and carrier concentration (c) of $Sb_{37}Te_{63}$, $Bi_{10}Sb_{30}Te_{60}$, $Bi_{13}Sb_{25}Te_{62}$, $Bi_{18}Sb_{28}Te_{54}$, and $Bi_{22}Sb_{24}Te_{54}$ thin films as a function of Bi content. Measurement was conducted in room temperature.

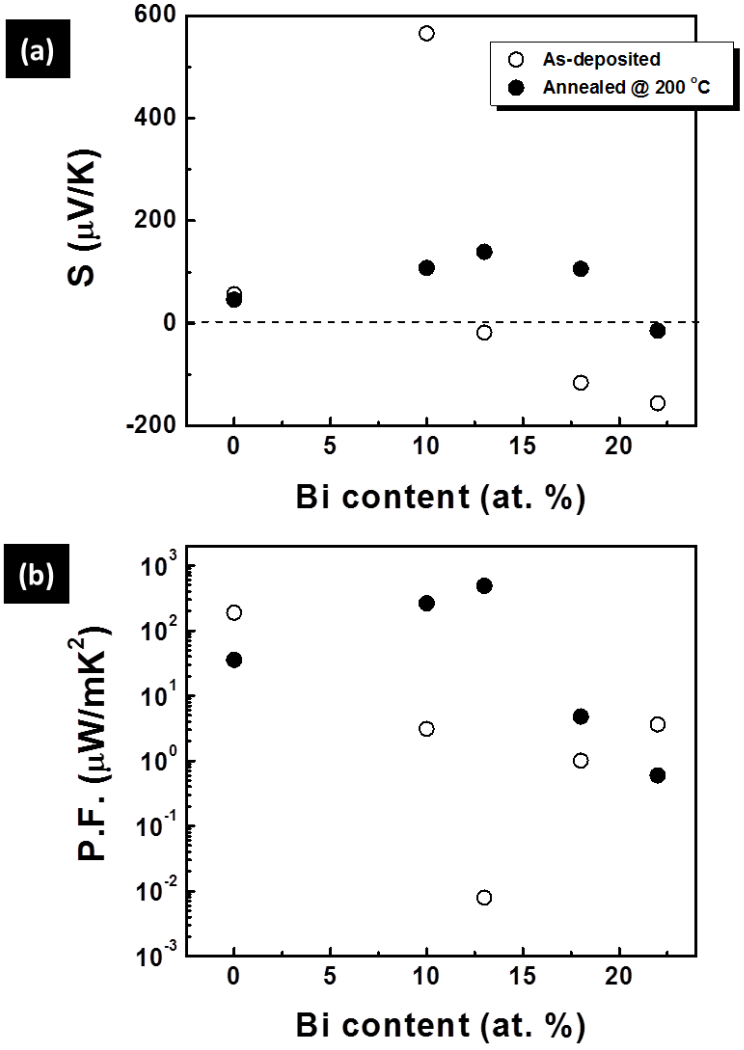

Figure 7.6 Seebeck coefficient (a) and Power factor (P.F.) of $Bi_{10}Sb_{30}Te_{60}$, $Bi_{13}Sb_{25}Te_{62}$, $Bi_{18}Sb_{28}Te_{54}$, and $Bi_{22}Sb_{24}Te_{54}$ thin films as a function of Bi content. Measurement was conducted in room temperature.

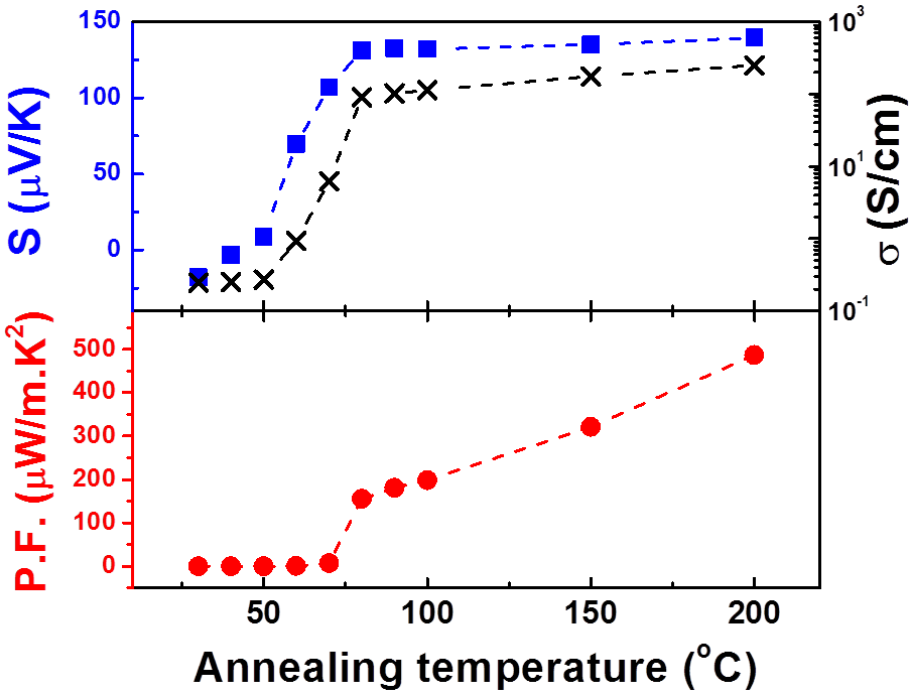

Figure 7.7 Thermoelectric properties of $Bi_{13}Sb_{25}Te_{62}$ thin films as a function of annealing temperature. Measurement was conducted in room temperature.

CHAPTER 8 Conclusion

This work demonstrated the synthesis and characterization of one- and two-dimensional chalcogenide nanostructures for thermoelectric applications.

Chapter 2 demonstrated the enhancement of thermoelectric properties by creating γ-SbTe/Sb_2Te_3 nanocomposite film, where γ-SbTe nanoinclusions are embedded in a nanocrystalline Sb_2Te_3 matrix. The two-phase nanocomposite was formed via solid-state phase transition using an amorphous Sb_2Te_3 electrodeposits as the starting materials. The formation of the γ-SbTe is attributed to the different enthalpy of mixing for the bonding structures available in the Sb-Te system. Measurement of electrical and thermoelectrical properties as a function of annealing temperature revealed that the two-phase system provided the carrier energy filtering effect at the interfaces between two phases, leading to enhanced Seebeck coefficient without affecting its electrical transport properties. The band bending at the two-phase interfaces was indirectly manifested by measuring their difference in the valence band, advocating the possibility of a strong energy-dependent charge scattering to the enhanced Seebeck coefficient.

Chapter 3 described the investigation of the role of the energy filtering effect to optimize the thermoelectric performance of the nanocrystalline Sb_2Te_3 thin film in aspect of a tailor of the energy barrier height. The interfacial energy barrier scatterings in the nanocrystalline Sb_2Te_3 electrodeposits were simply controlled by adjusing the grain size at given carrier concentration in addition to the incorpolation of the γ-SbTe and Te phases. The effect of low energy carrier filtering at the interfaces with the different types of the

barrier height was indicated by showing the enhanced Seebeck coefficient compared to the single-phase nanocrystalline Sb_2Te_3 without significant changes on the given carrier concentration. A facile but high precision composition-controlled electrodeposition technique is selected to synthesize various compositions of amorphous Sb-Te solid solutions which are readily crystallized by post annealing treatments selectively forming thermodynamically favored phases, including single-phase nanocrystalline Sb_2Te_3 and crystalline nanocomposites Te/Sb_2Te_3 or γ-$SbTe/Sb_2Te_3$. Solution composition and post-annealing profiles are used to control the single-phase grain size, thereby the grain-boundary potential-barrier, at a given carrier concentration as well as the nature of the embedded second-phase. Electrical and thermoelectrical properties are measured and correlated with the properties of each film, where an enhanced Seebeck coefficient at a given carrier concentration is interpreted to imply that an energy-dependent carrier filtering effect is at play.

Chapter 4 demonstrated the thermoelectric and transport properties of electrodeposited Ag-doped Sb_xTe_y amorphous films which were correlated and optimized with respect to chemical composition and their final crystallographic properties. A post-annealing process induced the final solid state amorphous-crystalline phase transition. Under the phase transition, the formation of the various phases ranged from the predominant metastable γ-SbTe phase to the rhombohedral Sb_2Te_3 phase as the Te content was increased from 58 and 67.1 at. %. The change in the crystal's crystallographic orientation was also determined and correlated with the film's thermoelectric properties. Moreover, the Ag atoms incorporated into the Sb_xTe_y thin

films acted as an acceptor dopant and increased the predominant hole carrier concentration. Among the various compositions, the optimized power factor of ~1870 $\mu W/mK^2$ was observed in the $Ag_{1.5}Sb_{31.5}Te_{67.1}$ thin film remained a single-phase of rhombohedral Sb_2Te_3 with a preferred orientation toward (110) with the highest conductivity of 1.82 x 10^3 S/cm.

Chapter 5 indicated the effect of the composition and microstructure changes on the electrical and thermoelectric properties of antimony telluride (Sb_xTe_y) nanowires. The template-directed electrodeposition was utilized to synthesize Sb_xTe_y nanowires where the composition of the nanowires was modulated by adjusting electrodeposition conditions. Material properties of the nanowires, such as crystallinity, grain size, and phase segregation as a function of the Sb content, were tailored by a post-annealing process. The tailored material properties successfully altered the electrical and thermoelectric properties of the nanowires. Composition-dependent phase transition behavior of the nanowires was investigated by measuring their resistivity changes where the resistivity variation ratio ($\Delta\rho/\rho_0$) was highly dependent on the Sb content in the nanowires. The carrier concentration of Sb_xTe_y nanowires decreased from ~10^{19} to ~10^{18} cm^{-3} as their grain size increased due to the reduced antisite defects. Temperature-dependent electrical properties of the amorphous and crystalline nanowires were also characterized before/after the phase transition. The highest thermopower of 318 $\mu V/K$ at the carrier concentration of 1.1 x 10^{19} cm^{-3} was observed in the Te segregated $Sb_{32}Te_{68}$.

Chapter 6 described the composition-dependent electrical transport and thermoelectric properties of ternary $Ag_xSb_{2-x}Te_{3-x}$ thin films synthesized by the simple

electrodeposition method. The modulated level of carrier concentration (10^{16} ~10^{19} cm^{-3}) of the films as a function of composition and crystallinity was successfully correlated to the electrical conductivity and Seebeck coefficient. This correlation leads us to achieve the optimum power factor film. The maximum power factor of ~196 $\mu W/mK^2$ was achieved in the $Ag_{25}Sb_{21}Te_{54}$ thin film (x=0.98) which is near the intrinsic composition of $AgSbTe_2$ (x=1) with a lowest carrier concentration of 1.62 x 10^{16} cm^{-3} and the highest Hall mobility of 8250 $cm^2/V.s$. From this observation, we confirmed that electrodeposition is a promising method to prepare the ternary $AgSbTe_2$ thin film for thermoelectric applications by adjusting the carrier concentrations with a simple and easy control over composition and crystallinity of the films.

Chapter 7 demonstrated an effective approach to optimize the electrical and thermoelectric property of electrodeposited ternary $Bi_xSb_{2-x}Te_y$ thin films by tailoring their chemical composition and the crystallinity. The substitution of Sb with Bi from the binary $Sb_{37}Te_{63}$ thin film systematically revealed the role of Bi in the electrical transport properties of ternary system. Resultantly, the highest conductivity was achieved in the nanocrystalline $Bi_{13}Sb_{25}Te_{62}$ film which was mainly due to the improved mobility induced by the significantly reduced carrier concentration. Such reduction of the carrier concentration was explained by the compensation of the antisite defects due to the addition of Bi. This behavior was also supported by observation of the carrier type transition indicated by the Seebeck coefficient.